Title

Aspects of nonequilibrium quantum many-body system: quantum entanglement dynamics, decoherent quantum quench, and one-particle perspective under dissipative and decoherent dynamics

Permalink

https://escholarship.org/uc/item/1v676141

Author

Kuo, Wei-Ting

Publication Date

2022

Peer reviewed|Thesis/dissertation

UNIVERSITY OF CALIFORNIA SAN DIEGO

Aspects of nonequilibrium quantum many-body system: quantum entanglement dynamics, decoherent quantum quench, and one-particle perspective under dissipative and decoherent dynamics

A dissertation submitted in partial satisfaction of the
requirements for the degree Doctor of Philosophy

in

Physics

by

Wei-Ting Kuo

Committee in charge:

Professor Daniel Arovas, Chair
Professor John Mcgreevy
Professor Jeffrey Rabin
Professor Yi-Zhuang You
Professor Joel Yuen-Zhou

2022

The Dissertation of Wei-Ting Kuo is approved, and it is acceptable in quality and form for publication on microfilm and electronically.

University of California San Diego

2022

DEDICATION

I dedicate this thesis to Jo-Fan Chien for her love, support and encouragement during my Ph.D. journey and to my family for their nursing and caring throughout my education. I also dedicate this thesis to my bunnies, Blueberry and Moo, who show the persistence to fight the illness and bring much joy to my life.

EPIGRAPH

”*Be curious, not judgmental.*”

-Walt Whitman

TABLE OF CONTENTS

LIST OF FIGURES

LIST OF TABLES

ACKNOWLEDGEMENTS

I would like to thank my advisor Prof. Daniel Arovas. When I was confused with any physics concepts, Dan always came up with a simple model for us to work on. During this investigation, I learned how to analyze a problem in great details and extracted the core knowledge from these toy models. I would also like to thank Prof. Yi-Zhuang You. Working with Yi-Zhuang is a great experience. Yi-Zhuang's innovative ideas and passions for physics always inspired me to explore those uncharted regions. Since I was new to condensed matter and quantum information when I joined UCSD, I have taken many courses from Prof. John Mcgreevy. I would like to thank John for his great courses. John could teach every concepts simply and clearly. Also, he could provide connections between different physics fields. I really learned a lot from all John's courses and finished those ”interesting” homework assignments. I have published six papers and this achievement comes from that I have a bunch of fantastic collaborators. I would like to thank Prof. Smitha Vishveshwara, Ahmed Akhtar, Hung-Hwa Lin, Jyotsna Gidugu, Paul Lauria, Yao-Yu Lin, Song-Mao Liao, Hung-Jin Huang, Olivia Hsuan-Min, and Jo-Fan Chien. It's a great experience to work with you all. Special thanks to Ming-Shiun Tsai for your Amazon Web Services support.

During my seven-year Ph.D. journey, I've done lab teaching assistant coordinator (LTAC) for six years. I really thank Prof. Mike Anderson, Prof. Avi Yagil and Prof. Phil Tsai for their support and trust when I was an LTAC. Also, our department staff members, Sharmila Poddar, Catherine McConney could always quickly solve my administrative questions . Thank you all to let me have a smooth Ph.D. journey.

Also I would like to thank my family's caring throughout my education to let me have this opportunity to study Ph.D. at UC San Diego. I would like ot thank my friends to let me have a wonderful Ph.D. journey - Xiang Ji, Yi Guo, Meng Zeng, Da-Chuan Lu, Hong-Ye Hu, Yi-Fan Xiang, Yi-Wen Huang, Jonathan Lam, Hsi-Ming Chang, Song-Mao Liao, Olivia Ou, Mendy Hsu, I-Da Chiang, Jung-Tsung Li, Tsung-Cheng Lu, Huan-Yu Kuo, Hung-Hwa Lin, Daniel Ben-Zion, Sebastian Diaz, Tom Zdyrski, Mac Lee, Joshua Lin, Yen-Ting Liu, Ming-Shiun Tsai. Siao-Fong

Li, Yen-Ting Hsu, Chih-I Chang, Pin-Chun Pai, Yi-Teng Huang.

Studying a Ph.D. is actually more mentally demanding than I expected. I was very fortunate to have my girl friend Jo-Fan Chien to stay with me all the way through my Ph.D. journey. Her love and mental support were invaluable. Her relentless positive attitude and passion for life open another door for me to experience the beauty of the world. Thank you for your patience and understanding. I would also like to thank my bunnies, Blueberry and Moo. They really bring much joy to my Ph.D. life. I learned how to keep on going regardless of any obstacles in front of me. In the end, I would like to thank myself for working hard to get this Ph.D. degree. You are the best.

Chapter 2 is, in part, a reprint of material from published work done in collaboration with A. A. Akhtar, Daniel P. Arovas, and Yi-Zhuang You, as it appears in Physical Review B. Wei-Ting Kuo, A. A. Akhtar, Daniel P. Arovas, and Yi-Zhuang You, ”Markovian Entanglement Dynamics under Locally Scrambled Quantum Evolution,” *Phys. Rev. B* **101**, 224202 (2020). The dissertation author was the primary investigator and author of this material.

Chapter 3 is, in part, a reprint of material from published work done in collaboration with Daniel P. Arovas, Smitha Vishveshwara,and Yi-Zhuang You, as it appears on Scipost. Wei-Ting Kuo, Daniel P. Arovas, Smitha Vishveshwara, and Yi-Zhuang You, ”Decoherent Quench Dynamics across Quantum Phase Transitions,” SciPost Phys. 11, 084 (2021). The dissertation author was the primary investigator and author of this material.

Chapters 4 is, in part, a reprint of material from work done in collaboration with Jyotsna Gidugu and Daniel P. Arovas, as it will appear on the arXiv. The dissertation author was the primary investigator and author of this material.

VITA

2013	Bachelor of Science in Physics, National Tsing Hua University, Hsinchu, Taiwan
2022	Doctor of Philosophy in Physics, University of California San Diego

PUBLICATIONS

Wei-Ting Kuo, A. A. Akhtar, Daniel P. Arovas, and Yi-Zhuang You, ”Markovian Entanglement Dynamics under Locally Scrambled Quantum Evolution,” *Phys. Rev. B* **101**, 224202 (2020)

Wei-Ting Kuo, Daniel P. Arovas, Smitha Vishveshwara, and Yi-Zhuang You, ”Decoherent Quench Dynamics across Quantum Phase Transitions,” *SciPost Phys.* **11**, 084 (2021)

Joshua Yao-Yu Lin, Song-Mao Liao, Hung-Jin Huang, Wei-Ting Kuo, and Olivia Hsuan-Min Ou, ”Galaxy Morphological Classification with Efficient Vision Transformer,” *NeurIPS 2021 Machine Learning and Physical Science Workshop Paper*

Paul Lauria, Wei-Ting Kuo, Nigel R. Cooper, and Julio T. Barreiro, ”Experimental Realization of a Fermionic Spin-Momentum Lattice,” *Phys. Rev. Lett.* **128**, 245301 (2022)

Hung-Hwa Lin, Wei-Ting Kuo, Daniel P. Arovas, and Yi-Zhuang You, ”Fluctuation of Chern Numbers in a Parametric Random Matrix Model,” arXiv:2207.12562

Wei-Ting Kuo, Jyotsna Gidugu, and Daniel P. Arovas, ”One particle perspective of the non-equilibrium steady state property for Aubry-Andre-Harper model under dissipative and decoherent dynamics,” *in preparation*

ABSTRACT OF THE DISSERTATION

Aspects of nonequilibrium quantum many-body system: quantum entanglement dynamics, decoherent quantum quench, and one-particle perspective under dissipative and decoherent dynamics

by

Wei-Ting Kuo

Doctor of Philosophy in Physics

University of California San Diego, 2022

Professor Daniel Arovas, Chair

In this dissertation, we study multiple nonequilibrium many-body systems from different aspects. We begin with a brief introduction to nonequilibrium system and general discussions of terminology. In Chapter 2, we study locally scrambled quantum evolution and develop a novel formalism to describe entanglement dynamics. In Chapter 3, we examine quantum quench across quantum phase transition in the presence of decoherence. We found a new scaling law in strong decoherence limit. In Chapter 4, we investigate multiple one-particle probes to diagnose the properties of steady states under dissipative and decoherent dynamics.

Chapter 1

Introduction

Physics is the branch of science which studies the nature and properties of matter. Matter is any substance with masses, including fundamental particles, materials around our daily life, and the largest galaxy in universe. The wide range of spatial scales and number of particles involved in matter match along with different branches in physics. Note that this scale hierarchy does not imply any subordinance or superiority between these branches. As Philip Anderson mentioned in his well-known article, ”More is different”[2], new generalization and concepts are required in different scales.

One significant example is the many-particle system with an enormously large number of particles, a typical number scale being the Avogadro's Number ($\sim 6.02 \times 10^{23}$). Studying a generic many-particle system is a challenging problem. However, under *equilibrium* assumption, we could simplify the many-particle system and utilize a relatively small number of thermodynamic variables to characterize it. This characterization does not allow complete and detailed descriptions of the system, such as the exact velocity of a certain particle. Instead, it means that the physical quantities could be described by a statistical ensemble average. The type of the statistical ensembles depends on system nature. For the classical system, the particles are distinguishable and the particle statistics is Maxwell-Boltzmann statistics. As for quantum systems, two types of spins along with indistinguishable particles give two different particle statistics, Bose-Einstein statistics and Fermi-Dirac statistics [3]. In addition, different conserved quantities in the system would lead to different ensembles, including micro-canonical, canonical, and grand-canonical ensembles. These tools in statistical mechanics enable us to describe a many-body system in equilibrium and compute physical quantities of interest from the well-established protocols.

By contrast, a nonequilibrium system fails to provide such universal protocols, which not only increases the difficulty in modeling nonequilibrium systems but also triggers much interest in exploring unique physical phenomena in nonequilibrium systems. In this thesis, I focus on several nonequilibrium systems and study their physical properties and behaviors. In Chap. 2, the target nonequilibrium system is a multi-qubit system under locally scrambled quantum dynamics which are realized by local random circuits. To characterize how this system arrives at equilibrium, we study the dynamics of quantum entanglement. Entanglement represents how separate portions in the system are correlated and dependent on each other. This correlation could exhibit differently in classical and quantum systems. To elaborate this dependence and the difference between classical and quantum systems, I would use a two-qubit system as an example. The qubit is a quantum-mechanical system with two states which are labeled by $|\uparrow\rangle, |\downarrow\rangle$. To quantitatively compute the dependence between these two qubits, I would use the information measure, mutual information, $I(A,B)$, defined as

$$I(A,B) = H(A) + H(B) - H(A,B) \tag{1.1}$$

where A,B represent different regions and $H(X)$ is the information entropy of region X. To compute the information entropy, I would first define reduced density matrix ρ_X. Suppose the density matrix for the full system is ρ, the reduced density matrix of the region X is $\rho_X = \mathrm{Tr}_{\bar{X}}\,\rho$ where $\bar{X}$ is the complement of the region X. The information entropy of the region X is defined as

$$H(X) = -\mathrm{Tr}\,\rho_X \log \rho_X. \tag{1.2}$$

In the following, I would compute the mutual information for three different two-qubit systems. The region A is the first qubit, whereas the region B is the second qubit. The first system is that these observed states of these two qubits are independent. The corresponding density matrix is

$$\rho = \frac{1}{4}|\uparrow\uparrow\rangle\langle\uparrow\uparrow| + \frac{1}{4}|\uparrow\downarrow\rangle\langle\uparrow\downarrow| + \frac{1}{4}|\downarrow\uparrow\rangle\langle\downarrow\uparrow| + \frac{1}{4}|\downarrow\downarrow\rangle\langle\downarrow\downarrow|. \tag{1.3}$$

The reduced density matrices are

$$\rho_A = \frac{1}{2}|\uparrow\rangle\langle\uparrow| + \frac{1}{2}|\downarrow\rangle\langle\downarrow|, \rho_B = \frac{1}{2}|\uparrow\rangle\langle\uparrow| + \frac{1}{2}|\downarrow\rangle\langle\downarrow| \tag{1.4}$$

The mutual information is zero since $H(A) = H(B) = \frac{1}{2}H(A,B) = \log 2$. The second system is that these two qubits are perfectly correlated. The density matrix is

$$\rho = \frac{1}{2}|\uparrow\uparrow\rangle\langle\uparrow\uparrow| + \frac{1}{2}|\downarrow\downarrow\rangle\langle\downarrow\downarrow|. \tag{1.5}$$

The reduced density matrices are equal to the first example,

$$\rho_A = \frac{1}{2}|\uparrow\rangle\langle\uparrow| + \frac{1}{2}|\downarrow\rangle\langle\downarrow|, \rho_B = \frac{1}{2}|\uparrow\rangle\langle\uparrow| + \frac{1}{2}|\downarrow\rangle\langle\downarrow|. \tag{1.6}$$

However, the information entropy for the full system is different, $H(A,B) = \log 2$. Hence, the mutual information is $I(A,B) = \log 2$. The third system is a quantum maximally entangled system. One typical example is the Bell state, $|\phi\rangle = \frac{1}{\sqrt{2}}(|\uparrow,\uparrow\rangle + |\downarrow,\downarrow\rangle)$. Then, we can construct the density matrix as

$$\rho = \frac{1}{2}|\uparrow\uparrow\rangle\langle\uparrow\uparrow| + \frac{1}{2}|\uparrow\uparrow\rangle\langle\downarrow\downarrow| + \frac{1}{2}|\downarrow\downarrow\rangle\langle\uparrow\uparrow| + + \frac{1}{2}|\downarrow\downarrow\rangle\langle\downarrow\downarrow|. \tag{1.7}$$

Since this density matrix is constructed from a pure state, the corresponding information entropy is simply zero. As for the reduced density matrices, they are equal to the previous examples.

Hence, the resultant mutual information is $2\log 2$. This simple example quantitatively presents the difference between classical correlation and quantum entanglement (quantum correlation). Since quantum entanglement builds on quantum nature of the system, quantum entanglement dynamics is an unique and useful tool to diagnose nonequilibrium quantum many-body systems. In this work, we developed a new formalism to describe entanglement dynamics under locally scrambled quantum dynamics. This new framework provided us with a novel perspective to view the entanglement dynamics with an imaginary-time Schrödinger equation.

In Chap. 3, the nonequilibrium system is a quantum many-body system under quantum quench dynamics across a critical point with decoherence. In a quantum quench, the system is prepared at the ground state of the initial Hamiltonian (H_0). Then, the system evolves with a different Hamiltonian (H_e). Typically, these two Hamiltonians have the same format but with different parameters (m_0/m_e). Based on how the Hamiltonian is tuned between H_0 and H_e, the quantum quench can be divided into two types: sudden quenches and continuous quenches. The sudden quenches indicated a sudden change of parameter from m_0 to m_e at $t = 0$. As for continuous quenches, the parameter would gradually change from m_0 to m_e with a quench rate $1/\tau$. The sudden quenches can be also considered as a limiting case as $\tau \to 0$. This quench rate serves a source which drives the system out of equilibrium, whereas another important time scale, the intrinsic relaxational time scale, would try to bring system back to equilibrium. This intrinsic relaxational time scale is determined by the inverse of energy gap. For any nonzero energy gap, it's always possible to find a slow enough quench rate to maintain system equilibrium. However, the equilibrium could not be achieved with the existence of critical point during continuous quench. The gap-closing behavior at the critical point leads to a divergent relaxational time scale. Hence, the final state of the system fails to arrive equilibrium regardless of the quench rate. Even though the final state is a non-equilibrium system, its universal length scale can still be predicted from Kibble-Zurek scaling[4, 5, 6, 7], which contains correlation length exponent and dynamical critical exponent of the critical point. This Kibble-Zurek scaling serves as a strong tool under nonequilibrium dynamics. In this work, we incorporate the environmental decoherence during the continuous quench, which leads to a new scaling relation in strong decoherent limit. We perform numerical simulation to verify our analytical prediction.

In Chap. 4, the non-equilibrium system is the quasi-periodic system under dissipative and dephasing dynamics. Our quasi-periodic system is the one-dimensional Aubry-Andre-Harper model which could exhibit extended and localized phases under different relative strengths between nearest-neighboring and incommensurate on-site potential. In this work, we couple Aubry-Andre-Harper model with the environment and aim at studying the corresponding non-equilibrium steady states. The probes are participation ratio, one-particle von Neumann entropy and one-particle logarithmic negativity. Our results suggest their ability to capture phase properties and potential future application to investigate different phases in open quantum system.

Chapter 2

Markovian entanglement dynamics under locally scrambled quantum evolution

2.1 Synopsis

We study the time evolution of quantum entanglement for a specific class of quantum dynamics, namely, the locally scrambled quantum dynamics, where each step of the unitary evolution is drawn from a random ensemble that is invariant under local (on-site) basis transformations. In this case, the average entanglement entropy follows a Markovian dynamics, such that the entanglement property of the future state can be inferred from the entanglement property of the unitary operator of the underlying quantum dynamics. We introduce the entanglement feature formulation to concisely organize the entanglement entropies over all subsystems into a many-body wave function, which allows us to describe the entanglement dynamics using an imaginary-time Schrödinger equation, such that various tools developed in quantum many-body physics can be applied. The framework enables us to investigate a variety of random quantum dynamics beyond Haar random circuits and Brownian circuits. We perform numerical simulations for these models and demonstrate the validity and prediction power of the entanglement feature approach.

2.1.1 Contribution of the author

The author has contributed in developing the main formalism and in writing the paper. He has performed the numerical calculations together with A. A. Akhtar.

2.2 Introduction

Quantum entanglement dynamics[8, 9, 10, 11, 12] is an emerging field that ties several interesting topics together, including non-equilibrium and driven quantum systems[13, 14, 15], many-body localization and thermalization[16, 17, 18, 19, 20, 21], quantum chaos and holography[22, 23, 24, 25, 26]. The central theme is to understand the production and propagation of quantum entanglement in quantum many-body systems. For pure states, the amount of quantum entanglement between a subsystem A and its environment $\bar{A}$ can be quantified by the (Rényi) *entanglement entropy* (EE) $S^{(n)}(A) = \frac{1}{1-n} \log \mathrm{Tr}_A \rho_A^n$ where $\rho_A = \mathrm{Tr}_{\bar{A}} |\Psi\rangle\langle\Psi|$ is the reduced density matrix of subsystem A. Various quantum information measures (such as mutual and tripartite information) can be constructed from the EE over different regions. Here, we would like to focus on the 2nd Rényi entropies $S^{(2)}(A)$ and establish their dynamic equations under quantum evolution.

As a quantum state $|\Psi\rangle$ evolves in time, its EE's $S^{(2)}(A)$ over different regions A will also change with respect to time in general. It is desired to understand how the unitary evolution of the quantum state induces the dynamics of quantum entanglement. There have been several works on the entanglement growth in quantum many-body systems[27, 28, 29, 12, 24, 30, 31, 32, 33, 34, 35, 36, 37]. The main focus has been on the half-system (or a single region) EE. To gain more resolution of the many-body entanglement structure, we extend our scope to all possible bipartitions of the system (including multiple disconnected entanglement regions). The question we would like to address is that given $S^{(2)}(A)$ at initial time over all possible subsystems A, what will be the equation of motion governing the evolution for all of them jointly in later time?

However, EE's over all regions contain a large amount of data, because the number of possible bipartitions 2^L grows exponentially in system size L. We need a conceptually concise way to organize these entropy data, in order to make progress in describing their dynamics. In Ref. [38], it was proposed that all these EE's can be organized into "entanglement features", which admit compact representations in terms of Boltzmann weights of Ising models. The key idea is to label each entanglement region A by a set of Ising variables $\boldsymbol{\sigma} = (\sigma_1, \sigma_2, \cdots)$, such that $\sigma_i = \downarrow$ (or $\uparrow$) corresponds to $i \in A$ (or $i \in \bar{A}$) for each site i. Then the EE $S^{(2)}(A) \equiv S^{(2)}[\boldsymbol{\sigma}]$ can be treated as a free energy associated to the Ising configuration $\boldsymbol{\sigma}$, and the *entanglement feature* (EF) refers to the corresponding Boltzmann weight $W[\boldsymbol{\sigma}] = e^{-S^{(2)}[\boldsymbol{\sigma}]} = \operatorname{Tr} \rho_A^2$, which is simply the purity for the 2nd Rényi case. Its time evolution can be related to the Loschmidt echo on the duplicated system,[12] which could be of experimental relevance. In this work, we further develop the Ising formulation by encoding the EF as a fictitious spin state $|W\rangle = \sum_{\boldsymbol{\sigma}} W[\boldsymbol{\sigma}]|\boldsymbol{\sigma}\rangle$, which we called the EF state. This rewriting packs the exponentially many entanglement data into a single EF state (as a many-body wave function). This conceptual simplification enables us to formulate the entanglement dynamics in a concise form of imaginary-time Hamiltonian evolution of the EF state

$$\partial_t |W\rangle = -\hat{H}_{\text{EF}} |W\rangle, \tag{2.1}$$

which can be further analyzed using powerful tools that have been developed in quantum many-body physics. Our development is along the line of mapping entanglement dynamics to statistical mechanical problems, as discussed in a few recent works [39, 28, 30, 40, 32, 33, 41, 42]. Given the equivalence between statistical mechanics and imaginary-time quantum mechanics, it is not surprising that the entanglement dynamics could admit a quantum mechanical formulation as Eq. (2.1).

Treating the EF $W[\boldsymbol{\sigma}]$ as an (unnormalized) probability distribution of entanglement regions $\boldsymbol{\sigma}$, the proposed dynamic equation in Eq. (2.1) could be interpreted as a Markov equation. The assumption behind this equation is that the future EF of a many-body state can be entirely determined based on the current EF without the need to know about the past EF or about other information beyond the EF. Unfortunately, this assumption does *not* hold in general! In fact, the entanglement dynamics is generally non-Markovian, meaning that knowing the present EE's even for all possible regions is still insufficient to determine their evolution in the future,[1] so we should not expect Eq. (2.1) to work in general. In this work, we point out a specific yet rich enough class of quantum dynamics, called the *locally scrambled* quantum dynamics, whose entanglement dynamics can be described by Eq. (2.1) (or some discrete version of it). Quantum dynamics can always be formulated as a unitary evolution $U = \prod_t U_t$ that can be chopped up into products of simpler unitaries U_t at each time slice t following a time ordering. A quantum dynamics is said to be locally scrambled, if for every time step, the unitary U_t is drawn from a random unitary ensemble that is invariant under local (on-site) basis transformations, and U_t at different time t are sampled independently. Such dynamics can be constructed by inserting local scramblers (product of on-site Haar random unitaries) between every time step, as if the system constantly forget about the choice of local basis from one time step to another. It can be used to model those quantum many-body systems with fast and random dynamics on each site, such that the quantum information is scrambled on each site quickly and sufficiently during each step of the time evolution. One famous example in this class is the Haar random unitary circuit[28, 40, 31, 32]. We will provide more examples of locally scrambled quantum dynamics in this work.

The reason that the future EE can be uniquely determined by the present EE under the locally scrambled quantum dynamics is related to the fact that the EE is a local-basis-independent quantity. As the local scramblers constantly remove the local-basis-dependent information in the quantum many-body state, only the local-basis-independent information can survive in time to govern the future evolution. Such local-basis-independent information can be captured by EE's over all possible entanglement regions, which are summarized as the EF of the quantum many-body state. In this work, we develop the theoretical framework to derive the dynamic

---

[1] One can easily construct examples like $|\uparrow\uparrow\rangle$ and $|\uparrow\downarrow\rangle$, which are both product states, but their evolution under the same Hamiltonian $H = \boldsymbol{S}_1 \cdot \boldsymbol{S}_2$ will result in states of different entanglements.

equation governing the evolution of the EF under locally scrambled quantum dynamics. We establish a systematic approach to construct the EF Hamiltonian $\hat{H}_{\text{EF}}$ based on the entanglement properties of the physical Hamiltonian or unitary operators that describe the quantum dynamics. We also carry out numerical simulations to justify the assumptions made in the theoretical development, and demonstrate the prediction power of the EF approach.

The paper is organized as follows. In Sec. 2.3, we first develop the theoretical framework for the EF and its application to the locally scrambled quantum dynamics. We start with the definition of EF for both quantum many-body state and quantum unitary circuits in Sec. 2.3.1. We then promote these notions to their quantum mechanical versions, introducing the EF states and EF operators in Sec. 2.3.2. With this setup, in Sec. 2.3.3, we prove an important relation between the the state and the unitary EF's, thereby mapping the unitary evolution of the quantum state to the dissipative evolution of the EF state under the corresponding entanglement dynamics in Sec. 2.3.4. Taking the continuum limit, we obtain the Schrödinger equation for EF state and derived the most generic form of the EF Hamiltonian in Sec. 2.3.5. We analyze the spectral properties of the EF Hamiltonian and their consequences on the universal behavior of entanglement dynamics in Sec. 2.3.6. We investigate the excitation spectrum of the EF Hamiltonian and obtain the quasiparticle dispersion in Sec. 2.3.7, which allows us to predict the long-time saturation behavior of the entanglement. We will provide numerical evidences in Sec. 2.4 to demonstrate the validity of the EF approach. We first introduce two models of locally scrambled quantum dynamics in Sec. 2.4.1, namely the locally scrambled quantum circuit and the locally scrambled Hamiltonian dynamics, which are further discussed in details in Sec. 2.4.2 and Sec. 2.4.3 separately. We sum up in Sec. 2.5 making connections to related topics and potential future development.

2.3 Theoretical framework

2.3.1 Definition of entanglement features

Let us consider a quantum many-body system consisting of L qudits, where each qudit (d-dimensional quantum system) has a d-dimensional physical Hilbert space, such that the total Hilbert space dimension is d^L. To define the 2nd Rényi entropy, we will need to duplicate the system and evaluate the expectation value of swap operators within a subsystem A of interest. There are altogether 2^L possible choices of a subsystem A, as each qudit can independent decide to be included in A or not. To label the 2^L different bipartitions of the system, we introduce a set of classical Ising variables $\boldsymbol{\sigma} = (\sigma_1, \sigma_2, \cdots, \sigma_L)$, such that the Ising variable σ_i determines if the ith qudit belongs to region A or its complement $\bar{A}$, following

$$\sigma_i = \begin{cases} \uparrow & i \in \bar{A}, \\ \downarrow & i \in A. \end{cases} \tag{2.2}$$

These Ising variables do not correspond to any degrees of freedom of the underlying quantum many-body system. Instead, they represent the identity or swap operator supported on the duplicated system, which are used to define the 2nd Rényi entropy. To be more specific, we define a permutation operator $\mathscr{X}_{\sigma_i}$ acting on the duplicated Hilbert space of the ith qudit,

$$\mathscr{X}_{\sigma_i} = \begin{cases} ||_i \equiv \sum_{\alpha,\beta=1}^{d} |\alpha\beta\rangle_i\langle\alpha\beta|_i & \text{if } \sigma_i = \uparrow, \\ \text{X}_i \equiv \sum_{\alpha,\beta=1}^{d} |\alpha\beta\rangle_i\langle\beta\alpha|_i & \text{if } \sigma_i = \downarrow, \end{cases} \tag{2.3}$$

which is assigned to the identity operator $||_i$ or the swap operator X_i depending on the Ising variable σ_i. Assembling these permutation operators together, we define $\mathscr{X}_{\boldsymbol{\sigma}} = \bigotimes_{i=1}^{L} \mathscr{X}_{\sigma_i}$ for the duplicated L-qudit system, which implements swap operations in the region A specified by the Ising configuration $\boldsymbol{\sigma}$.

With these notation setup, we can define the *entanglement feature* (EF) of quantum many-body states and time-evolution unitary circuits[43, 38]. The EF of a many-body pure state

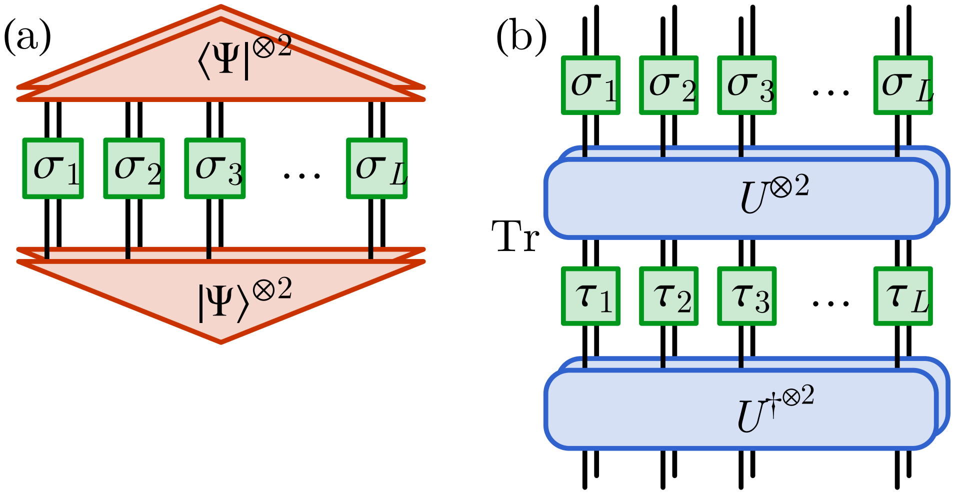

Figure 2.1. Diagrammatic representation of (a) the state EF $W_{|\Psi\rangle}[\boldsymbol{\sigma}]$ and (b) the unitary EF $W_U[\boldsymbol{\sigma},\boldsymbol{\tau}]$. The Tr operator contracts the dangling bottom legs with the corresponding dangling top legs.

$|\Psi\rangle$ is defined as

$$W_{|\Psi\rangle}[\boldsymbol{\sigma}] \equiv e^{-S^{(2)}[\boldsymbol{\sigma}]} = \mathrm{Tr}\left(\mathscr{X}_{\boldsymbol{\sigma}}(|\Psi\rangle\langle\Psi|)^{\otimes 2}\right), \tag{2.4}$$

which resembles Boltzmann weights for Ising configurations $\boldsymbol{\sigma}$ labeling different entanglement regions. In terms of the tensor network representation, the state EF can be depicted as Fig. 2.1(a). Not only for quantum states, the EF can also be defined for unitary circuits under the state-operator correspondence.[23, 44, 45] The EF of a unitary circuit U is defined as

$$W_U[\boldsymbol{\sigma},\boldsymbol{\tau}] = \mathrm{Tr}\left(\mathscr{X}_{\boldsymbol{\sigma}}U^{\otimes 2}\mathscr{X}_{\boldsymbol{\tau}}U^{\dagger\otimes 2}\right), \tag{2.5}$$

which depends on two sets of Ising configurations $\boldsymbol{\sigma}$ and $\boldsymbol{\tau}$ that separately specifies the entanglement regions on the past (input) and the future (output) sides of the unitary circuit, as illustrated in Fig. 2.1(b). The state EF $W_{|\Psi\rangle}[\boldsymbol{\sigma}]$ provides a comprehensive description of the entanglement properties of the pure state $|\Psi\rangle$, which contains the information about EE, mutual information and multipartite information among different subsystems. Similarly, the unitary EF $W_U[\boldsymbol{\sigma},\boldsymbol{\tau}]$

characterizes the entanglement properties of the unitary circuit U, including the EE and mutual information between past and future degrees of freedoms, which are also closely related to the operator-averaged out-of-time ordered correlator (OTOC)[23, 46, 47] under the quantum dynamics U.

It worth mention that entanglement features are invariant under *local basis transformations*. A generic local basis transformation takes the form of $V = \bigotimes_{i=1}^{L} V_i$ with V_i being a unitary operator acting on the ith qudit. It is easy to see that both the state EF and the unitary EF are independent of the choice of local basis, i.e.

$$W_{V|\Psi\rangle} = W_{|\Psi\rangle}, \quad W_{V^\dagger U V} = W_U. \tag{2.6}$$

In this way, the EF forgets about the local basis dependent information in quantum states or unitary circuits, and only captures the entanglement properties that are universal to local basis choices.

2.3.2 Operator formalism of entanglement features

To make our notation more concise, let us introduce a set of Ising basis $|\boldsymbol{\sigma}\rangle$, then we can pack $W_{|\Psi\rangle}$ to an *entanglement feature state* (EF state) $|W_\Psi\rangle$ as

$$|W_\Psi\rangle = \sum_{\boldsymbol{\sigma}} W_{|\Psi\rangle}[\boldsymbol{\sigma}]|\boldsymbol{\sigma}\rangle, \tag{2.7}$$

and W_U to an *entanglement feature operator* (EF operator) $\hat{W}_U$ as

$$\hat{W}_U = \sum_{\boldsymbol{\sigma},\boldsymbol{\tau}} |\boldsymbol{\sigma}\rangle W_U[\boldsymbol{\sigma},\boldsymbol{\tau}]\langle\boldsymbol{\tau}|. \tag{2.8}$$

The Ising basis $|\boldsymbol{\sigma}\rangle$ span a 2^L-dimensional Hilbert space of L qubits, called the *entanglement feature Hilbert space* (EF Hilbert space). It should not be confused with the d^L-dimensional physical Hilbert space of the underlying quantum many-body system. Each Ising basis state $|\boldsymbol{\sigma}\rangle$

in the EF Hilbert space simply corresponds to a bipartition of the L physical qudits following Eq. (2.2).

Given the EF state $|W_\Psi\rangle$, the EE $S^{(2)}[\boldsymbol{\sigma}]$ over all regions can be retrieved from the inner product of $|W_\Psi\rangle$ with the corresponding Ising basis state

$$e^{-S^{(2)}[\boldsymbol{\sigma}]} = W_{|\Psi\rangle}[\boldsymbol{\sigma}] = \langle \boldsymbol{\sigma} | W_\Psi \rangle. \tag{2.9}$$

In particular, a *product state* $|\Psi_{\text{prod}}\rangle = \bigotimes_i |\psi_i\rangle$ has zero EE in any region ($\forall \boldsymbol{\sigma} : S^{(2)}[\boldsymbol{\sigma}] = 0$), so its EF state is therefore a equal weight superposition of all Ising configurations,

$$|W_{\text{prod}}\rangle = \sum_{\boldsymbol{\sigma}} |\boldsymbol{\sigma}\rangle \quad \text{(product state)}, \tag{2.10}$$

which corresponds to the (ideal) paramagnetic state of Ising spins. On the other hand, a *Page state*[48] $|\Psi_{\text{Page}}\rangle$ exhibits the maximal volume-law EE, whose EF state is given by

$$|W_{\text{Page}}\rangle = \sum_{\boldsymbol{\sigma}} \frac{\cosh(\eta \sum_{i=1}^{L} \sigma_i)}{\cosh(\eta L)} |\boldsymbol{\sigma}\rangle \quad \text{(Page state)}, \tag{2.11}$$

where $\eta = \frac{1}{2}\log d$ and we have adopted $\sigma_i = \pm 1$ in the formula to represent $\uparrow, \downarrow$ spins. This result follows from the definition. Its detailed derivation can be found in Appendix A.1. The state $|W_{\text{Page}}\rangle$ contains extensive ferromagnetic correlations among Ising spins. In this picture, the process of quantum state thermalization corresponds to the process of building up ferromagnetic correlations in the EF state (until saturation to the Page state).

Let us also provide some examples for the EF of unitary gates which will be useful later. The EF of a single-qudit identity operator is straightforward to calculate based on the definition in Eq. (2.5),

$$\begin{aligned} \hat{W}_{\mathbb{1}} &= d^2(|\uparrow\rangle\langle\uparrow| + |\downarrow\rangle\langle\downarrow|) + d(|\uparrow\rangle\langle\downarrow| + |\downarrow\rangle\langle\uparrow|), \\ &= d(d + X), \end{aligned} \tag{2.12}$$

where X denotes the Pauli-X operator acting on the qudit site (acting in the EF Hilbert space, not in the qudit Hilbert space), and d is the qudit dimension. A more non-trivial example is the EF of a two-qudit Haar random unitary gate U_{ij} (averaged over Haar ensemble) that acts on qudits i and j,

$$\begin{aligned}\hat{W}_{\text{Haar}} =& d^2(d+X_i)(d+X_j) \\ & -\frac{d^2(d^2-1)}{d^2+1}\frac{1-Z_iZ_j}{2}(d^2-X_iX_j),\end{aligned} \tag{2.13}$$

where X_i and Z_i are Pauli-X and Z operators acting on site i. The derivation can be found in Appendix A.2.

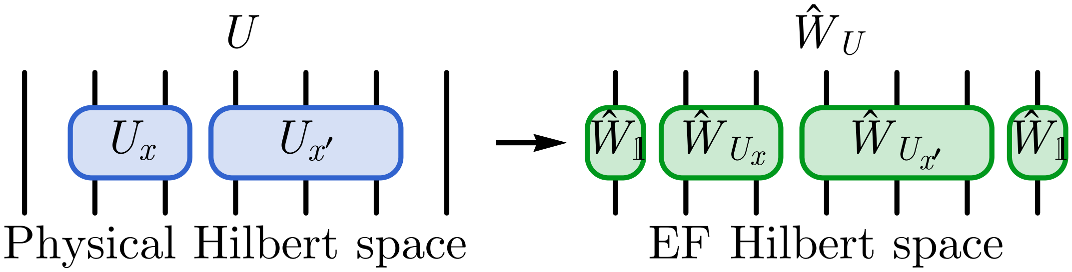

Figure 2.2. The mapping from the unitary operator in the physical Hilbert space to the corresponding EF operator in the EF Hilbert space. Locality is preserved under the mapping, enabling us to factorize the operators in the same manner on both sides.

Unitary gates are the building blocks to construct more complicated unitary circuits. One nice property of the EF operator is that it preserves the locality in space, meaning that if a unitary U operator can be factorized to smaller unitaries U_x over the space x, its corresponding EF operator $\hat{W}_U$ is also factorized in the same manner

$$U=\bigotimes_x U_x \quad \Rightarrow \quad \hat{W}_U=\bigotimes_x \hat{W}_{U_x}, \tag{2.14}$$

as examplified in Fig. 2.2. This property allows us to assemble the local EF operators together. For example, the EF operator $\hat{W}_{\mathbb{1}}$ of the identity operator for a L qudit system be obtained by assembling the single-qudit result in Eq. (2.12) together

$$\hat{W}_{\mathbb{1}} = \prod_{i=1}^{L} d(d+X_i) = (\coth\delta\,\operatorname{csch}\delta)^L \prod_{i=1}^{L} e^{\delta X_i}, \tag{2.15}$$

where we have introduced the constant δ

$$\delta \equiv \operatorname{arccoth} d = \frac{1}{2}\log\frac{d+1}{d-1} \tag{2.16}$$

to exponentiate the operator. The exponential form allows us to take the operator inverse easily, such that

$$\hat{W}_{\mathbb{1}}^{-1} = \prod_{i=1}^{L} \frac{1-d^{-1}X_i}{d^2-1} = (\tanh\delta\,\sinh\delta)^L \prod_{i=1}^{L} e^{-\delta X_i}. \tag{2.17}$$

These results will be useful in later discussions. In the following, we will show how the evolution of the EF state can be inferred from the EF operator of the unitary circuit.

2.3.3 Relation between state and unitary entanglement features

Suppose U describes a unitary circuit that evolves an initial quantum many-body state $|\Psi\rangle$ to the final state $U|\Psi\rangle$. This quantum dynamics will induce a corresponding entanglement dynamics, under which the EF of the initial state $W_{|\Psi\rangle}$ evolves to that of the final state $W_{U|\Psi\rangle}$. Can we predict the final state EF $W_{U|\Psi\rangle}$ based on our knowledge about the initial state EF $W_{|\Psi\rangle}$ and the EF W_U of the unitary evolution?

In general, this problem is not well-posed. Because U and $|\Psi\rangle$ contain many "non-universal" features that are specific to the choice of local basis, such features may affect the final state entanglement, but they are not captured by the EF, as the EF is invariant under local basis transformations. Therefore, the final state EF can not be inferred from the initial state EF and the unitary EF in general. However, instead of dealing with a specific unitary circuit U, we consider an ensemble of unitary circuits $U' = V^\dagger U V$ related to U by local basis transformations

V, denoted by

$$\mathscr{E}_U = \left\{ V^\dagger U V \middle| V = \bigotimes_{i=1}^{L} V_i, V_i \in \text{Haar} \right\}, \tag{2.18}$$

where each V_i is independently drawn from the Haar random unitary ensemble defined on the ith qudit. We will call $\mathscr{E}_U$ the *locally scrambled* unitary ensemble associated with U. According to Eq. (2.6), one immediately sees that all unitary operators $U' \in \mathscr{E}_U$ in the ensemble share the *same* entanglement feature as that of U, i.e. $W_{U'} = W_U$. Rather than asking about the EF of a specific final state $U|\Psi\rangle$, if we are allowed to consider the ensemble average of the EF over all final states $U'|\Psi\rangle$ with $U' \in \mathscr{E}_U$, the final state EF $W_{U'|\Psi\rangle}$ will indeed be constructable from the initial state EF $W_{|\Psi\rangle}$ and the unitary EF $W_{U'} = W_U$ on the average level. Using the operator formalism, the relation can be written in a concise form as

$$\mathop{\mathbb{E}}_{U' \in \mathscr{E}_U} |W_{U'\Psi}\rangle = \hat{W}_U \hat{W}_{\mathbb{1}}^{-1} |W_\Psi\rangle, \tag{2.19}$$

where $\hat{W}_{\mathbb{1}}$ is the EF operator for the identity evolution $\mathbb{1}$ and $\hat{W}_{\mathbb{1}}^{-1}$ is its inverse, which was given in Eq. (2.17) explicitly. One can derive Eq. (2.19) using tensor network diagrams, see Appendix A.3 for details. To simplify the notation, we may suppress spelling out the ensemble average $\mathbb{E}_{U' \in \mathscr{E}_U}$ explicitly in later discussions, with the understanding that in this work any unitary operator appearing in the subscript of the EF operator will be implicitly averaged over local basis transformations. Eq. (2.19) establishes an important relation between the state and the unitary EF's, which enables us to compute the evolution of the state EF induced by the underlying quantum dynamics, given the EF of the corresponding unitary evolution U. A special case of Eq. (2.19) has been discussed in Ref. [38, 47], where the initial state is restricted to product states.

As a side remark, we would like to provide some justifications for the use of locally scrambled unitary ensembles $\mathscr{E}_U$. Technically speaking, working with these ensembles enables us to predict the future evolution of EE's purely based on their current data, because the local-basis-dependent features of a quantum state are removed by local scrambling and the remaining local-basis-independent features are captured by the EF[2]. This setup allows us to make progress in understanding the entanglement dynamics with a tractable theoretical limit. Physically speaking, we can imagine systems with separating time scales between the on-site and the inter-site quantum dynamics. Suppose the on-site dynamics is fast and random, then the quantum information would be sufficiently scrambled on every site, before it can spread out to other sites at a longer time scale. So the overall unitary evolution will constantly be interrupted by the insertion of local scramblers $V_i \in$ Haar, making the evolution effectively local-basis-independent. In fact, many well explored random unitary ensembles in the field of entanglement dynamics are local-basis-independent (or "locally scrambled" in our language), including random unitary dynamics[49, 50, 28], random Hamiltonian dynamics[38, 51, 52, 53] and random Floquet dynamics[54, 55]. This strategy has also been adopted in the discussion of operator dynamics[30, 31, 32, 35, 36] and random tensor networks[39, 43, 56, 42]. Historically, the study of these models has advanced our understanding about the universal behavior of entanglement dynamics, so we would like to carry on this line of research.

2.3.4 Markovian entanglement dynamics

As long as we know how to construct the EF operator $\hat{W}_U$ for any unitary evolution U of interest, we can apply the operator formalism in Eq. (2.19) to compute the entanglement dynamics. However, calculating the EF for a large and deep unitary circuit is a difficult many-body problem, hence the relation Eq. (2.19) is still hard to apply. But if all unitary gates in the unitary circuit are independently drawn from locally scrambled unitary ensembles, they will be decoupled in time, such that we can apply the EF operator iteratively to drive the evolution of the EF state.

To be more concrete, let us consider the case where the full unitary evolution can be

---

[2] Strictly speaking, all the local-basis-independent features are capture by the full set of Rényi entropy to all Rényi orders. But here we only focus on a subset described by the 2nd Rényi entropy.

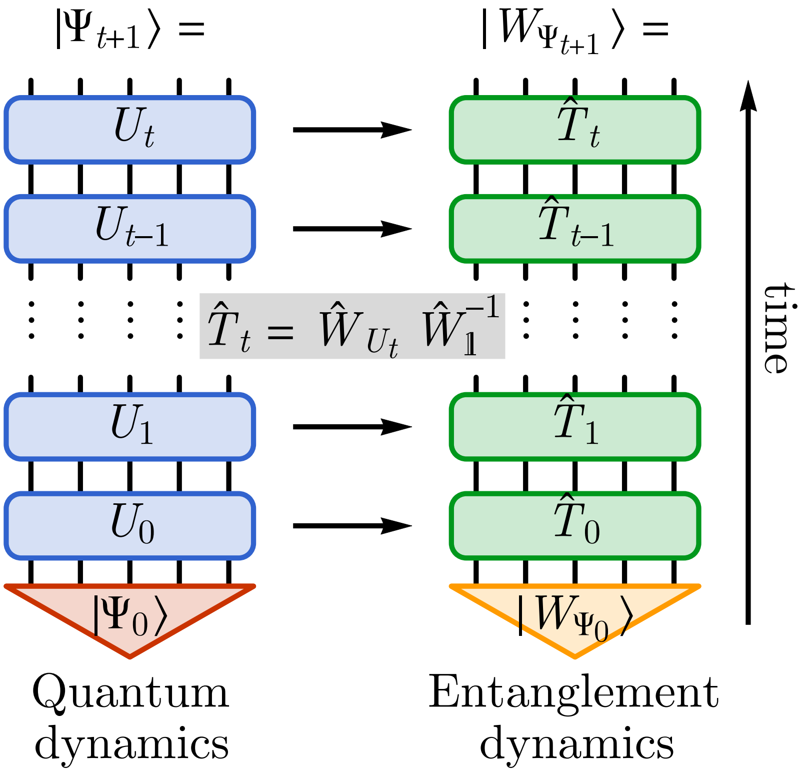

Figure 2.3. Quantum dynamics induces entanglement dynamics, assuming each unitary U_t is drawn from local basis invariant ensemble independently. The operator entanglement property of U_t determines the transfer matrix $\hat{T}_t$ that evolves the EF state via Eq. (2.25), and the EF state $|W_{\Psi_t}\rangle$ encodes the entanglement properties of the quantum state $|\Psi_t\rangle$.

broken up into discrete time steps (or layers), and each single-step unitary evolution at time t is described by U_t, as illustrated on the left of Fig. 2.3. Then the quantum many-body state $|\Psi_t\rangle$ evolves from step to step following

$$|\Psi_{t+1}\rangle = U_t|\Psi_t\rangle. \tag{2.20}$$

Suppose U_t at different time t are independently drawn from random unitary ensembles (not necessary Haar random) which are invariant under local basis transformation, then the full unitary evolution

$$U = \prod_t U_t = U_t U_{t-1} \cdots U_1 U_0 \tag{2.21}$$

will form a random unitary circuit that defines a *locally scrambled quantum dynamics*. If we spell out the local basis transformations V_t that has been made at each time step, i.e. $U_t = V_t^\dagger U_t' V_t$,

$$U = V_t^\dagger\, U_t'\, V_t V_{t-1}^\dagger\, U_{t-1}'\, V_{t-1} \cdots, \tag{2.22}$$

we can see that the neighboring transformations $V_t V_{t-1}^\dagger$ can merge into a single layer of local scramblers. Therefore a locally scrambled quantum dynamics can also be viewed as repeatedly applying the on-site scrambling $V_t V_{t-1}^\dagger$ followed by the inter-site unitary U_t'. In this way, the quantum many-body state is always sufficiently scrambled on each qudit and the scrambling is uncorrelated in time, such that the information about local basis choice does not pass on from step to step. Separating each step of the unitary evolution by local scramblers is our key assumption about the quantum dynamics, which enables us to proceed.

The entanglement dynamics induced by the locally scrambled quantum dynamics is Markovian, and admits a simple transfer matrix description. To see this, we evaluate the final state EF averaging over all locally scrambled unitary ensembles at different steps

$$|W_{\Psi_{t+1}}\rangle = \mathop{\mathbb{E}}_{U_t} \mathop{\mathbb{E}}_{U_{t-1}} \cdots |W_{U_t U_{t-1} \cdots \Psi_0}\rangle. \tag{2.23}$$

Applying Eq. (2.19), we arrive at the recurrent equation for the ensemble averaged EF state

$$|W_{\Psi_{t+1}}\rangle = \hat{T}_t |W_{\Psi_t}\rangle, \tag{2.24}$$

where we have introduced the transfer matrix

$$\hat{T}_t = \hat{W}_{U_t} \hat{W}_{\mathbb{1}}^{-1} \tag{2.25}$$

to evolve the EF state $|W_{\Psi_t}\rangle$ according to the EF of the single-step unitary U_t. As summarized in Fig. 2.3, Eq. (2.25) is the key equation that bridges the quantum dynamics and entanglement dynamics, allowing us to predict the evolution of entanglement properties of a quantum state based on the entanglement properties of the unitary operator applied at each time step. If we further assume *locality* of the quantum dynamics such that $U_t = \bigotimes_x U_{t,x}$ can be decomposed into products of non-overlapping local unitary gates $U_{t,x}$ (each gate only acts on a few qudits and its spatial position is labeled by x), the EF operator $\hat{W}_U$ can be factorized in the same manner following Eq. (2.14)

$$\hat{W}_{U_t} = \bigotimes_x \hat{W}_{U_{t,x}}, \tag{2.26}$$

where $\hat{W}_{U_{t,x}}$ is the EF operator for each local unitary gate, which can be easily computed (as it only involves a few qudits). Along this line, the transfer matrix $\hat{T}_t$ can be constructed purely based on our knowledge about the EF of each unitary gate involved in the quantum dynamics.

Using Eq. (2.24), we can evolve the EF of any initial quantum state in time, given the locally scrambled quantum dynamics. The time evolution of the (2nd Rényi) EE can be read out from the EF by

$$S^{(2)}[\boldsymbol{\sigma}](t) = -\log \langle \boldsymbol{\sigma} | W_{\Psi_t} \rangle, \tag{2.27}$$

following Eq. (2.9). Strictly speaking, there is a subtle issue about exchanging the order of the logarithm with all the ensemble average in Eq. (2.23). We are typically more interested in the ensemble average of the EE other than the EF. So the correct average for the EF should be the geometric mean $\exp(\mathbb{E}\log W[\boldsymbol{\sigma}])$, but we are replacing it by the algebraic mean $\mathbb{E}W[\boldsymbol{\sigma}]$ in Eq. (2.23), which always overestimates the EF and hence underestimates the EE. So the EE obtained in Eq. (2.27) only serves as a lower bound of the ensemble averaged EE. We may treat this lower bound as an approximation, but we can not claim that it is always a good approximation, because there are known scenarios where this approximation is problematic. For example, near the entanglement transition[42, 57, 58] where critical fluctuation is important, this approximate treatment gives wrong answers about the universality class and critical exponents. There have been more rigorous treatments developed in Ref. [42, 59] using replica tricks, but we will not pursuit that direction in this paper. For thermalizing dynamics and volume-law states, we believe that the lower bound estimation in Eq. (2.27) will provide a decent approximation, because the EF of thermalizing state contains strong ferromagnetic correlation to suppress the spin fluctuation, which allows us to replace the geometric mean by the algebraic mean as the fluctuation is small. We will rely on numerical simulations in Sec. 2.4 to justify this assumption.

To conclude, the EF formalism provides a concise description for the entanglement dynamics, when the underlying quantum dynamics is locally scrambled. However, there are also several limitations of locally scrambled quantum dynamics. First of all, the dynamics is not translation invariant in time, because the local scrambles at each step must be sampled independently. As a result, energy is not conserved under such dynamics. Secondly, global symmetry[35, 60] can not be implemented in the current scheme, because symmetry representations on each site will all be scrambled together, such that the symmetry can not be preserved. Finally, in lack of the local-basis-specific information, we can not discuss the operator dynamics for specific local operators[61] (but we can discuss operator averaged behaviors). To go beyond the local scrambling assumption, one idea could be to gradually introduce the correlation of unitary gates in time. But we will leave that for future study. We believe that our discussion of the locally scrambled quantum dynamics will set a cornerstone for future developments.

2.3.5 Entanglement feature Hamiltonian

In the previous section, we have derived the dynamic equation Eq. (2.24) for EF states under discrete time dynamics. We can also consider the continuum limit of the dynamics, where we refine the time step and take U_t to be close to identity (up to local basis transformation).

For example, we can consider generating U_t by a local Hamiltonian for a short amount of "time" $\varepsilon \ll 1$ with the local basis scrambled

$$U_t = V_t^\dagger e^{-\mathrm{i}\varepsilon H} V_t, \tag{2.28}$$

where $V_t = \bigotimes_{i=1}^{L} V_{t,i}$ is a layer of local scramblers and each scrambler $V_{t,i}$ is an on-site unitary operator independently drawn from Haar random ensemble. The full unitary evolution $U = \prod_t U_t$ is given by the time-ordered product. The onsite scrambling does not generate entanglement (among different sites). The entanglement generation and propagation all depend on the inter-site couplings in the Hamiltonian H. As ε is small, the entanglement dynamics will be slow (smooth) enough that it admits a continuum time description. We will study this model in more details later, but the goal here is to first establish a Hamiltonian formulation for the evolution of EF state in the continuum limit.

When U_t is close to an identity operator (up to local basis transformations), its EF operator $\hat{W}_{U_t}$ will approach $\hat{W}_{\mathbb{1}}$, hence the transfer matrix $\hat{T}_t = \hat{W}_{U_t} \hat{W}_{\mathbb{1}}^{-1}$ will also be close to the identity operator $\hat{\mathbb{1}}$ (in the EF Hilbert space). It turns out that the difference between $\hat{T}_t$ and $\hat{\mathbb{1}}$ is of the order ε^2 (not ε as one may expect). A general argument for this property is as follows. Given U_t in Eq. (2.28), its EF is described by

$$W_{U_t}[\boldsymbol{\sigma}, \boldsymbol{\tau}] = \mathrm{Tr}(\mathscr{X}_{\boldsymbol{\sigma}} e^{-\mathrm{i}\varepsilon \mathbb{H}} \mathscr{X}_{\boldsymbol{\tau}} e^{\mathrm{i}\varepsilon \mathbb{H}}), \tag{2.29}$$

with $\mathbb{H} = H \otimes \mathbb{1} + \mathbb{1} \otimes H$. It can be shown that $W_{U_t}[\boldsymbol{\sigma}, \boldsymbol{\tau}]$ must be even in ε, because it is real by definition but ε comes with the imaginary unit in Eq. (2.29), thus the odd-power expansions of

$W_{U_t}[\boldsymbol{\sigma}, \boldsymbol{\tau}]$ in ε could only be imaginary, and must therefore vanish altogether. So the operators $\hat{W}_{U_t}$ and $\hat{T}_t$ are even in ε, hence the leading order deviation of $\hat{T}_t$ from $\hat{\mathbb{1}}$ is of the order ε^2.

Given this, we expand $\hat{T}_t$ around the identity operator $\hat{\mathbb{1}}$ and define the *entanglement feature Hamiltonian* (EF Hamiltonian)

$$\hat{H}_{\mathrm{EF}} = \frac{1}{\varepsilon^2}(\hat{\mathbb{1}} - \hat{T}_t) = \frac{1}{\varepsilon^2}(\hat{\mathbb{1}} - \hat{W}_{U_t}\hat{W}_{\mathbb{1}}^{-1}), \tag{2.30}$$

such that the recurrent equation Eq. (2.24) transforms to an imaginary-time Schrödinger equation in the continuum limit of $\varepsilon \ll 1$,

$$\partial_t |W_{\Psi_t}\rangle = -\hat{H}_{\mathrm{EF}} |W_{\Psi_t}\rangle. \tag{2.31}$$

The differentiation $\partial_t |W_{\Psi_t}\rangle$ should be considered as the limit of $(|W_{\Psi_{t+\varepsilon^2}}\rangle - |W_{\Psi_t}\rangle)/\varepsilon^2$, where ε^2 serves as the infinitesimal time step. In general, $\hat{H}_{\mathrm{EF}}$ can be time-dependent, but let us omit the explicit time dependence for simplicity. The locality of the EF operator $\hat{W}_{U_t}$ as discussed in Eq. (2.26) translates to the locality of the EF Hamiltonian $\hat{H}_{\mathrm{EF}}$, which allow us to write $\hat{H}_{\mathrm{EF}} = \sum_x \hat{H}_x$ as sum of local terms. In principle, the specific form of these local terms $\hat{H}_x$ can be derived from the terms in the quantum many-body Hamiltonian H that drives the quantum dynamics, which we will demonstrate later in Sec. 2.4.3. However, even if we have no specific knowledge about H, we can already learn a lot about $\hat{H}_{\mathrm{EF}}$ based on the general properties of entanglement dynamics. In the following, we will show how the physical constraint of entanglement dynamics can pin down the general form of the EF Hamiltonian.

Let us consider the two-local EF Hamiltonian, meaning that the local terms $\hat{H}_x$ span over two sites at most. We find that the most general two-local EF Hamiltonian should take the following form

$$\hat{H}_{\mathrm{EF}} = \sum_{i,j} g_{ij} \frac{1 - Z_i Z_j}{2} e^{-\beta_{ij} X_i X_j - \delta(X_i + X_j)}, \tag{2.32}$$

where $g_{ij} \geq 0$ and $\beta_{ij} \in \mathbb{R}$ are model parameters and the constant δ is fixed by the qudit dimension d via $\coth\delta = d$. Here X_i, Z_i are Pauli operators acting on the ith Ising spin (that labels the entanglement region). Each local term in the Hamiltonian consists of a term $e^{-\beta_{ij}X_iX_j-\delta(X_i+X_j)}$ that fluctuates Ising spins, followed by a ferromagnetic projection operator $(1-Z_iZ_j)/2$. Although we call $\hat{H}_{\text{EF}}$ a Hamiltonian, it is not a Hermitian operator as expected in conventional quantum mechanics, because fluctuation term and the projection term do not commute. As a result, the left- and the right-eigenstates of $\hat{H}_{\text{EF}}$ could be different. The coupling strength g_{ij} describes the entangling power of the quantum dynamics, i.e. the velocity that the entanglement builds up between sites i and j if initialized from a product state.

The derived form of $\hat{H}_{\text{EF}}$ in Eq. (2.32) is constrained by the following physical requirements (or assumptions).

- Pure state remains pure under quantum dynamics (i.e. a $\mathbb{Z}_2$ Ising symmetry),

  $$[\hat{H}_{\text{EF}}, \prod_i X_i] = 0. \tag{2.33}$$

  An important entanglement property of pure states is that the EE of a region A should be the same as that of its complement $\bar{A}$, therefore the pure state EF must be invariant under Ising symmetry, i.e. $W_{|\Psi\rangle}[\boldsymbol{\sigma}] = W_{|\Psi\rangle}[-\boldsymbol{\sigma}]$, which can be equivalently written as $|W_\Psi\rangle = \prod_i X_i |W_\Psi\rangle$. Since any quantum dynamics (described by a unitary evolution) will preserve the purity of the quantum state, the entanglement dynamics should also respect this Ising symmetry, such that the EF Hamiltonian $\hat{H}_{\text{EF}}$ must commute with the symmetry operator $\prod_i X_i$ as asserted in Eq. (2.33).

- EE must vanish for empty entanglement regions,

  $$\langle\uparrow\uparrow\uparrow\cdots|\hat{H}_{\text{EF}} = 0. \tag{2.34}$$

  By empty entanglement region, we mean $A = \emptyset$ is an empty set, which correspond to the Ising configuration $\boldsymbol{\sigma} = \uparrow\uparrow\uparrow\cdots \equiv \Uparrow$ (i.e. $\forall i : \sigma_i = +1$). Hereinafter we use the symbol

$\Uparrow$ to denote the all-up configuration to simplify the notation. When the entanglement region is empty, the EE must be zero, i.e. $S^{(2)}[\Uparrow] = 0$. This requires $\langle \Uparrow | W_\Psi \rangle = W_{|\Psi\rangle}[\Uparrow] = e^{-S^{(2)}[\Uparrow]} = 1$ to remain constant under any entanglement dynamics. Now suppose $|W_{\Psi_t}\rangle$ is time dependent under the entanglement dynamics. Taking the time derivative on both sides of $\langle \Uparrow | W_{\Psi_t}\rangle = 1$ and applying the dynamic equation Eq. (2.31), we can see that $\langle \Uparrow | \partial_t | W_{\Psi_t}\rangle = -\langle \Uparrow | \hat{H}_{\mathrm{EF}} | W_{\Psi_t}\rangle = 0$ must hold for any EF state $|W_{\Psi_t}\rangle$, therefore we must require $\langle \Uparrow | \hat{H}_{\mathrm{EF}} = 0$ as claimed in Eq. (2.34).

- Statistical time-reversal symmetry of random unitary ensembles,

  $$\hat{W}_{\mathbb{1}} \hat{H}_{\mathrm{EF}}^{\intercal} = \hat{H}_{\mathrm{EF}} \hat{W}_{\mathbb{1}}. \tag{2.35}$$

  We assume that the random unitary gates in the circuit are statistically invariant under time-reversal, meaning that U_t and $U_t^\dagger$ will appear with equal probability in the unitary ensemble. Then according to the definition of unitary EF in Eq. (2.5), the time-reversal symmetry implies to $W_U[\boldsymbol{\sigma}, \boldsymbol{\tau}] = W_U[\boldsymbol{\tau}, \boldsymbol{\sigma}]$, i.e. $\hat{W}_U^\intercal = \hat{W}_U$. As a special case, we also have $\hat{W}_{\mathbb{1}}^\intercal = \hat{W}_{\mathbb{1}}$ by definition. Transposing both sides of $\hat{W}_U \hat{W}_{\mathbb{1}}^{-1} = \hat{\mathbb{1}} - \varepsilon^2 \hat{H}_{\mathrm{EF}}$, we obtain $\hat{W}_{\mathbb{1}}^{-1} \hat{W}_U = \hat{\mathbb{1}} - \varepsilon^2 \hat{H}_{\mathrm{EF}}^\intercal$. Therefore $\hat{H}_{\mathrm{EF}}^\intercal$ and $\hat{H}_{\mathrm{EF}}$ must be related by $\hat{W}_{\mathbb{1}} \hat{H}_{\mathrm{EF}}^\intercal = \hat{H}_{\mathrm{EF}} \hat{W}_{\mathbb{1}}$ as stated in Eq. (2.35). One known scenario that the statistical time-reversal symmetry is broken is that the unitary operators cyclically permute the qudit along one direction, which describes a quantum dynamics that has dynamic anomaly.[62, 63] We conjecture that the statistical time-reversal symmetry effectively restricts the quantum dynamics to be anomaly free.

With these conditions, we can start from a generic two-local Hamiltonian $\hat{H}_{\mathrm{EF}} = \sum_{i,j} \hat{H}_{ij}$ and derive the generic form of Eq. (2.32). First of all, the Ising symmetry in Eq. (2.33) restricts $\hat{H}_{ij}$ to be a linear combination of the following operators $\hat{H}_{ij} = x_1 + x_2 X_j + x_3 X_i + x_4 X_i X_j + x_5 Y_i Y_j + x_6 Y_i Z_j + x_7 Z_i Y_j + x_8 Z_i Z_j$, which contains all the two-local operators that commute with

X_iX_j. Then the left-null-state requirement in Eq. (2.34) further requires $x_1 = -x_8, x_2 = \mathrm{i}x_7, x_3 = \mathrm{i}x_6, x_4 = x_5$, which reduce $\hat{H}_{ij}$ to $(1 - Z_iZ_j)(x_1 + x_2X_j + x_3X_i + x_4X_iX_j)$. Finally, the statistical time-reversal symmetry in Eq. (2.35) requires

$$x_2 = x_3 = -\frac{d(x_1 + x_4)}{d^2 + 1}, \tag{2.36}$$

leaving only two independent parameters x_1 and x_4. This relation can be resolved by introducing another two parameters g and β to parametrize $x_1 + x_2X_j + x_3X_i + x_4X_iX_j = \frac{g}{2}e^{-\beta X_iX_j - \delta(X_i + X_j)}$ with $\coth\delta = d$ fixed, such that

$$\begin{aligned} x_1 &= \frac{g(d^2\cosh\beta - \sinh\beta)}{2(d^2 - 1)}, \\ x_2 = x_3 &= -\frac{gde^{-\beta}}{2(d^2 - 1)}, \\ x_4 &= \frac{g(\cosh\beta - d^2\sinh\beta)}{2(d^2 - 1)}, \end{aligned} \tag{2.37}$$

automatically satisfies Eq. (2.36). The resulting local term reads $\hat{H}_{ij} = g\frac{1 - Z_iZ_j}{2}e^{-\beta X_iX_j - \delta(X_i + X_j)}$, which matches the form of Eq. (2.32).

2.3.6 Universal behaviors of entanglement dynamics

The generic form of the EF Hamiltonian $\hat{H}_{\mathrm{EF}}$ in Eq. (2.32) is already useful to illustrate several universal behaviors about the entanglement dynamics. Suppose the EF Hamiltonian admits the following spectral decomposition

$$\hat{H}_{\mathrm{EF}} = \sum_a |R_a\rangle\lambda_a\langle L_a|, \tag{2.38}$$

where $|R_a\rangle$ and $\langle L_a|$ are respectively the right- and left-eigenstate of the eigenvalue λ_a. The right-eigenstate is related to the corresponding left-eigenstate by $|R_a\rangle \propto (\langle L_a|\hat{W}_{\mathbb{1}})^\intercal$, which follows from Eq. (2.35). Then the Schrödinger equation for EF state Eq. (2.31) can be formally solved as

$$|W_{\Psi_t}\rangle = \sum_a e^{-\lambda_a t} |R_a\rangle\langle L_a|W_{\Psi_0}\rangle. \tag{2.39}$$

The dynamics of the EE can be inferred from Eq. (2.27) as

$$\begin{aligned} S^{(2)}[\boldsymbol{\sigma}](t) &= -\log\langle\boldsymbol{\sigma}|W_{\Psi_t}\rangle \\ &= -\log\sum_a e^{-\lambda_a t}\langle\boldsymbol{\sigma}|R_a\rangle\langle L_a|W_{\Psi_0}\rangle. \end{aligned} \tag{2.40}$$

Independent of the choice of model parameters g_{ij}, β_{ij}, the EF Hamiltonian $\hat{H}_{\mathrm{EF}}$ has the following spectral properties:

- $\hat{H}_{\mathrm{EF}}$ is positive semi-definite (all its eigenvalues $\lambda_a \geq 0$ are real and non-negative),
- $\hat{H}_{\mathrm{EF}}$ always has (at least) a zero eigenvalue $\lambda_0 = 0$ in the $\mathbb{Z}_2$ (Ising parity) even sector, whose left- and right-eigenstates are

  $$\begin{aligned} \langle L_0| &= \frac{\langle\Uparrow| + \langle\Downarrow|}{2}, \\ |R_0\rangle &= |W_{\mathrm{Page}}\rangle. \end{aligned} \tag{2.41}$$

  The left zero mode $\langle L_0|$ is the Ising symmetric superposition of the all-up and the all-down states. The right zero mode $|R_0\rangle$ is the Page EF state given in Eq. (2.11).

The proof can be found in Appendix A.4. With these results, we can obtain several universal behaviors of entanglement dynamics with local scrambling in the short-time and long-time limit.

In the short-time limit ($t \to 0$), expanding the solution of EF state in Eq. (2.40) to first order in t, we can show that the EE grows *linearly* in time,

$$S^{(2)}[\boldsymbol{\sigma}](t) = S^{(2)}[\boldsymbol{\sigma}](0) + v_{\mathrm{E}}^{(2)}[\boldsymbol{\sigma}] \times t + \mathscr{O}(t^2), \tag{2.42}$$

where the linear-time coefficient $v_{\mathrm{E}}^{(2)}[\boldsymbol{\sigma}]$ is the entanglement growth rate, which is related to the entanglement velocity introduced in Ref. [64, 65]

$$v_{\mathrm{E}}^{(2)}[\boldsymbol{\sigma}] = \partial_t S^{(2)}[\boldsymbol{\sigma}](0) = \frac{\langle \boldsymbol{\sigma}|\hat{H}_{\mathrm{EF}}|W_{\Psi_0}\rangle}{\langle \boldsymbol{\sigma}|W_{\Psi_0}\rangle}. \tag{2.43}$$

The entanglement velocity $v_{\mathrm{E}}^{(2)}[\boldsymbol{\sigma}]$ characterizes how fast the EE grows in a given entanglement region specified by $\boldsymbol{\sigma}$. It is proportional to the matrix element of the EF Hamiltonian $\hat{H}_{\mathrm{EF}}$, as can be seen in Eq. (2.43), because $\hat{H}_{\mathrm{EF}}$ is the time-evolution generator that drives the entanglement dynamics. In particular, if the initial state is a generic product state, i.e. $|W_{\Psi_0}\rangle = |W_{\mathrm{prod}}\rangle = \sum_{\boldsymbol{\sigma}} |\boldsymbol{\sigma}\rangle$ as given in Eq. (2.10), the entanglement velocity $v_{\mathrm{E}}^{(2)}[\boldsymbol{\sigma}]$ admits an explicit formula

$$v_{\mathrm{E}}^{(2)}[\boldsymbol{\sigma}] = \sum_{\langle ij\rangle} \tilde{g}_{ij} \frac{1-\sigma_i\sigma_j}{2}, \tag{2.44}$$

where $\tilde{g}_{ij} = g_{ij} e^{-\beta_{ij}-2\delta} \geq 0$ is the effective coupling. Eq. (2.44) describes how the entanglement velocity $v_{\mathrm{E}}^{(2)}$ depends on the choice of the entanglement region $\boldsymbol{\sigma}$. It is obvious that the entanglement velocity $v_{\mathrm{E}}^{(2)}[\boldsymbol{\sigma}] \geq 0$ is non-negative for all choices of entanglement regions, because the EE can only *grow* from an unentangled product state. If $\tilde{g}_{ij} = \tilde{g}$ is uniform through out the system, $v_{\mathrm{E}}^{(2)}[\boldsymbol{\sigma}]$ will simply be proportional to the number of domain walls in the Ising configuration $\boldsymbol{\sigma}$, which is also the area $|\partial A|$ of the entanglement region A. Therefore the entanglement velocity follows the *area-law* scaling,

$$v_{\mathrm{E}}^{(2)} = \tilde{g}|\partial A|, \tag{2.45}$$

which can be expected from the locality of the entanglement dynamics in our setup.

In the long-time limit ($t \to \infty$), the EF state is dominated by the zero mode (assuming the zero mode is unique) and all the other modes decays exponentially with time. The positive semi-definite property of the EF Hamiltonian, i.e. $\lambda_a \geq 0$, ensures that all modes (except the zero mode) will decay exponentially in time. As $t \to \infty$, Eq. (2.39) reduces to

$$|W_{\Psi_\infty}\rangle = |R_0\rangle\langle L_0|W_{\Psi_0}\rangle, \tag{2.46}$$

with the left and right zero modes given by Eq. (2.41). Given that the EE vanishes in trivial regions, $\langle \Uparrow |W_\Psi\rangle = \langle \Downarrow |W_\Psi\rangle = 1$, so $\langle L_0|W_\Psi\rangle = 1$ for any EF state $|W_\Psi\rangle$. Then Eq. (2.46) results in

$$|W_{\Psi_\infty}\rangle = |R_0\rangle = |W_{\text{Page}}\rangle, \tag{2.47}$$

meaning that the EF always converge to that of the Page state in the long-time limit regardless what the initial state is. All states are doomed to thermalize under the quantum dynamics with local scrambling. The Page state will be their final destiny, whose EE reads

$$S^{(2)}[\boldsymbol{\sigma}] = -\log \frac{\cosh(\eta \sum_{i=1}^{L} \sigma_i)}{\cosh(\eta L)}, \tag{2.48}$$

which follows from Eq. (2.11). For $|A| \ll L$, the EE exhibits the *volume-law* scaling

$$S^{(2)}(A) = 2\eta|A|, \tag{2.49}$$

with the volume law coefficient given by $2\eta = \log d$. It worth mention that the above conclusion is based on the assumption that the zero mode is unique. If there are other degenerated zero modes (other than $|W_{\text{Page}}\rangle$), the final state may not converge to the Page state and the system can evade thermalization. We will discuss such a possibility later with a more concrete model in Sec. 2.4.2.

2.3.7 Excitation spectrum of the entanglement feature Hamiltonian

Having discussed the ground state property of the EF Hamiltonian $\hat{H}_{\text{EF}}$, let us turn to the low-lying excited states of $\hat{H}_{\text{EF}}$. According to Eq. (2.39), every eigenmode with finite eigenenergy λ_a will decay exponentially in time as $e^{-\lambda_a t}$. Eventually, only the ground state with zero eigenenergy ($\lambda_0 = 0$) would survive, and the system thermalizes to Page states. Hence the low-energy excitation spectrum determines how the EE approaches to its thermal limit in the late-time regime. Here we will focus on the spectrum of two kinds of excitations, namely the two-domain-wall excitation and the single spin-flip excitation, which dominate the low-energy excitations. We obtain the analytical expression of their dispersion relations, from which we can estimate the excitation gap and determine the relaxation time. In Sec. 2.4.3, we further compare the analytically estimated relaxation time with the numerical fitted one, and find good consistency.

For simplicity, we assume the parameters g_{ij}, β_{ij} in the EF Hamiltonian $\hat{H}_{\text{EF}}$ are spatially homogeneous (i.e $g_{ij} = g, \beta_{ij} = \beta$). For the parameter β, any unitary evolution generated from Hamiltonian $e^{-\mathrm{i}\varepsilon H}$ would have nonzero β only at the order of $\mathscr{O}(\varepsilon^2)$ in small ε limit (see Appendix A.7 for details). Hence, we will take $\beta = 0$ in the following. More general results for $\beta \neq 0$ can be found in Appendix A.5 and Appendix A.6. To first gain some intuitions about the excitation spectrum, we start with the exact diagonalization (ED) of EF Hamiltonian. The result is shown in Fig. 2.4. Apart from the eigenenergy λ_a, every state $|R_a\rangle$ is also label by its crystal momentum k_a, which is defined through its translation eigenvalue as $\mathsf{T}|R_a\rangle = e^{\mathrm{i}k_a}|R_a\rangle$, where the translation operator T is defined by its action on the Ising basis $\mathsf{T}|\sigma_1\sigma_2\cdots\sigma_L\rangle = |\sigma_L\sigma_1\cdots\sigma_{L-1}\rangle$. Note that the periodic boundary is assumed in our system. One can see that above the ground state at $\lambda_0 = 0$ and $k_0 = 0$, there is a continuum of excited states.

To better understand these excited states, we look into their wave function. We realize that the excitation can be classified based on the number of domain walls in the *left*-eigenstate. For instance, $\langle\uparrow\cdots\uparrow\downarrow\cdots\downarrow\uparrow\cdots\uparrow|$ is an example of two-domain-wall states. As mentioned in Eq. (2.41), the left ground state $\langle L_0| = (\langle\Uparrow| + \langle\Downarrow|)/2$ contains no domain wall and hence no excitation. Other excited left-eigenstates will be a superposition of states of different domain-wall number. Note that the corresponding right eigenstates can be obtained from $|R\rangle = (\langle L|\hat{W}_{\mathbb{1}})^{\mathsf{T}}$. Fig. 2.5 shows the weights of different domain-wall states in the lowest-energy excited state of

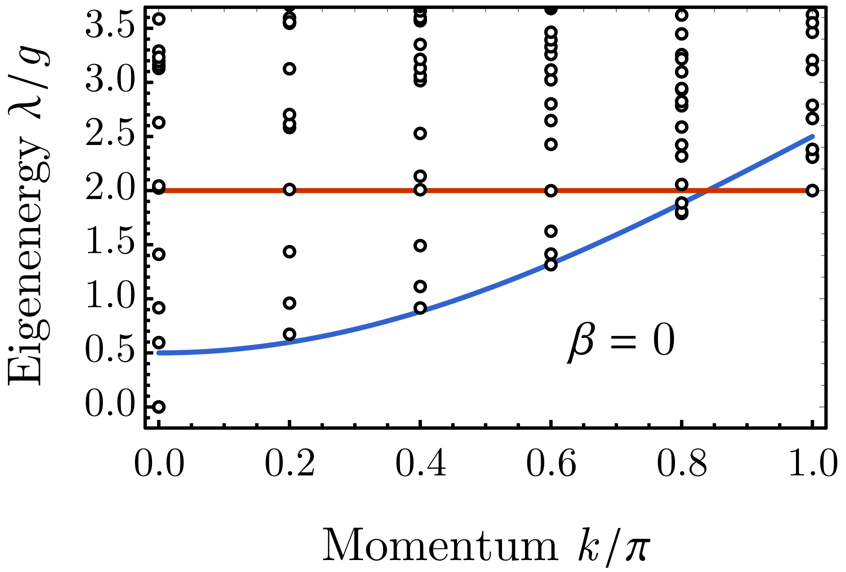

Figure 2.4. We perform exact diagonalization for the EF Hamiltonian $\hat{H}_{\mathrm{EF}}$ with $\beta = 0, L = 10$. Each small circle represents an eigenstate label by its eigenenergy λ and its crystal momentum k. The blue curve is the analytical result of two-domain-wall ansatz Eq. (2.52). The red curve is the analytical result of single spin-flip ansatz Eq. (2.54).

various momenta. The ED result indicates that the lowest-energy excited state mainly consists of two-domain-wall states, so we will focus on them in the following.

Based on the numerical observation, we approximate low energy excitation by the two-domain-wall (2DW) ansatz state as follows,

$$\langle k| \propto \sum_{i_1,i_2} e^{\mathrm{i}k\frac{i_1+i_2}{2}} \phi^*_{i_2-i_1} \langle i_1, i_2|, \tag{2.50}$$

where $\langle i_1, i_2| = \langle \Uparrow | \prod_{i=i_1}^{i_2-1} X_i$ is a two-domain-wall state with domain walls located at i_1 and i_2. k labels the center of mass momentum of the pair of domain walls. $\phi_{\Delta i}$ is a variational wave function that describes the relative motion between the domain walls. We can then evaluate the energy expectation value $\lambda(k)$ on the ansatz state $\langle k|$,

$$\lambda_{\mathrm{2DW}}(k) = \frac{\langle k|\hat{H}_{\mathrm{EF}}\hat{W}_{\mathbb{1}}|k\rangle}{\langle k|\hat{W}_{\mathbb{1}}|k\rangle}, \tag{2.51}$$

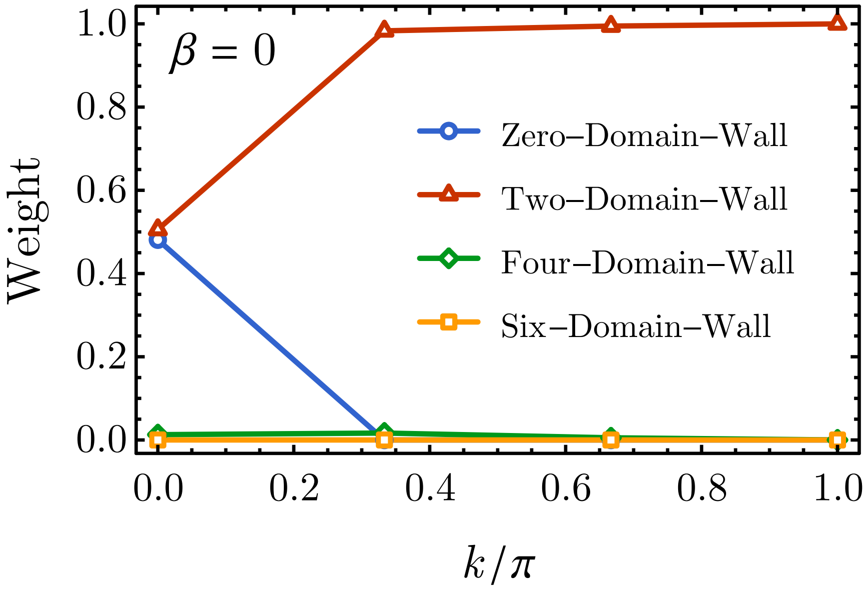

Figure 2.5. We perform exact diagonalization for the EF Hamiltonian $\hat{H}_{\mathrm{EF}}$ with $g = 1, \beta = 0, L = 6$. The weight is defined as follows: the left excited state $\langle L|$ can be expressed as the linear combination of two-, four- and six-domain-wall states with the coefficient (c_2, c_4, c_6). The weight of individual type is equal to $|c_n|^2$. For $k = 0$, zero-domain wall states take half of the weight in the lowest-energy excited state. However, they have no contribution in dispersion relation since their eigenenergy is zero.

where $\hat{W}_{\mathbb{1}}|k\rangle$ is understood as the corresponding right-state of the ansatz left-state $\langle k|$. Two assumptions are made to derive the analytical expression of the dispersion relation. The first assumption is that these domain walls have no interaction with each other and thus $\phi_{\Delta i}$ can be approximated by plane waves. The second assumption is the thermodynamic limit $L \to \infty$, which would simplify the calculation but suppress the contribution from short two-domain-wall states (see Appendix A.5 for details). Based on these assumptions, the dispersion relation for $\beta = 0$ can be derived as,

$$\lambda_{\mathrm{2DW}}(k) = 2g\left(1+\frac{1}{d^2}\right) - \frac{4g}{d}\cos\frac{k}{2} + \mathscr{O}(d^{-3}). \tag{2.52}$$

The band minimum is at $k = 0$, which defines the excitation gap

$$\Delta = \min_k \lambda(k) = 2g\left(1-\frac{1}{d}\right)^2 + \mathscr{O}(d^{-3}). \tag{2.53}$$

It turns out that the gap remains open (i.e. $\Delta > 0$) for any finite $g > 0$.

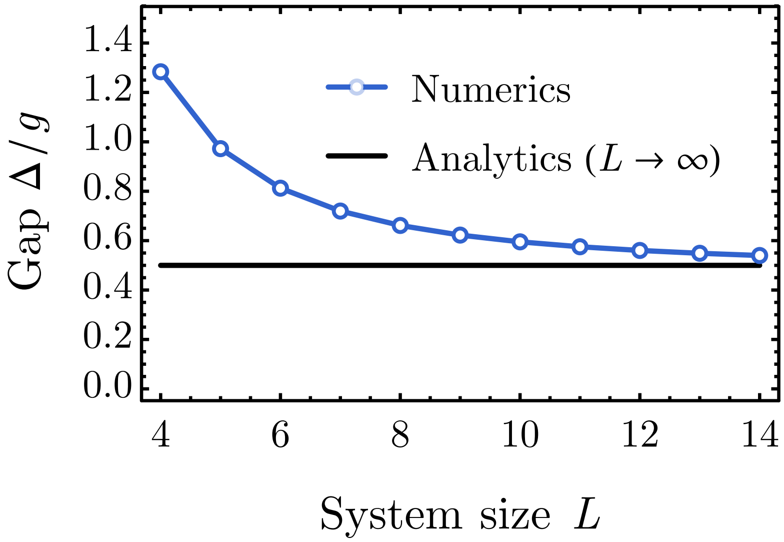

Figure 2.6. Comparison of the excitation gap between the finite-size ED result and the analytical result of two-domain-wall ansatz in the thermodynamic limit for the qudit dimension $d = 2$. The analytical result $\Delta = g/2$ is given by Eq. (2.53).

The comparison between ED result (black circles) and our analytical expression (blue curve) is shown in Fig. 2.4. The lower-edge of the excitation spectrum is pretty well captured by the two-domain-wall ansatz. The comparison also reveals a finite-size-effect in the spectrum. In Fig. 2.6, we show how the gap at $k = 0$ (from ED) approaches to the analytic result of Eq. (2.53) with increasing system size L. We also observe a systematic deviation of our analytical result from the excitation edge near $k = \pi$. The reason is that the eigenstate around $k = \pi$ is dominated by single-site excitations, where the domain-walls are next to each other such that their interaction can not be ignored. To capture the interaction effect, we switch to another ansatz state, which describes the motion of a tightly-bound domain-wall pair, or equivalently a single spin-flip (SSF) excitation (see Appendix A.6 for details). The dispersion of the SSF excitation reads

$$\lambda_{\text{SSF}}(k) = 2g, \tag{2.54}$$

which turns out to be independent of the qudit dimension d and the momentum k. This dispersion relation basically passes a series of points in Fig. 2.4 and only becomes the lowest excited state around $k = \pi$.

2.4 Applications and numerics

2.4.1 Models of locally scrambled quantum dynamics

In the following, we will apply the entanglement feature formalism to several scenarios of locally scrambled quantum dynamics. We will consider two types of models: random circuit models with discrete time as in Fig. 2.7(a), and Hamiltonian generated evolutions with local scramblers in the limit of continuous time as in Fig. 2.7(b). For the discrete time models, namely *locally scrambled random circuits*, we will adopt the transfer matrix method to study the entanglement dynamics. For the continuous time models, namely *locally scrambled Hamiltonian dynamics*, we will apply the EF Hamiltonian approach.

The random circuit we consider will be of the “brick wall” structure as shown in Fig. 2.7(a). The entire unitary circuit $U = \prod_t U_t$ is constructed by stacking layers of unitary gates.

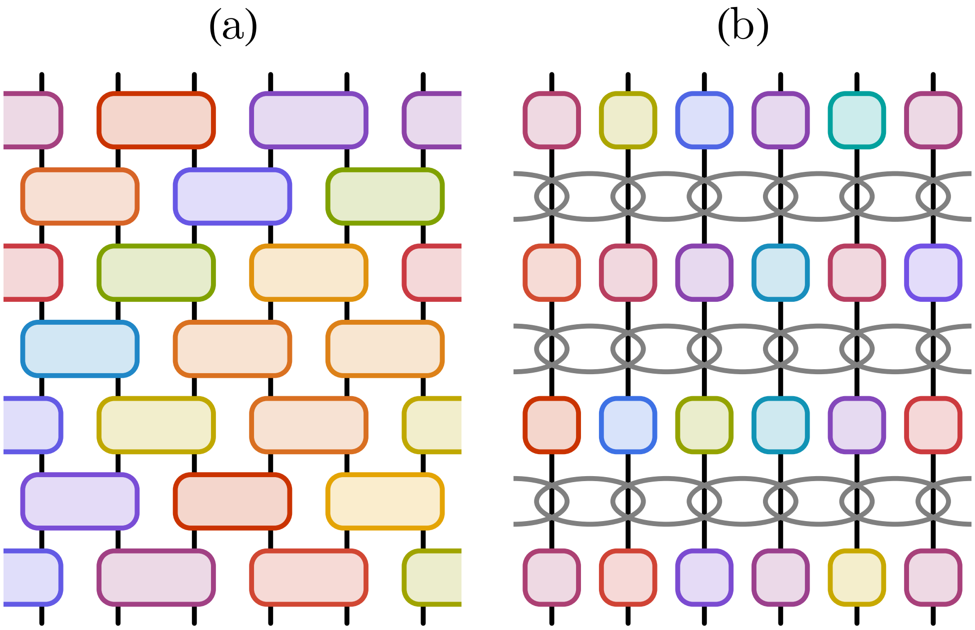

Figure 2.7. (a) Locally scrambled random circuit. The gates are drawn independently in both space and time (as indicated by different colors). (b) Locally scrambled Hamiltonian dynamics. The unitary operators generated by the local Hamiltonian are overlapping gray ovals in each layer. The on-site scramblers are uncorrelated in both space and time (as indicated by different colors).

Each layer U_t is described by

$$U_t = \begin{cases} \bigotimes_x U_{t;2x-1,2x} & t \in \text{odd}, \\ \bigotimes_x U_{t;2x,2x+1} & t \in \text{even}, \end{cases} \tag{2.55}$$

where $U_{t;ij}$ denotes the two-qudit unitary gate acting on sites i and j at time t. Each gate $U_{t;ij}$ is independently sampled from a locally scrambled unitary ensemble, so the quantum circuit U will be dubbed as a locally scrambled random circuit. In fact, any gate can be made locally scrambled by symmetrizing over local basis transformations as constructed in Eq. (2.18). The construction here is more general than the Haar random unitary circuit[28], as the unitary gate here does not need to be Haar random. As the quantum state evolves by $|\Psi_{t+1}\rangle = U_t|\Psi_t\rangle$, the corresponding EF state evolves by $|W_{\Psi_{t+1}}\rangle = \hat{T}_t|W_{\Psi_t}\rangle$. The transfer matrix $\hat{T}_t$ follows the same structure as U_t,

$$\hat{T}_t = \begin{cases} \bigotimes_x \hat{T}_{2x-1,2x} & t \in \text{odd}, \\ \bigotimes_x \hat{T}_{2x,2x+1} & t \in \text{even}. \end{cases} \tag{2.56}$$

According to Eq. (2.25), $\hat{T}_{ij}$ is fully determined by the EF of $U_{t;ij}$ via

$$\hat{T}_{ij} = \hat{W}_{U_{t;ij}} \hat{W}_{\mathbb{1}_{ij}}^{-1}. \tag{2.57}$$

Here we have assumed that $U_{t;ij}$ are drawn from identical unitary ensembles, such that $\hat{T}_{ij}$ is time-independent (despite of the time-dependence in $U_{t;ij}$). In the following, we will provide examples of the locally scrambled two-qudit unitary ensemble. We will use the transfer matrix approach to calculate the entanglement dynamics. The result will be compared with exact numerics by explicitly constructing the random circuit and average the final state EE over random realizations.

Another type of locally scrambled quantum dynamics that we will consider is generated by a local Hamiltonian $H = \sum_{\langle ij \rangle} H_{ij}$, which is a sum of local terms H_{ij} defined on nearest neighboring bonds $\langle ij \rangle$ along a 1D chain. Each step of the unitary evolution U_t is independently drawn from the locally scrambled unitary ensemble $\mathscr{E}_{e^{-\mathrm{i}\varepsilon H}}$ generated by the Hamiltonian H,

$$\mathscr{E}_{e^{-\mathrm{i}\varepsilon H}} = \{V^\dagger e^{-\mathrm{i}\varepsilon H} V | V = \bigotimes_{i=1}^{L} V_i, V_i \in \text{Haar}\}, \tag{2.58}$$

which may be simply denoted by $U_t = V_t^\dagger e^{-\mathrm{i}\varepsilon H} V_t$, as in Eq. (2.28). Combining the adjacent local scramblers following Eq. (2.22), the unitary evolution can be considered as repeatedly applying a short-time unitary evolution $e^{-\mathrm{i}\varepsilon H}$ followed by a layer of local scramblers, as illustrated in Fig. 2.7(b). Such dynamics will be called the locally scrambled Hamiltonian dynamics. It is similar to the Brownian random circuit model[66] in that each step of the evolution is driven by a different random Hamiltonian, but our construction is more general in that the random Hamiltonian ensemble only needs to be invariant under local basis transformations other than the full basis transformation of the many-body Hilbert space. For small ε, we can take the continuous time approach to calculate the entanglement dynamics by solving the imaginary-time Schrödinger equation $\partial_t |W_{\Psi_t}\rangle = -\hat{H}_{\text{EF}} |W_{\Psi_t}\rangle$ in Eq. (2.31). It worth mentioning that the locally scrambled quantum dynamics we considered here should be distinguished from Trotterizing a Hamiltonian dynamics. Here, the short-time evolutions $e^{-\mathrm{i}\varepsilon H}$ are interrupted by local scramblers, such that they do not combine to a coherent long-time evolution generated by the same Hamiltonian H. The local scramblers destroy the original notion of time. In the quantum dynamics, $e^{-\mathrm{i}\varepsilon H}$ advances the quantum state by ε in time, but after the insertion of layers of local scramblers, the entanglement dynamics only progress by ε^2, which is much slower. This phenomenon is analogous to the quantum Zeno effect due to the insertion of measurement. We conjecture that the local scramblers play a similar role as random local measurement in implementing random local basis transformations, such that the quantum dynamics is no longer coherent.

2.4.2 Locally scrambled random circuits

Let us first consider the locally scrambled random circuit as in Fig. 2.7(a). The building blocks of the random circuit are two-qudit unitary gates. Each gate is independently drawn from local basis-independent random ensembles. The EF of a two-qudit unitary operator U_{ij} is completely characterized by two parameters: the cross channel mutual information $I_{ij}^{\times}$ and the tripartite information $I_{ij}^{\triangledown}$. Let us label the input and output channels of the two-qudit unitary by A, B, C, D as shown in Fig. 2.8(a), then $I_{ij}^{\times}$ and $I_{ij}^{\triangledown}$ are defined as follows

$$\begin{aligned} I_{ij}^{\times} &= I^{(2)}(A:D) = I^{(2)}(B:C), \\ I_{ij}^{\triangledown} &= I^{(2)}(A:C) + I^{(2)}(A:D) - I^{(2)}(A:CD). \end{aligned} \tag{2.59}$$

The mutual information, such as $I^{(2)}(A:D) = S_A^{(2)} + S_D^{(2)} - S_{AD}^{(2)}$, is understood by treating the unitary gate as a quantum state by bending the input and output legs to the same side, and calculating the operator EE following the definition in Ref. [23, 44].

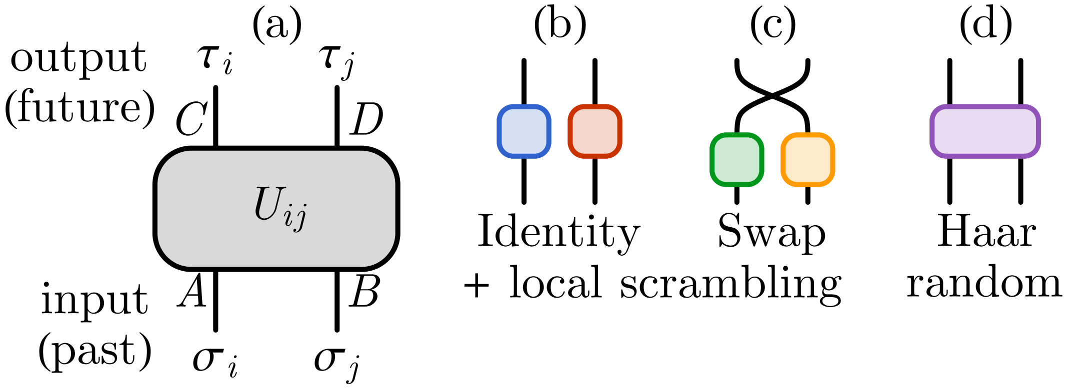

Figure 2.8. (a) A generic two-qudit gate acting on qudits i and j. The input channels are labeled by A and B, and the output channels are labeled by C and D. The EF of the gate will be labeled by the Ising configuration $\boldsymbol{\sigma} = (\sigma_i, \sigma_j)$ on the input side and $\boldsymbol{\tau} = (\tau_i, \tau_j)$ on the output side. (b-d) Examples of local basis independent ensembles of two-qudit gates: (b) identity gate with local scrambling, (c) swap gate with local scrambling, (d) Haar random unitary gate acting on both qudit (local basis automatically scrambled).

In terms of these information measures $I_{ij}^{\times}$ and $I_{ij}^{\triangledown}$ of the unitary gate U_{ij}, the EF operator

$\hat{W}_{U_{ij}}$ is given by

$$\begin{aligned} \hat{W}_{U_{ij}} &= d^2(d+X_i)(d+X_j) \\ &\quad - \frac{1-Z_iZ_j}{2}(A_{ij} - B_{ij}X_iX_j), \\ A_{ij} &= d^4(1-e^{I_{ij}^{\triangledown} - I_{ij}^{\times}}), \\ B_{ij} &= d^2(e^{I_{ij}^{\times}} - 1). \end{aligned} \tag{2.60}$$

The cross channel mutual information $I_{ij}^{\times} \geq 0$ is non-negative by the subadditivity[67] of entropy. It describes the entanglement propagation, as it measures the amount of information transferred between site i and j. The tripartite information $I_{ij}^{\triangledown}$ must be negative for unitary gates[23], and therefore $I_{ij}^{\times} - I_{ij}^{\triangledown} \geq 0$ holds. The negative tripartite information $(-I_{ij}^{\triangledown})$ is proposed[23] to be a description of information scrambling, since it measures the amount of information about A that is encoded in C and D jointly but can not be told by local measurements exclusively performed on C or D.

To gain more intuition about $I_{ij}^{\times}$ and $I_{ij}^{\triangledown}$, let us provide a few examples of local basis independent ensembles of two-qudit gates, as pictured in Fig. 2.8(b-d).

- Identity gate with local scrambling, i.e. two on-site Haar random unitary gates direct product together, as Fig. 2.8(b). In this rather trivial case, we have

  $$I_{ij}^{\times} = I_{ij}^{\triangledown} = 0, \tag{2.61}$$

  such that the EF operator in Eq. (2.60) reduces to $\hat{W}_{\mathbb{1}} = d^2(d+X_i)(d+X_j)$, consistent with the previous result in Eq. (2.15) by direct evaluation.

- Swap gate with local scrambling, i.e. two on-site Haar random unitary gates followed by an inter-site swap operator, as Fig. 2.8(c). In this case,

  $$I_{ij}^{\times} = 2\log d, \quad I_{ij}^{\triangledown} = 0, \tag{2.62}$$

such that the EF operator in Eq. (2.60) reduces to

$$\begin{aligned}\hat{W}_{\text{swap}} = d^2(d+X_i)(d+X_j)\\ -d^2(d^2-1)\frac{1-Z_iZ_j}{2}(1-X_iX_j).\end{aligned} \tag{2.63}$$

The swap gate can generate and propagate quantum entanglement due to the non-vanishing cross channel information $I_{ij}^{\times}$. But there is no information scrambling happening *between* the qudits (despite of the sufficient on-site scrambling), because the qubits are simply interchanged by the swap gate, such that local operators do not spread out other than being moved around in the space. The zero scrambling power of the swap gate is reflected in the zero tripartite information $I_{ij}^{\triangledown}$.

- Haar random unitary gate acting on the two qudits, as Fig. 2.8(d). In this case,

$$I_{ij}^{\times} = \log\frac{2d^2}{d^2+1}, \quad I_{ij}^{\triangledown} = \log\frac{4d^2}{(d^2+1)^2}, \tag{2.64}$$

  such that the EF operator in Eq. (2.60) reduces to $\hat{W}_{\text{Haar}}$ given in Eq. (2.13), see Appendix A.2 for derivation. The Haar random unitary gate not only propagates quantum entanglement, but also scrambles the quantum information efficiently, as it has a negative tripartite information $I_{ij}^{\triangledown}$ (as long as $d > 1$).

The above are examples of locally scrambled random unitary ensembles. Unitary gates drawn from such ensembles serve as the building block of locally scrambled random circuits. The entanglement dynamics of locally scrambled random circuits can be universally described by the transfer matrix approach as has been discussed in Sec. 2.4.1. On the level of EF, the formulation is exact: the evolution of the average state EF can be precisely calculated from $|W_{\Psi_{t+1}}\rangle = \hat{W}_{U_t}\hat{W}_{\mathbb{1}}^{-1}|W_{\Psi_t}\rangle$ given the EF of the unitary. However, when applying the result to predict the EE, we rely on the assumption that the average EE can be approximated by the negative log of average EF following Eq. (2.27), where we effectively switch the order between the ensemble average and the logarithm. One major goal of the following is to provide numerical evidences to check this assumption in various different cases. It turns out that the negative log of EF generally provides a good estimate of the averaged EE, which makes our EF formulation useful in describing the entanglement dynamics for a broad class of random unitary circuits.

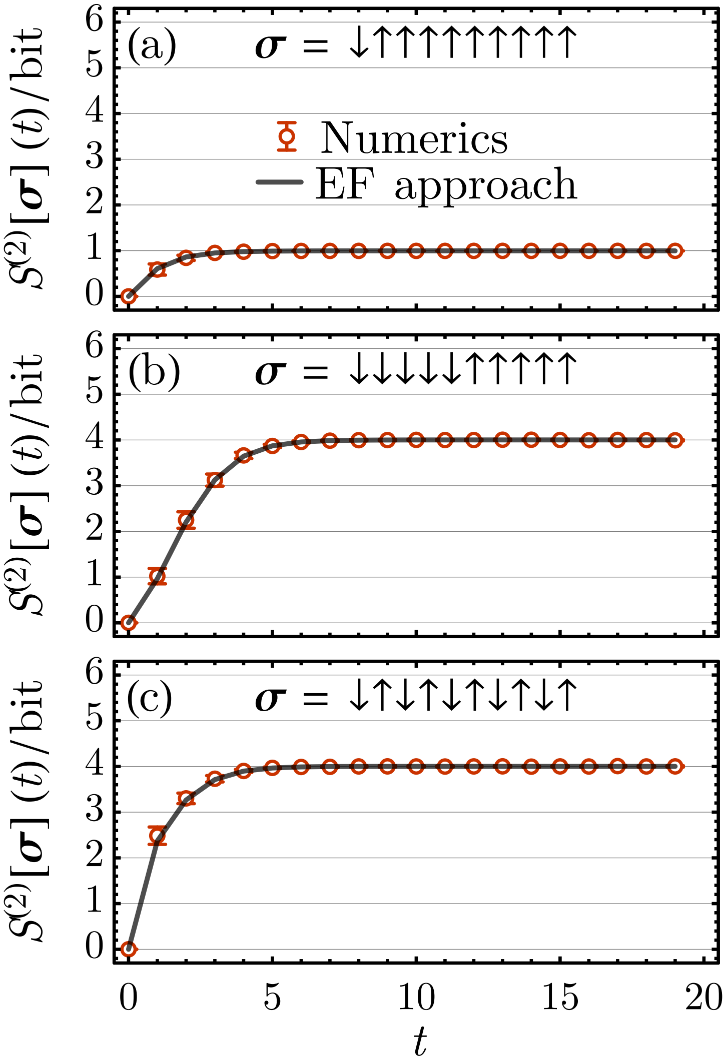

Figure 2.9. The finial state EE of the Haar random circuit on a 10-site system for different choices of the entanglement regions: (a) single site, (b) half-system, (c) alternating[1]. The qudit dimension is $d = 2$ and the entropy is measured in unit of bit ($= \log 2$).

Our first example is the standard Haar random unitary circuit, where each two-qudit gate is drawn from Haar random unitary ensemble independently. The model has be extensively studied in the literature,[28, 31, 35, 32] and the statistical mechanical model description has been developed by Zhou and Nahum in their pioneering work Ref. [40]. We revisit this model to show that our formalism is equivalent to the Zhou-Nahum approach and can reproduce the known behaviors. Let us first calculate the transfer matrix $\hat{T}_{ij}$ of a single Haar random unitary gate U_{ij} from its EF. Based on Eq. (2.13) and Eq. (2.17), we obtain

$$\hat{T}_{ij} = \hat{W}_{\text{Haar}} \hat{W}_{\mathbb{1}}^{-1} = \Big(1 + \frac{d(X_i + X_j)}{d^2+1}\Big)\frac{1+Z_iZ_j}{2}. \tag{2.65}$$

Using the Ising basis $|\sigma_i\sigma_j\rangle$, Eq. (2.65) can be expressed as

$$\begin{aligned}\hat{T}_{ij} = &|\uparrow\uparrow\rangle\langle\uparrow\uparrow| + \frac{d}{d^2+1}(|\uparrow\downarrow\rangle\langle\uparrow\uparrow| + |\downarrow\uparrow\rangle\langle\uparrow\uparrow|)\\ &+ |\downarrow\downarrow\rangle\langle\downarrow\downarrow| + \frac{d}{d^2+1}(|\downarrow\uparrow\rangle\langle\downarrow\downarrow| + |\uparrow\downarrow\rangle\langle\downarrow\downarrow|),\end{aligned} \tag{2.66}$$

which is equivalent to the triangle weights ▽ $= 1$ and ▽ $=$ ▽ $= d/(d^2+1)$ that defines the Ising model in Ref. [40]. An equivalent form of the transfer matrix Eq. (2.65) was previously obtained in Ref. [68]. Plugging Eq. (2.65) into Eq. (2.56), we obtain the transfer matrix $\hat{T}_t$ that describes the EF state evolution under the quantum dynamics of the Haar random circuit. We assume the initial state is a product state, s.t. $|W_0\rangle = |W_{\text{prod}}\rangle$. We evolve the EF state by Eq. (2.24). We can then compute the EE following Eq. (2.27) and compare the result with the numerical simulation. In the simulation, we applied randomly sampled unitary gates to an initial product state and measured the final state EE, then performed the ensemble average of the EE. As shown in Fig. 2.9, the EF approach provides pretty precise prediction of the EE that matches the numerical result.

Now let us turn to a new example of locally scrambled random circuits, namely the swap gate circuit, which is designed to mimic the entanglement dynamics in integrable conformal field theories (CFT) where entanglement spreads with the propagation of quasi-particles.[8, 44, 45] The circuit takes the architecture of the brick wall circuit in Fig. 2.7(a) with gates drawn from the locally scrambled swap gate ensemble in Fig. 2.8(c), the resulting circuit is equivalent to

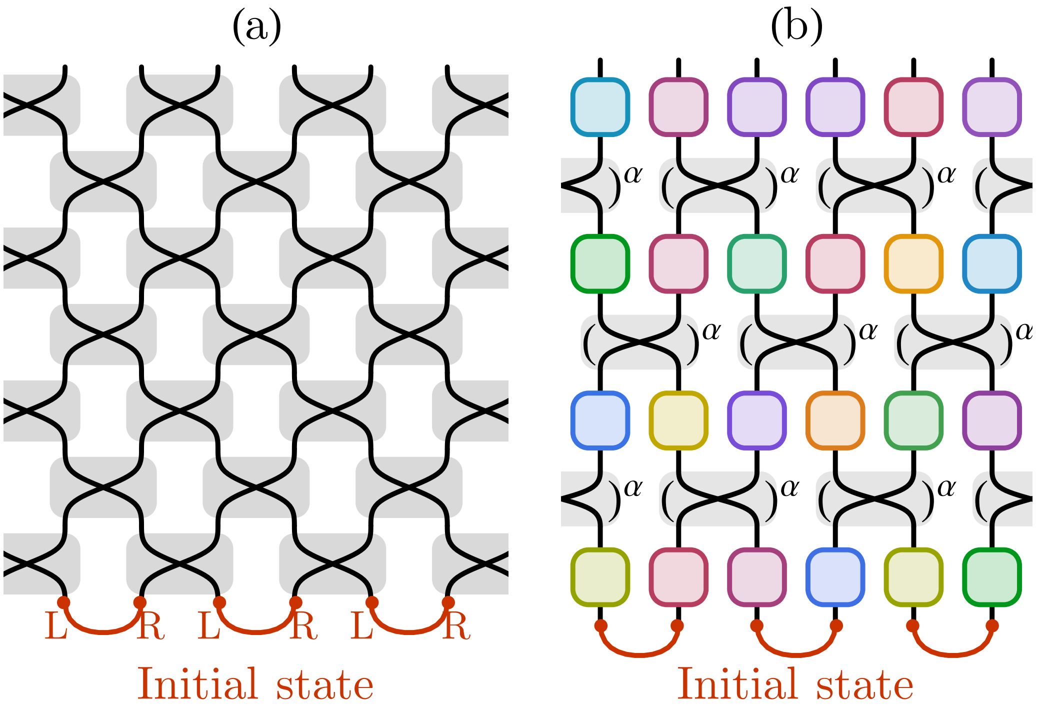

Figure 2.10. (a) Swap gate circuit. Gray blocks mark out the swap gates. (b) Locally scrambled fractional swap gate circuit. Each swap gate is powered by the fraction $0 < \alpha < 1$.

an interweaving network as shown in Fig. 2.10(a). The local scramblers in different layers can commute through the swap gates and combine to a single scrambling layer acting on the initial state, which can further be dropped as long as the initial state ensemble is already local basis invariant. For this model, we use a different initial state other than the product state. As illustrated in Fig. 2.10(a), the initial state is chosen to be a product of Einstein-Podolsky-Rosen (EPR) pairs arranged along a one-dimensional chain, whose EF can be described by

$$|W_0\rangle = \prod_x \Big(1 + \frac{1}{d}X_{2x-1} + \frac{1}{d}X_{2x} + X_{2x-1}X_{2x}\Big)|\Uparrow\rangle. \tag{2.67}$$

For each EPR pair, the qudit labeled by L (or R) will travel to the left (or right) in the swap gate circuit, which mimics the behaviors of left (or right) moving quasi-particles in an integrable CFT. In this way, entanglement spread out along the chain as EPR pairs stretch out, following the steps depicted in Fig. 2.11. On a finite-sized chain with periodic boundary condition, we expect to observe the half-system entanglement entropy to first grow and then decrease in time, and continue to oscillate like this. This recurrent behavior can be perfectly produced by the EF formulation, because, based on Eq. (2.63), the transfer matrix for a single swap gate turns out to be

$$\hat{T}_{ij} = \hat{W}_{\text{swap}}\hat{W}_{\mathbb{1}}^{-1} = \frac{1}{2}(1 + X_iX_j + Y_iY_j + Z_iZ_j), \tag{2.68}$$

which is precisely the swap operator for Ising spins. In this way, the permutation of entangled qudits under the quantum dynamics is equivalently modeled by the permutation of correlated Ising spins in the EF formulation.

The recurrent (periodically oscillating) behavior of the half-system EE is demonstrated in Fig. 2.12(a), where the EF approach matches the numerical simulation perfectly. The periodic recurrence of the low-entanglement state in the swap gate circuit seems to contradict with our previous conclusion in Sec. 3.3 that locally scrambled quantum dynamics generally thermalize. The swap gate circuit evades thermalization because its corresponding EF transfer matrix admits

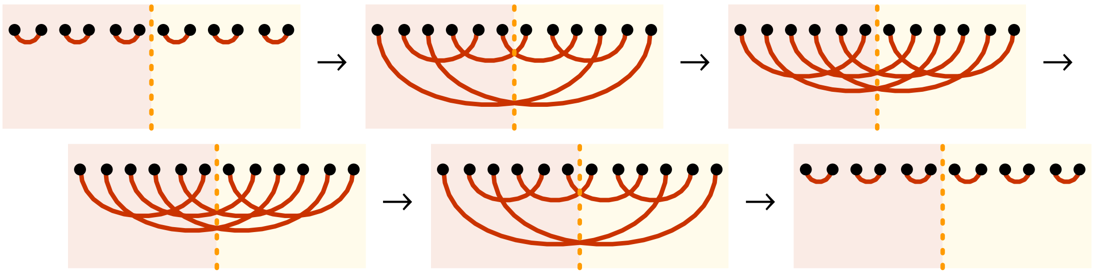

Figure 2.11. Evolution of EPR pairs under the swap gate circuit on a 12-site chain with periodic boundary condition. The entanglement entropy between the left- and right-half system is proportional to the EPR pairs across the cut (indicated by dotted vertical line).

more than one leading eigenstate. Let $\hat{T} = \bigotimes_x \hat{T}_{2x-1,2x} \bigotimes_x \hat{T}_{2x,2x+1}$ be two steps (one period) of the transfer matrix that translates the L (or R) sublattice to the left (or right) by one unit-cell. On a chain of $2n$ sites, the operator $\hat{T}$ has $n^{-1}\sum_{d|n}\varphi(d)4^{n/d}$ fold degenerated eigenstates of eigenvalue 1, with $\varphi(d)$ being the Euler totient function and d running over all divisors of n. These eigenstates can be constructed by taking any Ising basis state and symmetrizing over the cyclic group generated by $\hat{T}$. Their degeneracy can be counted by mapping the problem to the number of n-bead necklaces with four colors,[69] where the four colors correspond to the four choices of $\uparrow\uparrow, \uparrow\downarrow, \downarrow\uparrow, \downarrow\downarrow$ configurations in each unit-cell. Therefore the Page state is not the unique state that can survive in the long-time limit, and thermalization is not the ultimate fate.

The swap gate circuit model can be generalized by introducing the *fractional swap gate* that interpolates between the identity gate and the swap gate. The fractional swap gate can be written as a fractional power α of the swap gate with $0 < \alpha < 1$

$$\mathsf{SWAP}^{\alpha} = \frac{1+e^{i\alpha\pi}}{2} \parallel + \frac{1-e^{i\alpha\pi}}{2} \times . \tag{2.69}$$

The fractional swap gate reduces to the identity gate (or the swap gate) at $\alpha = 0$ (or $\alpha = 1$). But unlike both identity and swap gates which do not scramble quantum information between the two qudits, the fractional swap gate does have finite scrambling power. We can construct a locally scrambled fractional swap gate circuit by starting from the architecture of the random

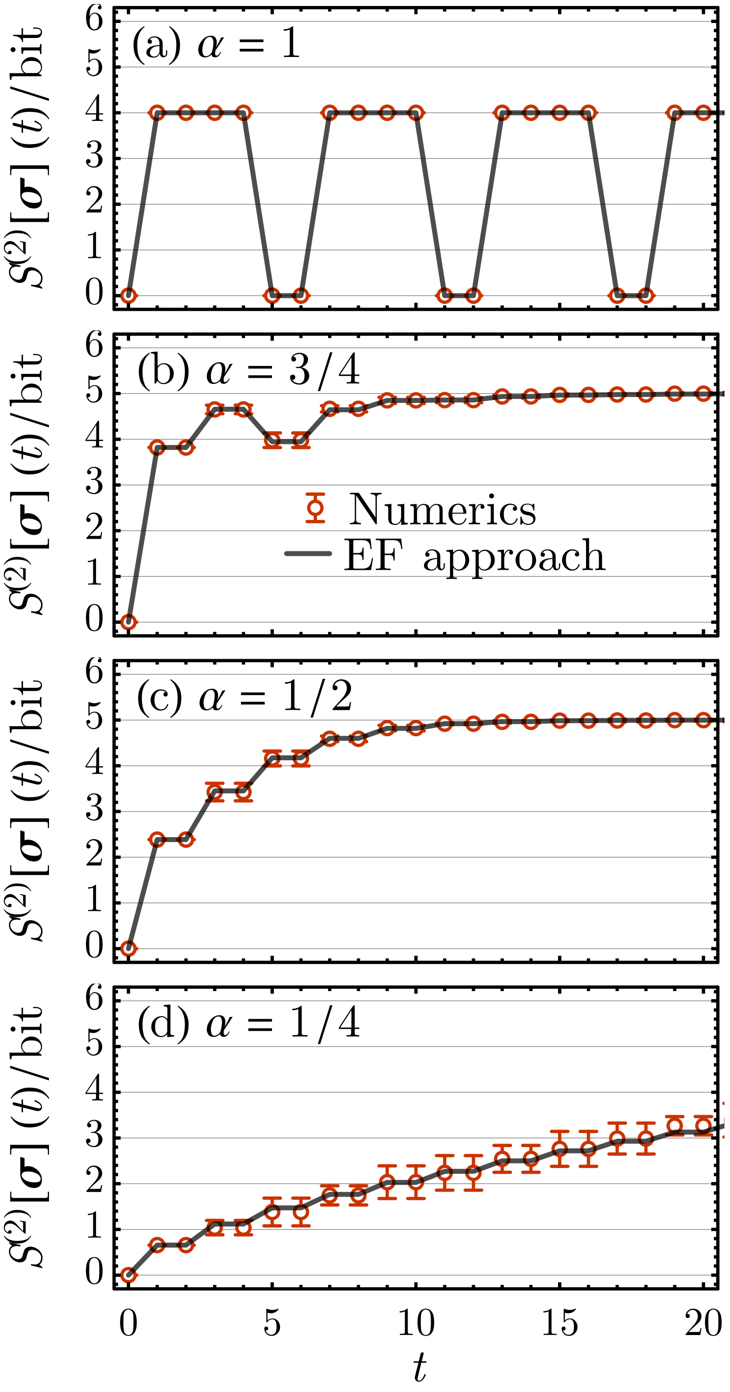

Figure 2.12. Half-system entanglement entropy of the locally scrambled fractional swap gate circuit on a 12-site system with different fraction α: (a) $\alpha = 1$, (b) $\alpha = 3/4$, (c) $\alpha = 1/2$, (d) $\alpha = 1/4$. The model is realized on a 12-site chain with periodic boundary condition. The entanglement region is chosen to be the first 6 sites. The qudit dimension is $d = 2$ and the entropy is measured in unit of bit ($= \log 2$).

circuit in Fig. 2.7(a) and sampling every gate independently from local basis invariant fractional swap gate ensemble, as illustrated in Fig. 2.10(b). The EF operator of the fractional swap gate follows the general form of Eq. (2.60) with parameters A_{ij} and B_{ij} given by

$$\begin{aligned} A_{ij} &= d^2(d^2-1)\frac{3+\cos\alpha\pi}{2}\sin^2\frac{\alpha\pi}{2}, \\ B_{ij} &= d^2(d^2-1)\sin^4\frac{\alpha\pi}{2}. \end{aligned} \tag{2.70}$$

Based on this result, the corresponding transfer matrix $\hat{T}_{ij}$ can be constructed by Eq. (2.57) and the evolution of the EF state can be calculated following the transfer matrix approach described in Eq. (2.56). In Fig. 2.12(b-d), we compare the EE calculated based on the EF approach with the ensemble averaged EE from numerical simulation. They match perfectly for different values of α. Because the fractional swap gate has finite scrambling power, the recurrence behavior no longer persist and the system can now thermalize. The entanglement dynamics is somewhat between that of the swap gate circuit and the Haar random circuit, in that the EE grows mostly linearly in time with small oscillations, until the EE eventually saturates to the thermal limit. As α becomes small, the system will take longer time (more steps) to thermalize. As shown in Fig. 2.12(d), the oscillation of EE is suppressed and its growth curve is more smooth. In the $\alpha \to 0$ limit, the entanglement dynamics approaches the continuum limit that can be described by the EF Hamiltonian, which is the topic of the following discussion.

2.4.3 Locally scrambled Hamiltonian dynamics

Now we turn to the locally scrambled Hamiltonian dynamics as illustrated in Fig. 2.7(b). We consider the local Hamiltonian $H = \sum_{\langle ij \rangle} H_{ij}$ and assume that H_{ij} on every bond is drawn from a local-basis-independent ensemble of two-qudit Hermitian operators. Equivalently, we can choose H to be a fixed Hamiltonian and construct a locally scrambled unitary ensemble $\mathscr{E}_{e^{-\mathrm{i}\epsilon H}}$ by applying local basis transformations following Eq. (2.58). The quantum dynamics is described by the unitary

$$U=\prod_t\big(V_te^{-\mathrm{i}\varepsilon H}\big), \tag{2.71}$$

where V_t describe the layer of local scramblers at time t, as illustrated in Fig. 2.7(b). The corresponding entanglement dynamics is described by the imaginary-time Schrödinger equation Eq. (2.31), where the EF Hamiltonian takes the form of

$$\hat{H}_{\mathrm{EF}}=\sum_{\langle ij\rangle}g_{ij}\frac{1-Z_iZ_j}{2}e^{-\beta_{ij}X_iX_j-\delta(X_i+X_j)}. \tag{2.72}$$

It turns out that the parameters $\beta_{ij}\sim\mathscr{O}(\varepsilon^2)$ always vanish in the $\varepsilon\to 0$ limit. The parameters g_{ij} are the only non-trivial parameters to the leading order of ε, which are determined by the local terms H_{ij} in the Hamiltonian

$$\begin{aligned}g_{ij}=&\frac{2}{d^2(d^2-1)}\big((\operatorname{Tr}H_{ij})^2+d^2\operatorname{Tr}(H_{ij}^2)\\&-d\operatorname{Tr}_j(\operatorname{Tr}_iH_{ij})^2-d\operatorname{Tr}_i(\operatorname{Tr}_jH_{ij})^2\big).\end{aligned} \tag{2.73}$$

The detailed derivation of these results can be found in Appendix A.7.

One well-studied example of the locally scrambled Hamiltonian dynamics is the Brownian random circuit,[66] where each step of the time evolution is generated by a random Hamiltonian drawn from the Gaussian unitary ensemble (GUE). The Hamiltonian can be written as a random U(d) spin model,

$$H_t=\sum_{\langle ij\rangle}J_{t,ij}^{ab}T_i^aT_j^b, \tag{2.74}$$

where T_i^a (for $a=1,2,\cdots,d^2$) are U(d) generators on site i with $\operatorname{Tr}T_i^{a\dagger}T_i^b=\delta^{ab}$. The coupling $J_{t,ij}^{ab}$ are independently drawn for each time t and indices i,j,a,b from the Gaussian distribution with zero mean and d^{-2} variance. The quantum dynamics is described by $U=\prod_t e^{-\mathrm{i}\varepsilon H_t}$. The operator growth dynamics and the spectral form factor of the Brownian random circuit has been investigated in Ref. [70, 71, 72, 73] recently, where differential equations governing the evolution of operator weight distribution were derived. Our approach also applies to the Brownian circuit model and results in similar differential equations for the evolution of EF state, whose EF Hamiltonian reads (see Appendix A.7 for derivation)

$$\hat{H}_{\mathrm{EF}} = \frac{2(d^2-1)}{d^2} \sum_{\langle ij \rangle} \frac{1 - Z_i Z_j}{2} e^{-\delta(X_i + X_j)}. \tag{2.75}$$

We will not discuss this model in further details, given the extensive study of Brownian circuits in the literature. Instead, we will consider a new type of locally scrambled Hamiltonian dynamics.

We start with a fixed Hamiltonian on the one dimensional chain of qudits

$$H = -\sum_{\langle ij \rangle} T_i T_j, \tag{2.76}$$

where T_i is one particular traceless Hermitian operator on site i that squares to identity (i.e. $\operatorname{Tr} T_i = 0$ and $T_i^2 = 1$). For the qubit case ($d = 2$), Eq. (2.76) reduces to an Ising model. Note that there is no randomness in the Hamiltonian H. The randomness will be introduced by the local scramblers, when we use H to generate the locally scrambled Hamiltonian dynamics following Eq. (2.71). The entanglement dynamics will be described by the following EF Hamiltonian

$$\hat{H}_{\mathrm{EF}} = \frac{2d^2}{d^2-1} \sum_{\langle ij \rangle} \frac{1 - Z_i Z_j}{2} e^{-\delta(X_i + X_j)}, \tag{2.77}$$

which takes the same form as Eq. (2.75) but with a different parameter g. We can test the EF approach with numerical simulation on a 12-qubit system with the choice of $\varepsilon = 0.01$. We start with a product state $|W_{\Psi_0}\rangle = |W_{\mathrm{prod}}\rangle$, evolve the EF state by Eq. (2.31) and calculate the EE from Eq. (2.27). The result is shown in Fig. 2.13. We can see that the averaged EE obtained from numerics matches well with the result of the EF approach over different choices of the entanglement regions. These numerical evidences suggest that exchanging the order between taking ensemble average and taking logarithm does not seem to matter much, so the evolution equation we established for the EF in this work can provide reliable descriptions for the entanglement dynamics under locally scrambled quantum dynamics. Comparing Fig. 2.13 with Fig. 2.9, one can see that the entanglement dynamics of the locally scrambled Hamiltonian dynamics closely resembles that of the Haar random unitary circuit. Thus the former can be considered as a continuum limit of the later.

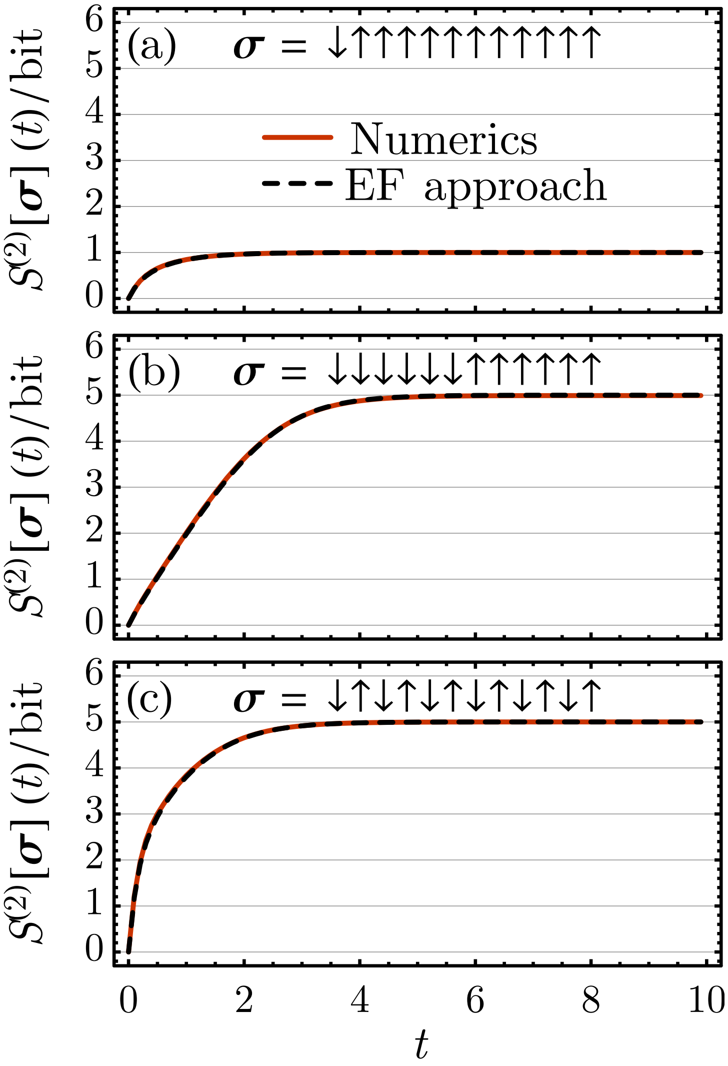

Figure 2.13. The final state EE of the locally scrambled Hamiltonian dynamics on a 12-site system for different choices of the entanglement regions: (a) single site, (b) half-system, (c) alternating [1]. The qudit dimension is $d = 2$ and the entropy is measured in unit of bit ($= \log 2$).

We also notice that, in agreement with the imaginary time EF Schrödinger equation, the

EE always approaches to its final thermalized value exponentially with the same relaxation time τ independent of the choice of the entanglement region,

$$S^{(2)}[\boldsymbol{\sigma}](t) \to S^{(2)}[\boldsymbol{\sigma}](\infty) - A[\boldsymbol{\sigma}]e^{-t/\tau}. \tag{2.78}$$

The relaxation time τ is intrinsically related to the excitation gap Δ of the EF Hamiltonian $\hat{H}_{\text{EF}}$, which can be estimated by Eq. (2.53) in the thermodynamic limit,

$$\tau^{-1} = \Delta = 2g\left(1 - \frac{1}{d}\right)^2 = \frac{4}{3}, \tag{2.79}$$

where the coupling g, according to Eq. (2.77), is given by $g = 2d^2/(d^2-1) = 8/3$ for qubits ($d = 2$). To check this prediction, we fit the numerical simulation data using Eq. (2.78) in the late-time regime to extract the excitation gap Δ. As shown in Fig. 2.14, the EE approaches to the thermal value with the same rate (within error bars) regardless of the different choice of entanglement regions. The numerically fitted gap is around $\Delta = 1.48$, which is close to the thermodynamic-limit analytic prediction $\Delta = 4/3 = 1.33$. The small discrepancy mainly arises from the finite-size effect. If we use the finite-size gap formula $\Delta = 0.56g$ based on the ED result in Fig. 2.6 at the system size $L = 12$, we will obtain a better prediction of the gap $\Delta = 1.49$, which matches the simulation result perfectly.

2.5 Summary and discussions

In this work, we introduced the concept of locally scrambled quantum dynamics, where each step of the unitary evolution is randomized by local scramblers (on-site Haar random unitary gates). Surrounding each unitary gate in a quantum circuit by local scramblers effectively blocks the local-basis-specific quantum information from propagating in the circuit and decouples the gates from each other under ensemble average. In this way, the average EF of the entire circuit can be constructed piece-by-piece from the EF of each gate, which makes the entanglement

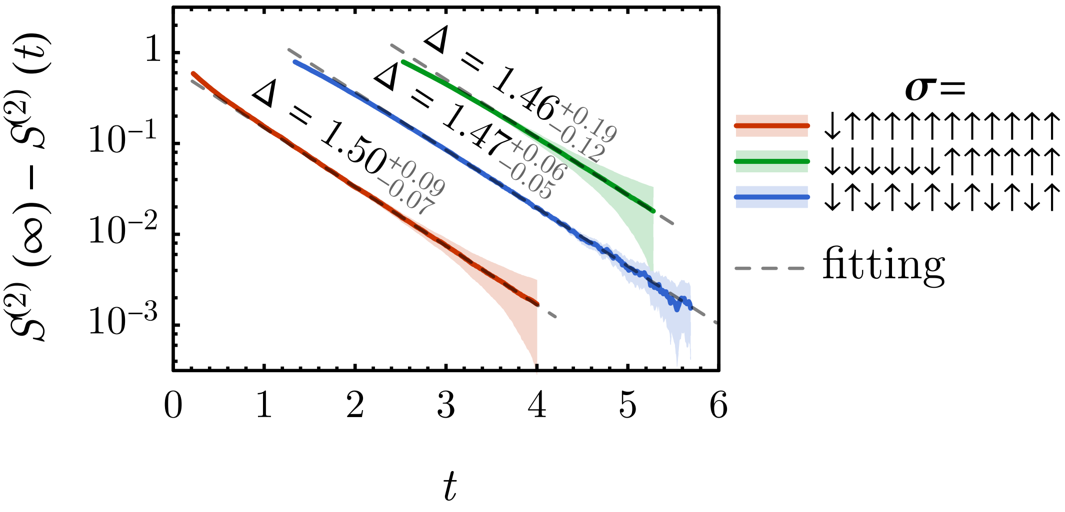

Figure 2.14. The difference between the EE and its final saturation value, i.e. $A[\boldsymbol{\sigma}]e^{-t/\tau}$, plot in the logarithmic scale vs time t. Different colors correspond to different choices of entanglement region (labeled by $\boldsymbol{\sigma}$). The shaded region indicates the error interval. The excitation gap $\Delta = \tau^{-1}$ is extracted by fitting the decay rate.

dynamics Markovian and enables us to write down the evolution equation for the EF of quantum states. The framework provides us the freedom to design the EF for each gate, such that we can go beyond the conventional Haar random gates and build the random circuit with more general random gates as long as their ensemble is local-basis-independent. This enables us to define and explore the continuum limit of locally scrambled quantum dynamics, under which the evolution of the EF state will be governed by an EF Hamiltonian. We obtained the general form of the EF Hamiltonian on symmetry ground and discussed the implication of its spectral properties on the entanglement dynamics. When the EF Hamiltonian is *gapped*, the excitation modes in the EF state will decay exponentially in time $W_{|\Psi\rangle} = e^{-S} \sim e^{-t/\tau}$, which corresponds to a linear growth of EE in time, i.e. $S \sim t/\tau$, as the system thermalizes. What has not been much discussed previously is the possibility that the EF Hamiltonian can become *gapless* under fine-tuning, then the EF will decay in a power-law manner $W_{|\Psi\rangle} = e^{-S} \sim t^{-\alpha}$, which corresponds to a logarithmic growth of EE, i.e. $S \sim \alpha \log t$. Such scenario could happen at entanglement transitions,[42, 58, 57] where the entanglement scaling of the long-time final state switches from volume-law to area-law. The transition can be interpreted as an order to disorder phase transition of the EF Hamiltonian. One interesting future direction is to explore different models of the EF Hamiltonian and to map out the phase diagram using analytical and numerical tools developed in quantum many-body physics.

Although we focused on the entanglement dynamics of pure states in this work, the EF formulation can be easily generalized to describe mixed state or operator entanglement. Following Eq. (2.4), it is straight forward to define the EF $W_O[\boldsymbol{\sigma}]$ for any many-body operator O (including the density matrix ρ as a special case),

$$W_O[\boldsymbol{\sigma}] = \mathrm{Tr}(\mathscr{X}_{\boldsymbol{\sigma}} O^{\otimes 2}), \tag{2.80}$$

and quantize the EF to a state $|W_O\rangle = \sum_{[\boldsymbol{\sigma}]} W_O[\boldsymbol{\sigma}]|\boldsymbol{\sigma}\rangle$. Suppose the operator evolves in time under a locally scrambled quantum dynamics $O' = UOU^\dagger$, the average EF will still be described by the same set of equation $|W_{O'}\rangle = \hat{W}_U \hat{W}_{\mathbb{1}}^{-1} |W_O\rangle$ as Eq. (2.19). Based on this, all the dynamic equation that we developed in this work applies directly, such that we do not need to derive a new set of equations for operator dynamics. The EF state $|W_O\rangle$ encodes the operator EE[29] over all possible regions, which can be used to construct various quantities characterizing the operator size. To name a few, let us first assume O to be a traceless Hermitian operator normalized to $\mathrm{Tr}\, O^2 = d^L$. We can decompose the operator $O = \sum_{[a]} O_{[a]} T^{[a]}$ in the operator basis $T^{[a]} = \prod_i T_i^{a_i}$ (where T_i^a denotes the $\mathrm{SU}(d)$ generator on the ith qudit), and define the operator weight $p_{[a]} = O_{[a]}^2$.[32, 35, 70, 72] The fraction of the operator in a subsystem A then reads $p_A = \sum_{[a] \in A} p_{[a]}$,[3] which can be extracted from the EF state $|W_O\rangle$ by taking its inner product with a state $|P_A\rangle$ that labels the subsystem A:

$$p_A = \langle P_A | W_O \rangle, \quad |P_A\rangle = \frac{1}{d^{2L}} \prod_{i \in A} (dX_i - 1) |\Uparrow\rangle. \tag{2.81}$$

---

[3] The notation $\sum_{[a] \in A} = \prod_{i \in A} \sum_{a_i=1}^{d^2-1}$ denotes the summation over the operator configuration $[a]$ which is non-trivial in region A.

The fraction p_A can be further used to characterize the average operator size $\ell_O = \sum_A p_A |A|$. The evolution equation for p_A under Brownian dynamics is recently discussed in Ref. [70, 72]. Another way to probe $|W_O\rangle$ is to consider the variance of the expectation value of O on random mixed states ρ, i.e. $\text{var}_\rho \langle O \rangle_\rho = \mathbb{E}_\rho (\text{Tr}\, \rho O)^2$. Suppose ρ is drawn from a local-basis-independent ensemble characterized by its EF state $|W_\rho\rangle$, then the variance of operator expectation value is given by

$$\text{var}_\rho \langle O \rangle_\rho = \langle W_\rho | \hat{W}_{\mathbb{1}}^{-1} | W_O \rangle. \tag{2.82}$$

It was recently pointed out by Ref. [74] that $\text{var}_\rho \langle O \rangle_\rho = \sum_A p_A (d+1)^{-|A|}$ can be expressed in terms of p_A, if ρ is uniformly sampled from the ensemble of pure product states. The fact that $\text{var}_\rho \langle O \rangle_\rho$ and p_A are related to each other is less surprising in the EF formulation, because they are simply two different ways to probe the same EF state $|W_O\rangle$. The evolution equation of $|W_O\rangle$ under locally scrambled quantum dynamics is identical to that of $|W_\Psi\rangle$, from which the evolution equations of p_A, ℓ_O or $\text{var}_\rho \langle O \rangle_\rho$ follow automatically. In this way, the EF formulation developed in our work provides a unified framework to discuss various aspects of the operator dynamics.

Another immediate generalization of the framework is to extend the unitary evolution to generic quantum channels allowing measurements to take place. The recent observation of measurement-induced entanglement transition in random unitary circuits [75, 76, 59] has attracted much research interest.[77, 78, 79, 58, 57, 80] In these models, the quantum circuit is doped with local measurements (which can be either weak measurements or projective measurements performed with some probability), and the final state EE is studied conditioned on the measurement outcome. If each measurements basis is randomly chosen each time, or if the local measurement take place only after the local basis has been sufficiently scrambled by the unitary evolution, the whole quantum channel still falls in the scope of locally scrambled quantum dynamics, which can be described by the EF approach developed in this work. In this case, each measurement, described by the Kraus operator M, is also a local-basis-independent component in the quantum circuit, and has its own EF similar to Eq. (2.5)

$$W_M[\boldsymbol{\sigma}, \boldsymbol{\tau}] = \mathrm{Tr}\left(\mathscr{X}_{\boldsymbol{\sigma}} M^{\otimes 2} \mathscr{X}_{\boldsymbol{\tau}} M^{\dagger\otimes 2}\right), \tag{2.83}$$

from which the EF operator

$$\hat{W}_M = \sum_{\boldsymbol{\sigma}, \boldsymbol{\tau}} |\boldsymbol{\sigma}\rangle W_M[\boldsymbol{\sigma}, \boldsymbol{\tau}] \langle \boldsymbol{\tau}| \tag{2.84}$$

can be constructed. The EF state will evolve under measurement by $|W_{\Psi'}\rangle = \hat{W}_M \hat{W}_{\mathbb{1}}^{-1} |W_\Psi\rangle$, such that the approaches developed in this work seamlessly apply. The EF provides a finer resolution of the entanglement structure of a quantum many-body state beyond the single region scaling of EE, which turns out to be useful in diagnosing the error correction capacity[79] in the volume-law states prepared by the measurement-doped quantum circuits. We will leave this topic to future works[81]. More generally, the EF formulation can be further generalized to locally scrambled tensor networks, which does not even need to have a preferential time direction. As long as each tensor in the tensor network is independently drawn from local-basis-independent ensembles, the entanglement structured of the random tensor network can be described by the EF approach. The freedom to design the EF for each separate tensor in the tensor networks opens up a large space of models to explore in the future.

There are also a few more challenging future directions that are worth further investigation. The first direction is to generalize the 2nd Rényi EF to arbitrary Rényi index. As a consequence, the Ising variable on each site will be promoted to a permutation group element $\sigma_i \in S_n$. Such generalization will also allow us to access other measures of entanglement, such as Rényi negativity[45, 82, 83], as the moment of the partial transposed density matrix ρ^{T_A}[84, 85, 86, 87, 88, 89] can be expressed in terms of the nth Rényi EF,

$$\mathrm{Tr}(\rho^{\mathsf{T}_A})^n = W_\rho[\boldsymbol{g}], \quad g_i = \begin{cases} (n\cdots 21) & i \in A, \\ (12\cdots n) & i \in \bar{A}. \end{cases} \tag{2.85}$$

The nth Rényi generalization of EF states $|W_\Psi\rangle$ and EF operators $\hat{W}_U$ can still be defined, but it will be more difficult to perform explicit calculations given that the number of group elements $n!$ grows quickly with n. Perhaps the most subtle issue is how to take the $n \to 1$ replica limit systematically, which has been identified[42, 57, 58] as an important step to understand the nature of entanglement transitions. The second direction is to include global symmetries and conservation laws[35, 60] into the discussion. This amounts to refining the generic local scramblers to symmetry-preserving local scramblers, which only performs basis transformations within each irreducible representations of the symmetry group. The formulation to describe the interference between the entanglement dynamics and the flow of symmetry representations in the quantum circuits still need to be developed. The third direction is to go beyond the locally scrambled quantum dynamics and to gradually introduce correlations among random gates in the spacetime. Can the current EF formulation serves as a good starting point to construct phenomenological descriptions for weakly correlated random gates? Can we eventually approach the limit of coherent quantum evolution for Hamiltonian or Floquet dynamics? There are many interesting open question awaiting us to explore.

Chapter 2 is, in part, a reprint of material from published work done in collaboration with A. A. Akhtar, Daniel P. Arovas, and Yi-Zhuang You, as it appears in Physical Review B. Wei-Ting Kuo, A. A. Akhtar, Daniel P. Arovas, and Yi-Zhuang You, ”Markovian Entanglement Dynamics under Locally Scrambled Quantum Evolution,” *Phys. Rev. B* **101**, 224202 (2020). The dissertation author was the primary investigator and author of this material.

Chapter 3

Decoherent quench dynamics across quantum phase transitions

3.1 Synopsis

We present a formulation for investigating quench dynamics across quantum phase transitions in the presence of decoherence. We formulate decoherent dynamics induced by continuous quantum non-demolition measurements of the instantaneous Hamiltonian. We generalize the well-studied universal Kibble-Zurek behavior for linear temporal drive across the critical point. We identify a strong decoherence regime wherein the decoherence time is shorter than the standard correlation time, which varies as the inverse gap above the groundstate. In this regime, we find that the freeze-out time $\bar{t} \sim \tau^{2\nu z/(1+2\nu z)}$ for when the system falls out of equilibrium and the associated freeze-out length $\bar{\xi} \sim \tau^{\nu/(1+2\nu z)}$ show power-law scaling with respect to the quench rate $1/\tau$, where the exponents depend on the correlation length exponent ν and the dynamical exponent z associated with the transition. The universal exponents differ from those of standard Kibble-Zurek scaling. We explicitly demonstrate this scaling behavior in the instance of a topological transition in a Chern insulator system. We show that the freeze-out time scale can be probed from the relaxation of the Hall conductivity. Furthermore, on introducing disorder to break translational invariance, we demonstrate how quenching results in regions of imbalanced excitation density characterized by an emergent length scale which also shows universal scaling. We perform numerical simulations to confirm our analytical predictions and corroborate the scaling arguments that we postulate as universal to a host of systems.

3.1.1 Contribution of the author

The author has contributed in developing the main formalism and in writing the paper. He has performed the numerical calculations together with Prof. Yi-Zhuang You.

3.2 Introduction

Nonequilibrium properties associated with quenches across a continuous phase transition are exhibited in a range of physical systems, from quantum magnets at the nanoscale to the cosmos itself. Close to the critical point separating the two phases, the intrinsic relaxation time, equivalently, the correlation time diverges. In this regime, no matter how slow the tuning rate for the quench, the system is driven faster than it can respond, and thus plunges out of equilibrium. Universal properties of the phase transition have powerful implications for the nonequilibrium dynamics associated with the quench. A paradigm example is Kibble-Zurek scaling[4, 5, 6, 7], which states that both the time scale of the out-of-equilibrium dynamics and the length scale of the post-quench nonequilibrium region scale as power laws with the quench rate. The power law exponent depends only on universal properties of the equilibrium phase transition and is independent of microscopic details of the system.

The combined effects of quantum measurement and decoherence on quantum critical quenches largely remains uncharted ground, despite the growing research interest in open quantum systems and measurement-impacted quantum dynamics[75, 78, 79, 90, 76, 59, 57, 80, 58, 81]. Unitary evolution combined with intermittent measurement can generate nontrivial quantum dynamics by repeatedly collapsing the quantum state to the measured basis, following Born's rule. Such processes generally modify the quantum state drastically and create high-energy excitations in the system. However, if the measurement observable commutes with the system Hamiltonian, while the system becomes entangled with its environment, no such high energy excitations are produced, a state of affairs known as a *quantum non-demolition measurement*[91, 92, 93, 94, 95, 96, 97]. In particular, the quantum non-demolition measurement of the system Hamiltonian itself has recently been proposed in Ref. [98, 99] for trapped-ion systems, as an indirect measurement realized by coupling the system with an environment through the energy channel. The process also can be interpreted as the environmental monitoring of the system energy, under which the system will decohere in the energy basis. It was further demonstrated in Ref. [100, 101, 102] that repeatedly measuring local terms of the many-body Hamiltonian during the quantum dynamics can stabilize different quantum phases in the final steady state. One can even drive quantum phase transitions by varying the measurement strength of different Hamiltonian terms. This provides us an opportunity to consider the critical quench dynamics driven by quantum non-demolition measurement of the system energy, and to investigate its effect on universal scaling behaviors.

In this work, we present a formulation for integrating the physics of quantum measurement and decoherence with that of quantum critical quench dynamics. The formulation provides a description of continuous measurement of the system Hamiltonian, while the Hamiltonian itself is dynamically driven across the quantum phase transition. Averaging over energy measurement outcomes leads to decoherence in the energy basis. The decoherence time enters the dynamics as a time scale distinct from that set by the correlation time. As the system is tuned through the critical point, both the decoherence time τ_{dec} and the correlation time ξ_t diverge, such that the quantum dynamics slows down and the system is unable to equilibrate in the face of the parameter tuning. As a result, the system is effectively frozen near the critical point and falls out of equilibrium after the quantum quench. The freeze-out time is set by the choice of time scale between ξ_t and τ_{dec} that remains shorter at the moment. As the two time scales ξ_t and τ_{dec} diverge with different exponents near the critical point, they lead to different scaling behaviors of the freeze-out time (also known as the Kibble-Zurek scaling in the coherent limit). In the strong decoherence regime, we derive the critical quench scaling exponents for both length and time scales, and demonstrate how they differ from the standard Kibble-Zurek predictions.

We apply our formulation to topological transitions in Chern insulators and show how these strong-decoherence scaling laws become manifest. Our choice of system stems from the surge of interest in these materials, the plethora of experiments, the ability to tune through these transitions, and the straightforward theoretical formulation that enables adding the complexity of the decoherent aspects. Given that much of Kibble-Zurek physics has focused on systems having spontaneous symmetry breaking and local order, we focus on an alternate set of observables for probing our predicted novel scaling behavior in the case of topological order. In particular, we propose that the out-of-equilibrium time scale can be obtained from the relaxation of Hall conductivity across the topological transition. We also propose the extraction of the post-quench correlation length from the autocorrelation function of excitation density in the presence of weak disorder.

While this work offers a framework for describing decoherent quantum critical quenches and applies it to a specific example, we believe its scope is very broad[1]. The formulation itself can be applied to vast and diverse systems ranging from symmetry broken phase in cosmology, solid state, and cold atomic gases to topological systems in the latter two settings. Almost invariably, decoherence goes hand in hand with quenching, and in the case of ultracold gases, it can even be engineered. In general, its effects can be murky. But for universal regimes defined by critical points, not only are the effects much more clear-cut, the interplay between the two distinct time scales allows demarcating a testable strong decoherence regime showing entirely new scaling.

In what follows, in Sec. 3.3, we introduce the general formulation of quantum dynamics with energy-basis decoherence, realized by quantum non-demolition measurement of the system Hamiltonian. We derive the master equation that governs the decoherent dynamics. Based on the master equation, having recapitulated standard Kibble-Zurek scaling in quantum quenches, we analyze its behavior in the presence of decoherence.We discuss the regimes of weak versus strong decoherence and associated scaling. In Sec. 3.4, we demonstrate our treatment for quenches in

---

[1] The general behavior of quantum systems undergoing decoherence remains an open question. Our formalism applies to any model so long as the decoherence mechanism can be modeled by continuously measuring the system's energy.

Chern insulators tuned through topological phase transitions. We present the corresponding non-interacting fermionic Hamiltonian and describe the dynamics in terms of associated pseudo-spin degrees of freedom for each momentum sector. We next derive our predicted scaling behavior in the relaxation of Hall conductivity. We adapt numerical techniques to describe quenches and further corroborate our results. We introduce weak disorder to break translational invariance and extract correlation lengths and related scaling behavior via post-quench correlation of emergent regions having high excitation densities. In Sec. 3.5, we summarize our work, consider ramifications, and make connections with possible experiments.

3.3 Universal scaling of decoherent critical quench

We begin with the overarching set-up for describing the decoherent system at hand and its dynamics. We then show how even in the simplest case of a two-level system, one can extract a decoherence time that is intimately tied to the gap between states. Our formulation immediately enables us to study the general scenario of quenching through a quantum critical point. We therefore then proceed to derive the universal argument for a competition between three timescales–the inverse quench rate, the intrinsic coherent timescale of the system (the correlation time), and the decoherence time. Based on the competition, we are able to identify strong and weak decoherence regimes and the different associated scaling behavior of the critical quench.

3.3.1 Decoherent Quantum Dynamics

The decoherence of a quantum system in its energy eigenbasis can be effectively modeled by an environment that monitors the energy of the quantum system through continuous measurements[103, 104]. Under this protocol, the dynamics of the quantum system is non-unitary and can be formulated as a *quantum channel*[105]. The quantum channel formulation provides a unified description of the effect of both unitary evolution and quantum measurement on the density matrix ρ of an open quantum system,

$$\rho(t+\delta t) = \sum_j K_j(t)\,\rho(t)\,K_j^\dagger(t) \quad , \tag{3.1}$$

specified by a set of Kraus operators[106] $K_i(t)$ satisfying $\sum_j K_j^\dagger(t)K_j(t) = 1$. Unitary evolution corresponds to the presence of a single unitary Kraus operator $K(t) = U(t) = e^{-\mathrm{i}H(t)\,\delta t}$ (setting $\hbar = 1$); in this case, one has the familiar behavior

$$\rho(t+\delta t) = \rho(t) - \mathrm{i}\,\delta t\,\left[H(t), \rho(t)\right] + \mathscr{O}(\delta t^2), \tag{3.2}$$

where $H(t)$ is the Hamiltonian of the quantum system that generates the coherent time-evolution.

The environmental monitoring of the energy of a quantum system can be described by a set of measurement operators $K_j(t)$, where the index j labels the possible measurement outcomes. We consider an indirect (or ancilla) weak measurement[107] scheme, in which the system couples to some ancilla qubits in the environment via the interaction term $H_{\text{int}}(t) = H(t) \otimes A$. Here, $H(t)$ is the Hamiltonian of the quantum system and A is some Hermitian operator acting on the ancilla qubits. Suppose the ancilla qubits start in a random initial state $|\phi\rangle$ and evolve jointly with the quantum system under $H_{\text{int}}(t)$ for a short period of time, after which they collapse to the measurement basis $|j\rangle$ via a projective measurement. The effect on the quantum system is described by the following Kraus operator

$$K_j(t) = \langle j|\phi\rangle\,\mathbb{I} - \mathrm{i}\,\varepsilon H(t)\left\langle j\,\middle|A\,\middle|\,\phi\right\rangle - \tfrac{1}{2}\varepsilon^2 H(t)^2\left\langle j\,\middle|A^2\,\middle|\,\phi\right\rangle + \mathscr{O}(\varepsilon^3) \tag{3.3}$$

where ε is proportional to the coupling time and can be viewed as a parameter controlling the measurement strength. Here $\mathbb{I}$ is the identity operator acting on the Hilbert space of the system. This procedure weakly measures the energy of the quantum system because the observable being measured in a quantum measurement is determined by the particular operator that couples the system to the environment[108, 109], which in this case is the system Hamiltonian $H(t)$ itself. Such a measurement protocol will gradually decohere the system to disperse among different energy levels. Applying the Kraus operator to the density matrix, we obtain

$$\begin{aligned}\sum_j K_j(t)\,\rho(t)\,K_j^\dagger(t) &= \rho(t) - \mathrm{i}\,\varepsilon\left[H(t),\rho(t)\right]\left\langle\,\phi\,\middle|\,A\,\middle|\,\phi\,\right\rangle \\ &\quad -\tfrac{1}{2}\varepsilon^2\left[H(t),\left[H(t),\rho(t)\right]\right]\left\langle\,\phi\,\middle|\,A^2\,\middle|\,\phi\,\right\rangle + \mathscr{O}(\varepsilon^3) \quad . \qquad (3.4)\end{aligned}$$

We assume that the ancilla state $|\phi\rangle$ and the ancilla operator A satisfy $\left\langle\,\phi\,\middle|\,A\,\middle|\,\phi\,\right\rangle = 0$, such that the measurement process will not bias the energy of the system. Typically this is true if $|\phi\rangle$ and A are random, as we have no prior knowledge of how the environment will monitor the energy. We also ignore the memory effect of the environment, and assume that the dynamics is Markovian. With this assumption, the density matrix evolves under the environmental measurement as

$$\rho(t+\delta t) = \rho(t) - \gamma\delta t\left[H(t),\left[H(t),\rho(t)\right]\right] + \mathscr{O}(\delta t^2)\,, \qquad (3.5)$$

where a new parameter $\gamma = \left\langle\,\phi\,\middle|\,A^2\,\middle|\,\phi\,\right\rangle\varepsilon^2/(2\,\delta t)$ is introduced to represent the quantum non-demolition measurement strength (or the decoherence rate). To approach the limit of continuous measurement, we should take the $\delta t \to 0$ limit keeping the ratio $\varepsilon^2/\delta t$ held fixed so as to respect the quadratic time scaling[110, 111, 112] required by the quantum Zeno effect.

Combining Eq. (3.2) with Eq. (3.5), and taking the continuum limit $\delta t \to 0$, we arrive at the master equation for decoherent quantum dynamics

$$\frac{\partial\rho(t)}{\partial t} = -\mathrm{i}\left[H(t),\rho(t)\right] - \gamma\left[H(t),\left[H(t),\rho(t)\right]\right] \quad . \qquad (3.6)$$

This is the Lindblad equation (in double-commutator form)[113, 114, 115] for the Lindblad operator being the Hamiltonian itself. Note that we derive this result from the time evolution of density matrix (Eq. (3.2)) with continuum limit. It describes how an open quantum system evolves under a time-dependent Hamiltonian as it continues to decohere among the instantaneous energy eigenstates.

If H is time-independent, then it is easy to see that the off-diagonal elements of $\rho(t)$ expressed in the eigenbasis of H all collapse to zero provided they are between states of different energy, *i.e.* $\rho_{mn}(t) \to 0$ if $E_m \neq E_n$. For time-dependent $H(t)$, however, as we shall see, the dynamics is nontrivial.

3.3.2 Decoherence time and excitation energy

To gain more intuition regarding the decoherent quantum dynamics described by Eq. (3.6), we consider a quantum system close to its ground state. As a toy model, we focus on the low-energy subspace spanned by the ground state (energy E_0) and the first-excited state (energy E_1), in which H and ρ can be represented as

$$H = \begin{bmatrix} E_0 & 0 \\ 0 & E_1 \end{bmatrix} \quad , \quad \rho = \begin{bmatrix} \rho_{00} & \rho_{01} \\ \rho_{10} & \rho_{11} \end{bmatrix} \quad . \tag{3.7}$$

Within this two-level subspace, Eq. (3.6) implies

$$\frac{\partial \rho_{01}}{\partial t} = \mathrm{i}\,(E_1 - E_0)\rho_{01} - \gamma(E_1 - E_0)^2 \rho_{01}, \tag{3.8}$$

which indicates that the off-diagonal density matrix element (*i.e.* the quantum coherence between the ground state and the excited state) decays exponentially in time as $|\rho_{01}| \propto \exp(-t/\tau_{\mathrm{dec}})$. Here, the decoherence time is given by

$$\tau_{\mathrm{dec}} = \frac{1}{\gamma \Delta^2}, \tag{3.9}$$

where $\Delta = E_1 - E_0$ denotes the excitation energy. This demonstrates that Eq. (3.6) indeed describes the energy level decoherence in which the decoherence time τ_{dec} is set by the energy Δ (or more generally, the level spacing).

3.3.3 Kibble-Zurek scaling under decoherent quench

With the general formulation of the decoherent quantum dynamics now in place, captured by the master equation in Eq. (3.6), we can now investigate quenches in the presence of decoherence. Specifically, we analyze the effect of introducing decoherence to the universal behavior exhibited by quantum systems dynamically tuned between two phases through a continuous quantum phase transition. Quantum quenches, in general, form a fertile and currently active field of study (see e.g., Ref. [116]), encompassing condensed matter physics, atomic, molecular and optical physics (AMO), cosmology, and quantum information. Quenches near quantum and thermal critical points exhibit Kibble-Zurek behavior[4, 5, 6, 7], which reflects the universal non-equilibrium power-law scaling of several quantities, such as quench-induced density of defect. Note that here we focus on quantum quenches, as opposed to thermal. The source of the non-equilibrium behavior is that the intrinsic relaxational timescale of the system diverges as a universal power-law close to the critical point, and thus, no matter how slow the quench rate, the system cannot relax fast enough in a certain window. The size $\bar{\xi}$ of the local equilibrium domain after the quench scales with the quench rate $1/\tau$ as

$$\bar{\xi} \sim \tau^{\nu/(1+\nu z)} \quad , \tag{3.10}$$

where ν and z are the correlation length exponent and dynamic critical exponent associated with the quantum critical point. We will show that the same scaling holds under decoherence as long as the decoherence rate γ scales together with the quench rate as $\gamma \sim \tau^{\nu z/(1+\nu z)}$. However, in the strong decoherence limit ($\gamma \to \infty$), we find a new combined scaling

$$\bar{\xi} \sim (\gamma\tau)^{\nu/(1+2\nu z)} \quad , \tag{3.11}$$

which is unique to the decoherent dynamics.

These trends in scaling behavior can be derived from an analysis of the dynamic equation Eq. (3.6). Here, we generalize the standard approach for Kibble-Zurek physics in absence of dissipation to include and pinpoint its effects. We assume the quantum critical point can be describe by a critical Hamiltonian H_{critical}. Quenching through the critical point corresponds to tuning the relevant perturbation H_{pert} (which drives the phase transition) through zero, which can be formally described by

$$H(t) = H_{\text{critical}} + \delta(t) H_{\text{pert}} \quad , \tag{3.12}$$

where $\delta(t) = \alpha(t) - \alpha_{\text{c}}$ measures the deviation of the driving parameter α away from its critical point α_{c}. In the vicinity of the critical point, we focus on the most general quench case where the deviation is tuned linearly with time $\delta(t) = t/\tau$, which introduces the quench rate $1/\tau$ (or equivalently the quench time scale τ). However, the linear tuning of the driving parameter does not tune the excitation energy linearly. Near the quantum critical point, low-energy collective properties of the system, such as the correlation length ξ or the excitation energy Δ, scale with the deviation δ according to power laws set by universal relations

$$\xi \sim \delta^{-\nu} \sim (t/\tau)^{-\nu} \quad , \quad \Delta \sim \xi^{-z} \sim (t/\tau)^{\nu z} \quad . \tag{3.13}$$

The many-body excitation energy Δ will be the only relevant energy scale that enters Eq. (3.6) in the replacement of $H(t)$ near the critical point.

Following the form of Eq. (3.8), we ignore all the level-specific details, which are secondary to universal behavior, and put forth a heuristic dynamic equation for the purpose of scaling analysis, *viz.*

$$\begin{aligned}\frac{\partial\rho}{\partial t} &\sim \left(\mathrm{i}\Delta-\gamma\Delta^2\right)\rho \\ &\sim \left\{\mathrm{i}\left(\frac{t}{\tau}\right)^{\nu z}-\gamma\left(\frac{t}{\tau}\right)^{2\nu z}\right\}\rho \quad .\end{aligned} \tag{3.14}$$

We can eliminate the τ-dependence in Eq. (3.14) by rescaling t and γ jointly as follows:

$$t \to \tau^{\nu z/(1+\nu z)}t' \quad , \quad \gamma \to \tau^{\nu z/(1+\nu z)}\gamma' \quad , \tag{3.15}$$

implying that the quantum quench dynamics is universal if the time t and the decoherence rate γ scale accordingly. In the large γ regime, Eq. (3.14) is dominated by the decoherence dynamics (*i.e.* the γ-term only), *viz.*

$$\partial_t\rho \sim -\gamma\Delta^2\rho \sim -\gamma\left(\frac{t}{\tau}\right)^{2\nu z}\rho \quad . \tag{3.16}$$

It is then possible to simultaneously eliminate both the γ- and the τ-dependences in Eq. (3.16) by the following rescaling of time:

$$t \to (\gamma^{-1}\tau^{2\nu z})^{1/(1+2\nu z)}t' \quad , \tag{3.17}$$

which gives a different, but consistent, scaling of time in the strong decoherence limit as compared to Eq. (3.15), which holds for all decoherence rates.

Underlying the different scaling behaviors is the competition between two distinct time scales: the correlation time ξ_t and the decoherence time τ_{dec} (defined in Eq. (3.9)),

$$\xi_t \sim \frac{1}{\Delta} \sim \left(\frac{t}{\tau}\right)^{-\nu z}, \quad \tau_{\text{dec}} \sim \frac{1}{\gamma\Delta^2} \sim \frac{1}{\gamma}\left(\frac{t}{\tau}\right)^{-2\nu z}. \tag{3.18}$$

As we quench through a quantum critical point, the many-body excitation energy Δ closes and reopens. As the critical point is approached, namely $\Delta \to 0$, both the correlation time ξ_t and the

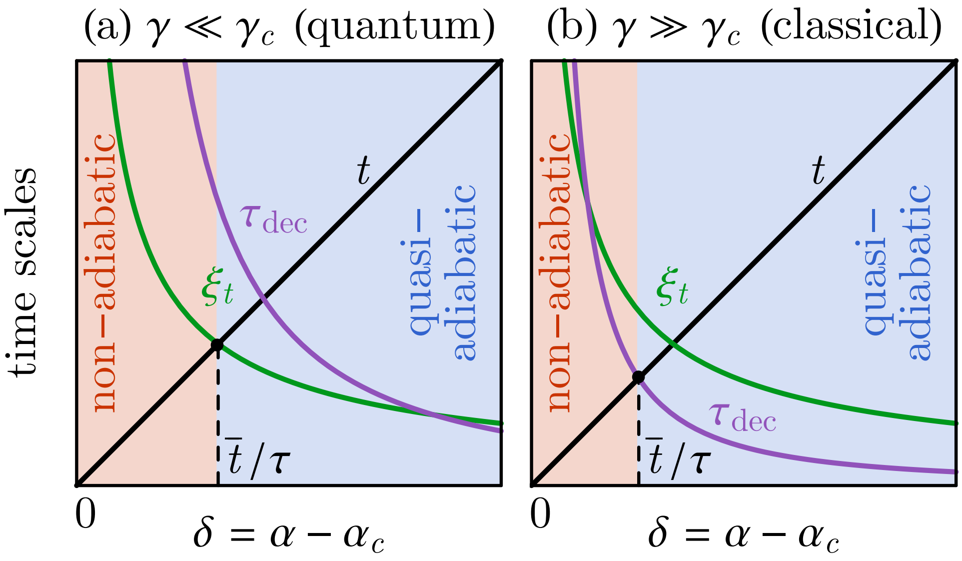

Figure 3.1. The divergent correlation time ξ_t and decoherence time τ_{dec} near the critical point under (a) weak decoherence (quantum regime) and (b) strong decoherence (classical regime). The first intersection point marks the freeze-out time $\bar{t}$ when the system loses/restores adiabaticity. Thus, during the quench process, the freeze-out time in (a) is determined by ξ_t and in (b) by τ_{dec} .

decoherence time τ_{dec} diverge, as shown in Fig. 3.1. The system effectively freezes due to the critical slowing down and falls out of equilibrium. The freeze-out time $\bar{t}$ is set by the smaller time scale $\mathsf{min}(\xi_t, \tau_{\text{dec}})$. These time scales correspond to two different mechanisms to maintain adiabaticity: beyond the correlation time ξ_t, the system can respond to the parameter tuning by unitary evolution, while beyond the decoherence time τ_{dec}, the system can follow the energy level by the quantum Zeno effect (the effect that frequent measurements can slow down the quantum evolution).

The competition between ξ_t and τ_{dec} is dependent upon the decoherence rate γ, as can be seen from Eq. (3.18). When the decoherence rate γ is small, the system is in the coherent quantum regime, where ξ_t is the shorter time scale, and the freeze-out time $\bar{t}$ is set by $\bar{t} \simeq \xi_t(\bar{t}) \sim (\bar{t}/\tau)^{-\nu z}$. The solution then conforms to standard Kibble-Zurek behavior and reads

$$\bar{t} \sim \tau^{\nu z/(1+\nu z)} \quad , \quad \bar{\xi} \sim (\bar{t}/\tau)^{-\nu} \sim \tau^{\nu/(1+\nu z)} \quad , \tag{3.19}$$

which is consistent with Eq. (3.15) and Eq. (3.10). When the decoherence rate γ is large, the system is in the decoherent "classical" regime, where τ_{dec} is the shorter time scale, and the freeze-out time $\bar{t}$ is set by $\bar{t} \simeq \tau_{\text{dec}}(\bar{t}) \sim \gamma^{-1}(\bar{t}/\tau)^{-2\nu z}$. The term "classical" here means that the density matrix is diagonal in the energy basis. The off-diagonal terms vanish in the strong decoherence regime, and information about the relative phase is washed out. Thus, we called this strong decoherence limit as "classical" limit. The solution then reads

$$\bar{t} \sim (\gamma^{-1}\tau^{2\nu z})^{1/(1+2\nu z)} \quad , \quad \bar{\xi} \sim (\bar{t}/\tau)^{-\nu} \sim (\gamma\tau)^{\nu/(1+2\nu z)}, \tag{3.20}$$

which is consistent with Eq. (3.17) and Eq. (3.11). The crossover between the two regimes occurs at a decoherence rate $\gamma_c = \tau^{\nu z/(1+\nu z)}$ when all the time scales meet $t \simeq \xi_t \simeq \tau_{\text{dec}}$, as indicated by Eq. (3.15).

Regarding the new scaling found in the strong decoherence regime (Eq. (3.20)), we wish to stress the following: The exponent in the strong decoherence regime can be obtained by replacing the dynamical exponent z in conventional Kibble-Zurek scaling (Eq. (3.19)) with $2z$. This simple replacement results from the peculiar excitation energy dependence in decoherence time ($\tau_{\text{dec}} \sim \Delta^{-2}$ in Eq. (3.9)). Note that the time scale ξ_t in standard Kibble-Zurek scaling is inversely proportional to the excitation energy $\xi_t \sim \Delta^{-1}$. This crucial difference leads to a doubling of the conventional KZ dynamical exponent in strong decoherence regime.

This new scaling is expected to emerge due to the introduction of decoherence rate γ. Similar change of scaling by introducing new parameter can be achieved by coupling the system with thermal bath with tuning parameter temperature[117]. The main difference between our decoherent formulation and regular thermal coupling is the interaction term, in that we choose an interaction which commutes with the system Hamiltonian. In the strong decoherence regime, the final density matrix becomes diagonal in the energy basis, but does not belong to any thermal ensemble. This leads to the new scaling form in this regime of strong decoherence.

In conclusion, our analysis shows that, depending on the ratio $\gamma/\gamma_c = \gamma/\tau^{-\nu z/(1+\nu z)}$, the quench dynamics can cross over from the quantum limit ($\gamma/\gamma_c \ll 1$) to the ”classical” limit ($\gamma/\gamma_c \gg 1$). A combined scaling behavior Eq. (3.20) emerges in the strong decoherence ”classical” regime, which is different from (but consistent with) the Kibble-Zurek behavior of Eq. (3.19).

3.4 Decoherent quench through topological transitions

In order to demonstrate our arguments and explore new terrain in decoherent dynamics, we now apply the general framework developed above to investigate quantum quenches in topological insulators. We focus mainly on quenches across the topological transition separating a Chern insulator from a trivial insulator. Most of our results can be easily generalized to topological insulators in other dimensions and they demonstrate the principles behind a diverse range of systems, both topological and non-topological.

In what follows, we first introduce the model Hamiltonian parametrized by a pseudo-magnetic field in momentum space. We then formulate the related density matrix in terms of the pseudo-spin vector. By applying the master equation for decoherent quantum dynamics developed in the previous section, we obtain the effective dynamical equation for the pseudo-spin, based on which we analyze the universal scaling behavior for the topological transition.

3.4.1 Model Hamiltonian and band topology

Consider a two-band Hamiltonian of spinless fermions in (2+1) dimensions having a time-dependent band structure

$$H(t) = \frac{1}{2}\sum_{\boldsymbol{k}} c^{\dagger}_{\boldsymbol{k}} \boldsymbol{h}_{\boldsymbol{k}}(t) \cdot \boldsymbol{\sigma}\, c_{\boldsymbol{k}} \quad , \tag{3.21}$$

where $c_{\boldsymbol{k}}$ is the fermion annihilation operator in momentum space, $\boldsymbol{\sigma} = (\sigma_x, \sigma_y, \sigma_z)$ represents the pseudo-spin operators as Pauli matrices, and $\boldsymbol{h}_{\boldsymbol{k}}(t)$ is the time-dependent pseudo-magnetic field defined for each momentum $\boldsymbol{k} = (k_x, k_y)$. As opposed to actual spins in magnetic fields, the pseudo-spin describes *orbital* degrees of freedom of spinless fermions. The (instantaneous) band dispersions are given by $\pm|\boldsymbol{h}_{\boldsymbol{k}}|$. The two bands are separated by a gap so long as $|\boldsymbol{h}_{\boldsymbol{k}}| \neq 0$ throughout the Brillouin zone. We assume that the number of fermions is such that they can fully fill a single band, and that the fermion number does not change with the ensuing quantum dynamics.

Depending on the winding number of $\hat{\boldsymbol{h}}_{\boldsymbol{k}} \equiv \boldsymbol{h}_{\boldsymbol{k}} / |\boldsymbol{h}_{\boldsymbol{k}}|$ in momentum space

$$w = \frac{1}{4\pi} \int \mathrm{d}^2 k \, \hat{\boldsymbol{h}}_{\boldsymbol{k}} \cdot \frac{\partial \hat{\boldsymbol{h}}_{\boldsymbol{k}}}{\partial k_x} \times \frac{\partial \hat{\boldsymbol{h}}_{\boldsymbol{k}}}{\partial k_y} \tag{3.22}$$

the band structure can be classified as trivial (if $w = 0$) or topological (if $w \neq 0$). Our quench consists of tuning the band structure between the trivial and the topological phases. Such quenches have been studied extensively in the literature[118, 119, 120, 121, 122, 123, 124, 125, 126, 127, 128, 129, 130, 131, 132, 133, 134, 135], but the effect of decoherence is still largely not understood. Our goal is thus to examine the interplay between critical quench dynamics and quantum decoherence in topological insulators.

To analyze the critical behavior, we invoke the linearized band structure near the Dirac point,

$$\boldsymbol{h}_{\boldsymbol{k}}(t) = \left(k_x, k_y, t/\tau\right) \quad , \tag{3.23}$$

which describes the low-energy Dirac Hamiltonian with linearly tuned mass term. We assume that the mass term $m = t/\tau$ is tuned linearly across the phase transition.

3.4.2 Quench protocol and density matrix

For the quench protocol, we start with the ground state of an initial Hamiltonian $H(t_0)$ ($t_0 < 0$), where the bottom band is filled and the upper band is empty. We then tune the band structure through a topological transition, where the band gap closes and reopens. We define our time origin such that the critical point is always reached at $t = 0$. The time evolution of the system is governed by the dynamical equation Eq. (3.6). True to a free fermion system, the quantum dynamics takes place at each momentum point independently. Since the initial state is a product state over momentum states, the density matrix of the system continues to take the product form throughout the evolution

$$\rho(t) = \prod_{\boldsymbol{k}} c^{\dagger}_{\boldsymbol{k}} |0\rangle \, \rho_{\boldsymbol{k}}(t) \, \langle 0| \, c_{\boldsymbol{k}} \quad , \tag{3.24}$$

where $\rho_{\boldsymbol{k}}(t)$ is the single-particle density matrix at momentum $\boldsymbol{k}$,

$$\rho_{\boldsymbol{k}}(t) = \frac{1}{2}\left(1 + \boldsymbol{n}_{\boldsymbol{k}}(t) \cdot \boldsymbol{\sigma}\right) \quad . \tag{3.25}$$

The pseudo-spin vector $\boldsymbol{n}_{\boldsymbol{k}}(t) = \mathrm{Tr}\, \rho(t)\, c^{\dagger}_{\boldsymbol{k}} \boldsymbol{\sigma}\, c_{\boldsymbol{k}}$ is introduced in momentum space to parameterize the density matrix. The ”purity” of the density matrix is given by $\mathrm{Tr}(\rho^2) = \prod_{\boldsymbol{k}} \frac{1}{2}(1 + |\boldsymbol{n}_{\boldsymbol{k}}|^2)$, such that the system is pure if and only if $|\boldsymbol{n}_{\boldsymbol{k}}|^2 = 1$ for all $\boldsymbol{k}$, *i.e.* when the pseudo-spin vector lies on the unit sphere. Due to the non-unitary decoherent dynamics, the density matrix in general becomes mixed under the time-evolution such that the pseudo-spin vectors shrink toward the origin, *i.e.* $\boldsymbol{n}_{\boldsymbol{k}} \to 0$. In this limit, the density matrix for each $\boldsymbol{k}$ is proportional to the identity, corresponding to ‘infinite temperature’.

3.4.3 Dynamics of pseudo-spin vectors

To describe the pseudo-spin dynamics, we substitute the Hamiltonian $H(t)$ from Eq. (3.21) and the density matrix $\rho(t)$ from Eq. (3.24) into the master equation Eq. (3.6). Note that each momentum sector is decoupled in the free fermion model. In terms of the pseudo-magnetic field $\boldsymbol{h}_{\boldsymbol{k}}(t)$ and the pseudo-spin $\boldsymbol{n}_{\boldsymbol{k}}(t)$, the dynamic equation reads

$$\frac{\partial \boldsymbol{n}_{\boldsymbol{k}}}{\partial t} = \boldsymbol{h}_{\boldsymbol{k}} \times \boldsymbol{n}_{\boldsymbol{k}} + \gamma \boldsymbol{h}_{\boldsymbol{k}} \times (\boldsymbol{h}_{\boldsymbol{k}} \times \boldsymbol{n}_{\boldsymbol{k}}) \quad . \tag{3.26}$$

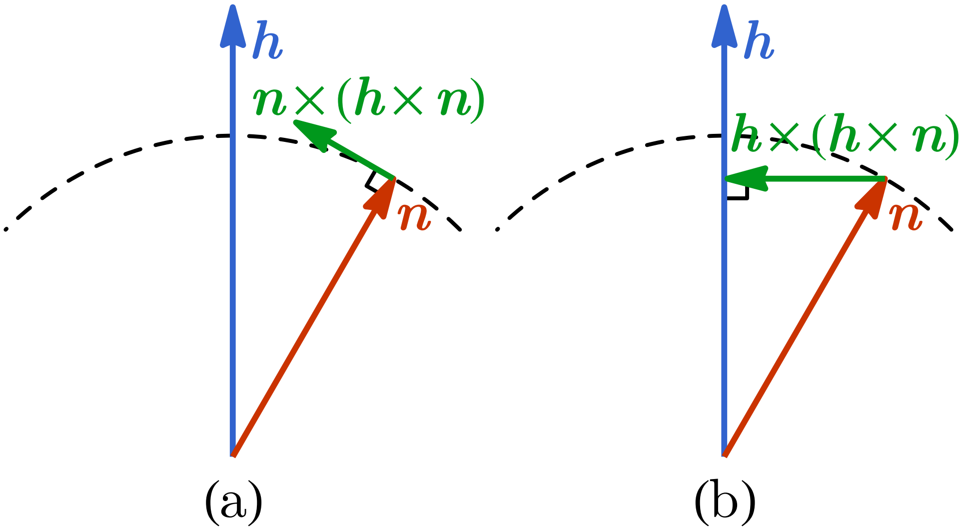

Figure 3.2. Comparison of the effects of (a) the damping term λ in the LLG equation and (b) the decoherence term γ in Eq. (3.26).The contribution to the rate of change of the pseudo-vector is denoted by the green arrow. The dynamics in (a) preserves the norm of the pseudo-vector but it does not in (b).

Note that Eq. (3.26) is different from the Landau-Lifshitz-Gilbert (LLG) equation,

$$\frac{\partial \boldsymbol{n}}{\partial t} = \boldsymbol{h} \times \boldsymbol{n} + \lambda\, \boldsymbol{n} \times (\boldsymbol{h} \times \boldsymbol{n}) \quad , \tag{3.27}$$

used to describe the damping of spin precession in a magnetic field. The LLG equation is nonlinear in $\boldsymbol{n}$ and preserves the norm of $\boldsymbol{n}$. In contrast, Eq. (3.26) is linear in $\boldsymbol{n}_k$ with the norm of $\boldsymbol{n}_k$ generally decreasing under evolution, which reflects the non-unitary nature of the decoherent dynamics. Their differences are clearly demonstrated in Fig. 3.2. Under the decoherent dynamics, the pseudo-spin $\boldsymbol{n}_k$ tends to be projected onto the direction of the pseudo-magnetic field $\boldsymbol{h}_k$, which precisely describes the decoherence of off-diagonal density matrix elements in the diagonal basis set by the Hamiltonian $\boldsymbol{h}_k \cdot \boldsymbol{\sigma}$. Similar decoherence term was also studied in Ref. [136].

As the system equilibrates to the ground state, the pseudo-spin $\boldsymbol{n}_k$ anti-aligns with the pseudo-magnetic field $\boldsymbol{h}_{\boldsymbol{k}}$, *i.e.* $\boldsymbol{n}_{\boldsymbol{k}} \to -\hat{\boldsymbol{h}}_{\boldsymbol{k}}$, so as to minimize the energy

$$E = \operatorname{Tr}(H\rho) = \frac{1}{2}\sum_{\boldsymbol{k}} \boldsymbol{h}_{\boldsymbol{k}} \cdot \boldsymbol{n}_{\boldsymbol{k}} \quad . \tag{3.28}$$

When the pseudo-magnetic field $\boldsymbol{h}_{\boldsymbol{k}}$ flips between topological and trivial configurations, there are two mechanisms to maintain the pseudo-spin in alignment with the field. In the weak deoherence regime ($\gamma \ll \gamma_{\mathrm{c}}$), as the pseudo-spin precesses about the pseudo-magnetic field it is also driven by the damping towards its new equilibrium position, as shown in Fig. 3.3(a). In the strong decoherence regime ($\gamma \gg \gamma_{\mathrm{c}}$), the pseudo-spin is driven by the quantum Zeno effect to follow the field, as shown in Fig. 3.3(b), since it is constantly being measured by the environment along the field direction. The crossover decoherence rate γ_{c} scales as $\gamma_{\mathrm{c}} \sim \tau^{1/2}$ with the quench rate $1/\tau$.

In the vicinity of the Dirac point at $\boldsymbol{k} = 0$, where the band gap closes, the pseudo-magnetic field vanishes as the system is driven through criticality. In this case, the pseudo-magnetic field ceases to provide the alignment impetus to the pseudo-spin. Therefore, *both* alignment mechanisms fail in this region, and the system falls out of equilibrium as the pseudo-spin loses track of the pseudo-magnetic field. The above argument can be confirmed by the numerical

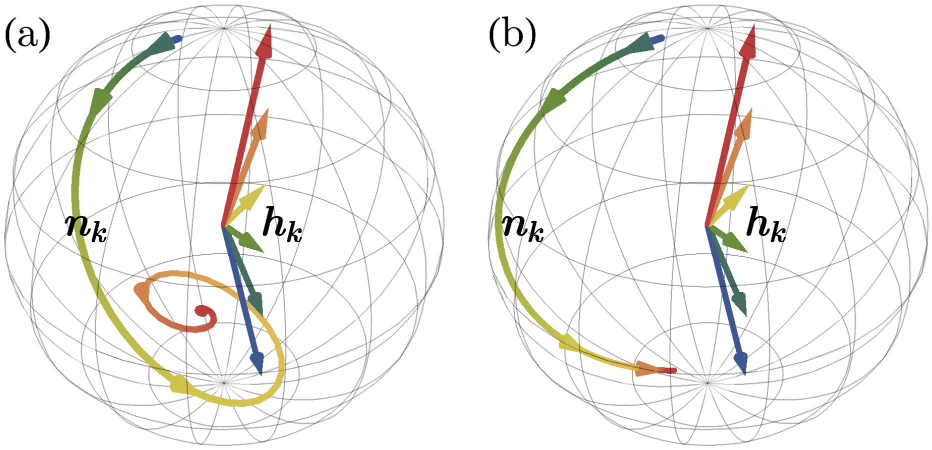

Figure 3.3. Pseudo-spin dynamics under (a) weak decoherence $\gamma = 0.1\tau^{1/2}$ and (b) strong decoherence $\gamma = 10\tau^{1/2}$. The rainbow colors (from blue to red) trace the time evolution.

simulation of the pseudo-spin dynamics Eq. (3.26) using the linearized model Eq. (3.23),

$$
\begin{aligned}
\frac{\partial}{\partial t}\begin{bmatrix} n_1 \\ n_2 \\ n_3 \end{bmatrix} &= \begin{bmatrix} 0 & -t/\tau & k_y \\ t/\tau & 0 & -k_x \\ -k_y & k_x & 0 \end{bmatrix}\begin{bmatrix} n_1 \\ n_2 \\ n_3 \end{bmatrix} \\
&-\gamma\begin{bmatrix} k_y^2+(t/\tau)^2 & -k_xk_y & -k_xt/\tau \\ -k_xk_y & k_x^2+(t/\tau)^2 & -k_yt/\tau \\ -k_xt/\tau & -k_yt/\tau & k_x^2+k_y^2 \end{bmatrix}\begin{bmatrix} n_1 \\ n_2 \\ n_3 \end{bmatrix} .
\end{aligned}
\tag{3.29}
$$

A typical result (at $\gamma = \gamma_c \sim \tau^{1/2}$) is shown in Fig. 3.4. As $h^z_{\boldsymbol{k}}$ flips across the critical point, $n^z_{\boldsymbol{k}}$ is expected to follow the sign change if the dynamics were the adiabatic. However, due to the gap closing at the Dirac point $\boldsymbol{k} = 0$, the system can not maintain adiabaticity in the vicinity of the Dirac point, no matter how slow the driving parameter is tuned. As a result, a portion of the pseudo-spins fails to flip after the quench, which leads to an emergent nonequilibrium region in the momentum space within the momentum range $\bar{k}$ in Fig. 3.4(e).

3.4.4 Universal scaling for topological transition

To understand how the nonequilibrium momentum range $\bar{k}$ scales with the quench rate $1/\tau$, we perform a scaling analysis of the dynamic equation Eq. (3.29). It is straightforward to check that rescaling variables $t \to \tau^{1/2}t'$, $\boldsymbol{k} \to \tau^{-1/2}\boldsymbol{k}'$, and $\gamma \to \tau^{1/2}\gamma'$ eliminates the τ-dependence in the equation entirely. This implies that the quench dynamics is universal if the time t, the momentum $\boldsymbol{k}$ and the decoherence rate γ scale with the quench time τ accordingly. Therefore, we conclude that the freeze-out time $\bar{t}$, the nonequilibrium momentum range $\bar{k}$ and the local equilibrium domain size $\bar{\xi}$ scale as

$$
\bar{t} \sim \tau^{1/2} \quad , \quad \bar{k} \sim \tau^{-1/2} \quad , \quad \bar{\xi} \sim \tau^{1/2} \quad , \tag{3.30}
$$

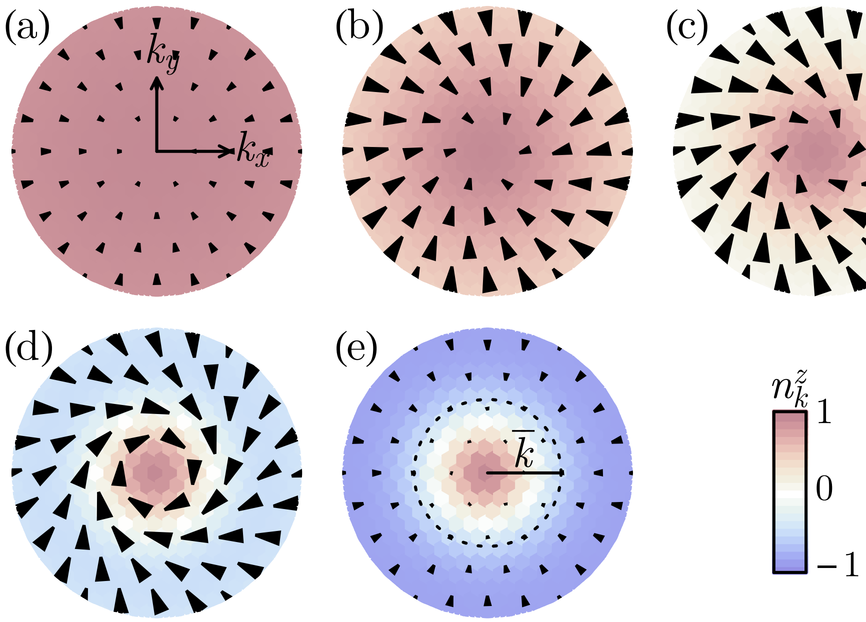

Figure 3.4. Evolution of pseudo-spin vectors in momentum space at (a) $t = -5\tau^{1/2}$, (b) $t = -\tau^{1/2}$, (c) $t = 0$, (d) $t = \tau^{1/2}$, (e) $t = 5\tau^{1/2}$. The black arrow indicates the in-plane component $(n_{\boldsymbol{k}}^x, n_{\boldsymbol{k}}^y)$ and the background color indicates the $n_{\boldsymbol{k}}^z$ component.

which is consistent with the Kibble-Zurek scaling given in Eq. (3.19), with $\nu = 1$ and $z = 1$ for the topological transition of Dirac fermions. The scales $\bar{k}$ and $\bar{\xi}$ are dual to each other: the system falls out of equilibrium within $\bar{k}$ in momentum space, which translates to the non-adiabaticity beyond $\bar{\xi}$ in the real space.

To quantify the nonequilibrium region in the momentum space, we define the excitation density

$$p_{\text{exc}}(\boldsymbol{k}) = \lim_{t\to\infty} \tfrac{1}{2}\left(1 + \hat{\boldsymbol{h}}_{\boldsymbol{k}}(t) \cdot \boldsymbol{n}_{\boldsymbol{k}}(t)\right) \quad , \tag{3.31}$$

and the thermal entropy density

$$S_{\text{th}}(\boldsymbol{k}) = -\lim_{t\to\infty} \sum_{s=\pm} \frac{1 + s\,|\boldsymbol{n}_{\boldsymbol{k}}(t)|}{2} \log_2\left(\frac{1 + s\,|\boldsymbol{n}_{\boldsymbol{k}}(t)|}{2}\right) \quad , \tag{3.32}$$

in the late time limit. The late time limit is defined to be long enough for the energy-basis decoherence to have effect but short enough for other possible relaxation mechanism to influence the system. The excitation density $p_{\rm ext}(\boldsymbol{k})$ measures the probability that the fermion at momentum $\boldsymbol{k}$ is found to be excited in the upper band after quench. The thermal entropy density $S_{\rm th}(\boldsymbol{k})$ reflects the distribution of thermal entropy in momentum space after the quench. Our results are shown in Fig. 3.5 for different decoherence rates γ. Separated by a crossover decoherence rate $\gamma_{\rm c} \sim \tau^{1/2}$, the weak decoherence ($\gamma \ll \gamma_{\rm c}$) and the strong decoherence ($\gamma \gg \gamma_{\rm c}$) regimes clearly exhibit different behaviors. In the coherent limit ($\gamma \to 0$), the nonequilibrium momentum range $\bar{k} \sim \tau^{-1/2}$ is simply set by the quench rate $1/\tau$. As decoherence sets in, $\bar{k}$ will continue to shrink with γ, because decoherence helps drive the system back to equilibrium. In the strong decoherence regime, a new set of scaling emerges,

$$\bar{t} \sim \gamma^{-1/3}\tau^{2/3} \quad , \quad \bar{k} \sim (\gamma\tau)^{-1/3} \quad , \quad \bar{\xi} \sim (\gamma\tau)^{1/3} \quad , \tag{3.33}$$

which describes how the momentum range $\bar{k}$ shrinks with the decoherence rate γ (see the dashed

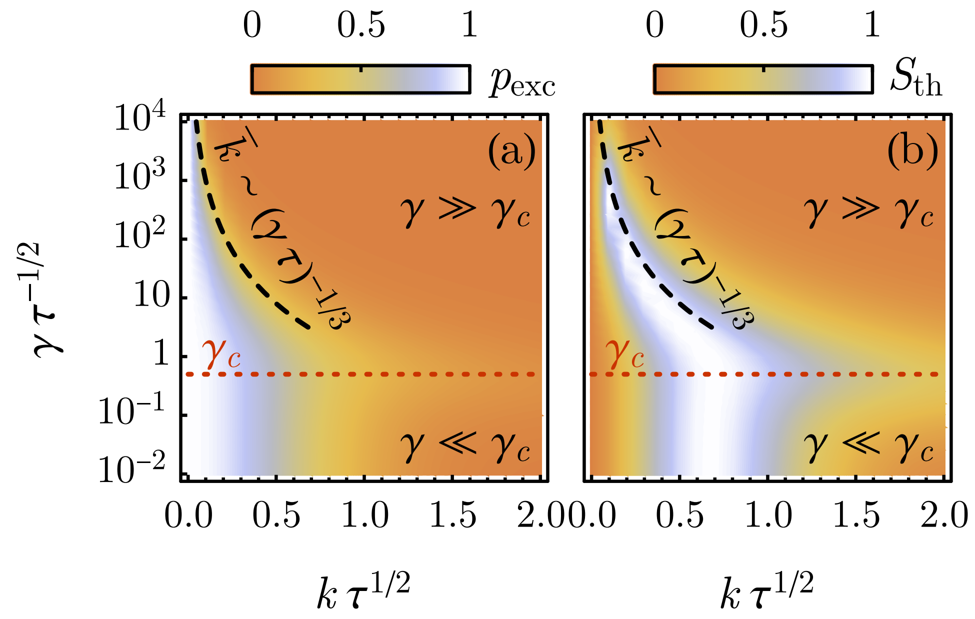

Figure 3.5. (a) Excitation density and (b) thermal entropy distribution in momentum space for different decoherence rates γ. The line γ_c demarcates the weak versus strong decoherence regimes in both plots. The dashed black lines indicate emergent new scaling in the strong decoherence limit.

curves in Fig. 3.5). These scaling behaviors are consistent with the general result in Eq. (3.20) with $\nu = 1$ and $z = 1$. They may also be obtained by a scaling analysis of the dynamical equation Eq. (3.29). In the limit $\gamma \to \infty$, Eq. (3.29) is dominated by its second term, which allows us to simultaneously remove both γ and τ dependences by rescaling $t \to \gamma^{-1/3}\tau^{2/3}t'$ and $\boldsymbol{k} \to (\gamma\tau)^{-1/3}\boldsymbol{k}'$, which in turn leads to the scaling as claimed above.

3.4.5 Numerical demonstration of temporal scaling

To test the above universal scaling behaviors, we propose to monitor the topological response of the fermion system as it is tuned between the topological and trivial phases. The topological response that typically characterizes Chern insulators is the Hall conductivity, which can be measured in transport experiments.

To define the instantaneous Hall conductivity for nonequilibrium systems, we consider perturbing the system by a weak electric field $\boldsymbol{E}(t)$ cranked up over a short time scale T,

$$\boldsymbol{E}(t) = \begin{cases} \boldsymbol{E}\, e^{(t-t_0)/T} & \text{for } t \le t_0 \\ 0 & \text{for } t > t_0 \quad . \end{cases} \tag{3.34}$$

We assume that the probe time scale T is much smaller than the quench time τ, i.e. $T \ll \tau$, so that $H(t)$ remains almost unchanged during this period, and can be approximated by $H(t_0)$. In response to the perturbation, the current can be calculated from the current-current correlation function $\Pi(t_0,t)$, using $-\partial_t \boldsymbol{A}(t) = \boldsymbol{E}(t)$, *viz.*

$$\begin{aligned} \langle \boldsymbol{J}(t_0) \rangle &= \int_{-\infty}^{t_0} \mathrm{d}t\, \Pi(t_0,t) \boldsymbol{A}(t) \\ &= -\boldsymbol{E}\, T \int_{-\infty}^{0} \mathrm{d}t'\, \Pi(t_0, t_0 + t')\, e^{t'/T} \quad . \end{aligned} \tag{3.35}$$

$\Pi(t_0,t)$ is given by standard linear response theory as

$$\Pi(t_0,t) = -\mathrm{i}\,\mathrm{Tr}\left(\left[\boldsymbol{J}(t_0)\,,\boldsymbol{J}(t)\right]\rho(t_0)\right) \quad , \tag{3.36}$$

where $\boldsymbol{J}(t_0) = \partial_{\boldsymbol{A}} H(t_0)$ and at a later time, we have

$$\boldsymbol{J}(t) = U^{\dagger}(t-t_0)\,\boldsymbol{J}(t_0)\,U(t-t_0) \tag{3.37}$$

with $U(t-t_0) \simeq e^{-\mathrm{i}H(t_0)(t-t_0)}$. The Hall conductivity $\sigma_{\mathrm{H}}(t_0)$ can be read off from Eq. (3.35),

$$\sigma_{\mathrm{H}}(t_0) = \mathrm{i}\,T\int_{-\infty}^{0} \mathrm{d}t'\, e^{t'/T}\,\mathrm{Tr}\left(\left[J_x(t_0)\,, J_y(t_0+t')\right]\rho(t_0)\right) \quad . \tag{3.38}$$

Here, we assume that $\rho(t_0)$ does not significantly vary during the short time scale T. Employing $H(t_0)$ and $\rho(t_0)$ from Eq. (3.21) and Eq. (3.24), we obtain the instantaneous Hall conductivity $\sigma_{\mathrm{H}}(t_0)$ in terms of the pseudo-spin vector $\boldsymbol{n}_{\boldsymbol{k}}(t_0)$ and pseudo-magnetic field $\boldsymbol{h}_{\boldsymbol{k}}(t_0)$,

$$\sigma_{\mathrm{H}} = \frac{1}{2}\int \mathrm{d}^2k\, \frac{\boldsymbol{n}_{\boldsymbol{k}}\cdot\left(\partial_{k_x}\boldsymbol{h}_{\boldsymbol{k}} \times \partial_{k_y}\boldsymbol{h}_{\boldsymbol{k}}\right)}{\boldsymbol{h}_{\boldsymbol{k}}^2 + T^{-2}} \quad . \tag{3.39}$$

As a special case, when the system equilibrates to the ground state, *i.e.* $\boldsymbol{n}_{\boldsymbol{k}} = -\hat{\boldsymbol{h}}_{\boldsymbol{k}}$, Eq. (3.39) then reduces to $\sigma_{\mathrm{H}} = -2\pi w$ in the static limit $T \to \infty$, where $w \in \mathbb{Z}$ is the band winding number defined in Eq. (3.22), as expected in the quantum Hall effect. However, away from equilibrium, the Hall conductivity does not need to be quantized.

From Eq. (3.39), we calculate the behavior of the Hall conductivity as the system is quenched from a topological band structure ($w = -1$) to a trivial band structure ($w = 0$). The result is shown in Fig. 3.6. The Hall conductivity deviates from the original quantized value and relaxes to a new quantized value after the quench. It is worth mentioning that several prior studies[119, 124] have stressed that the Chern number of the fermion state, which is defined only

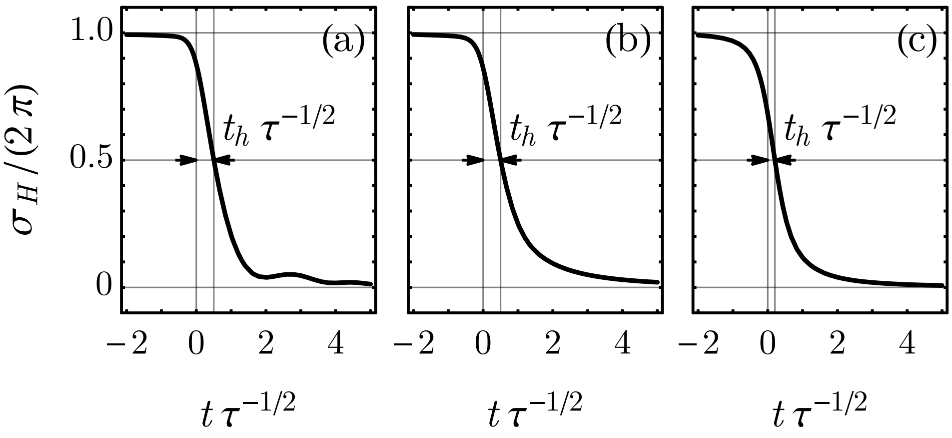

Figure 3.6. Hall conductivity across the quench (from topological to trivial phase) with the decoherence rate (a) $\gamma = 0$, (b) $\gamma = \tau^{1/2}$, (c) $\gamma = 10\,\tau^{1/2}$. The arrows indicate the time scale t_h at which the Hall conductivity relax to halfway between the initial and final quantized values.

for pure states under coherent evolution, and is given by

$$C = \frac{1}{4\pi}\int \mathrm{d}^2k\, \boldsymbol{n_k}\cdot\frac{\partial \boldsymbol{n_k}}{\partial k_x}\times\frac{\partial \boldsymbol{n_k}}{\partial k_y} \tag{3.40}$$

remains unchanged across the quantum quench, simply because the continuous time evolution of $\boldsymbol{n_k}$ is a smooth deformation that can not change the topological index. While this is a correct statement, its meaning may be misinterpreted. The conservation of Chern number does not imply that the system remains in the original phase, because the Chern number is not a physical observable and can not be used to characterize the topological property of a system. Topological properties must be characterized by physical responses, such as the Hall conductivity, which *does* switch between different quantized values across the quench (as shown in Fig. 3.6(a)), even if the Chern number remains the same under coherent evolution.

To further understand the relaxation of Hall conductivity and its associated universal scaling near the critical point, we invoke the linearized model Eq. (3.23), for which the Hall

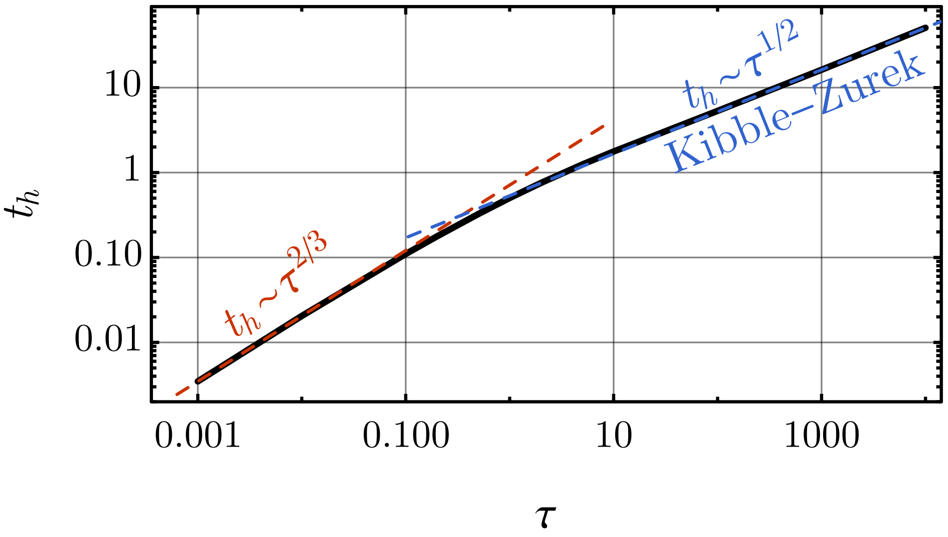

Figure 3.7. The Hall conductivity σ_H is calculated under different quench rate $1/\tau$, from which the halfway time t_h is extracted. This timescale, t_h, exhibits two different scaling behaviors, consistent with Eq. (3.42).

conductivity becomes[2]

$$\sigma_\mathrm{H}(t) = \frac{1}{2}\int \mathrm{d}^2k\, \frac{n^z_{\boldsymbol{k}}(t)}{\boldsymbol{k}^2 + (t/\tau)^2 + T^{-2}}. \tag{3.41}$$

After the quench, in the long time limit, the denominator is dominated by the $(t/\tau)^2$ term, and the numerator $n^z_{\boldsymbol{k}}$ becomes concentrated about the Dirac point within the momentum range $\bar{k}$, as shown in Fig. 3.4(e). So the integral scales as $\sigma_\mathrm{H}(t) \sim \bar{k}^2/(t/\tau)^2 \sim (t/\bar{t})^{-2}$, where the time scale $\bar{t} \sim \bar{k}\tau$ is introduced according to Eq. (3.30) and Eq. (3.33) in both weak and strong decoherence regimes. Thus we conclude that the Hall conductivity relaxes to the new equilibrium with a power-law tail behaving as $(t/\bar{t})^{-2}$.

We can estimate the time scale $\bar{t}$ from the Hall conductivity data. One possibility is to consider the time t_h at which the Hall conductivity relaxes to halfway between the initial and final value, *i.e.* $\sigma_\mathrm{H}(t_\mathrm{h}) = \frac{1}{2}$ (see Fig. 3.6). Because $\bar{t}$ is the only time scale governing the critical quench, the halfway time t_h is expected to scale in the same way as $\bar{t}$. If we fix the decoherence

---

[2] The Hall conductivity should be regularized by an additional factor of $\frac{1}{2}$ in the case of the linearized model. This regularization is due to the Brillouin zone boundary. We ignore the regularization here, as it does not affect any scaling analysis.

rate γ by controlling the temperature and the environmental coupling and perform the quench experiment with different quench rates $1/\tau$, we should expect the following scaling behavior of $\bar{t}$:

$$\bar{t} \sim \begin{cases} \tau^{2/3} & \text{for } \tau \ll \gamma^2, \\ \tau^{1/2} & \text{for } \tau \gg \gamma^2 \quad . \end{cases} \tag{3.42}$$

This behavior is verified in Fig. 3.7 by our numerical simulations. It provides a testable prediction for the scaling behavior of the decoherent critical quench. Observation of the crossover from the $\frac{1}{2}$ to the $\frac{2}{3}$ power laws will then serve as an indicator of decoherence in quantum quench dynamics.

3.4.6 Numerical demonstration of spatial scaling

To demonstrate the universal scaling of the length scale $\bar{\xi}$ after the quench, we break space-translational symmetry by weak disorder, and investigate the disorder-induced inhomogeneous spatial distribution of the excitation density in the final state. For this purpose, we study the spinless Bernevig-Hughes-Zhang (BHZ) model[137] with bond disorder. Following a similar quench protocol to that described above, we can elicit the decoherence-driven crossover of scaling behaviors in real space.

Our purpose of introducing disorder is merely to provide some randomness to seed the spatial inhomogeneity after the critical quench. However, introducing disorder at a quantum critical point can sometimes alter the universal properties, as the disorder can be relevant, which then drives the system to a strong disorder fixed point that is distinct from the clean limit[138]. To prevent the disorder from affecting the universality, we add irrelevant disorder, such as bond disorder (*i.e.* random modulation of bond strengths)[3].

We consider the following lattice model, with static randomness in the hopping amplitude

---

[3] Although mass disorder is marginally irrelevant for (2+1)D Dirac fermions, given the finite system size in our numerics, mass disorder would still have a considerable effect. For this reason, we do not consider it.

and the time-dependent on-site potential:

$$
\begin{aligned}
H(t) = \sum_{\boldsymbol{r}} \sum_{\mu \in \{x,y\}} \left\{ t_{\boldsymbol{r}} c^{\dagger}_{\boldsymbol{r}+\hat{\mathrm{e}}_{\mu}} \left(\sigma^{z} - \mathrm{i}\, \sigma^{\mu} \right) c_{\boldsymbol{r}} + \text{h.c.} \right\} \\
+ \big(m(t) - 2 \big) \sum_{\boldsymbol{r}} c^{\dagger}_{\boldsymbol{r}} \sigma^{z} c_{\boldsymbol{r}} \quad ,
\end{aligned}
\tag{3.43}
$$

where $c_{\boldsymbol{r}} = (c_{\boldsymbol{r}1}\,, c_{\boldsymbol{r}2})^{\mathsf{T}}$, $c_{\boldsymbol{r}\alpha}$ annihilates a fermion at site $\boldsymbol{r}$ in orbital α, and $\hat{\mathrm{e}}_{\mu}$ is a unit vector in the $\mu \in (x,y)$ direction. The mass term $m(t) = t/\tau$ is linear in time. The hopping term $t_{\boldsymbol{r}} = 1 + \delta t_{\boldsymbol{r}}$ fluctuates with $\delta t_{\boldsymbol{r}}$, independently drawn from uniform distribution over $[-\delta t\,, +\delta t]$. The disorder strength δt is irrelevant to the critical behavior and fixed at $\delta t = 0.1$ in our simulation.

The quench dynamics is described by the master equation of Eq. (3.6). Although a Gaussian state does not remain Gaussian under this evolution in general, we make the approximation to project the density matrix to the single particle subspace $\mathscr{P}_{ab} = \mathrm{Tr}\left(c_{b} c^{\dagger}_{a} \rho \right)$. Then, given the quadratic Hamiltonian $H = \sum_{a,b} \mathscr{H}_{ab} c^{\dagger}_{a} c_{b}$, one can derive the equation

$$
\frac{\partial \mathscr{P}}{\partial t} = -\mathrm{i}\,[\mathscr{H}, \mathscr{P}] - \gamma \left[\mathscr{H}, [\mathscr{H}, \mathscr{P}] \right] \quad . \tag{3.44}
$$

Our quench protocol starts with the disordered spinless BHZ Hamiltonian $H(t_0)$ given in Eq. (3.43) having $m(t_0) = -0.5$ and a random profile of $\delta t_{\boldsymbol{r}}$. We use 30×30 site square lattice in which the chemical potential is chosen to yield a half-filled band. The initial density matrix in its first quantization form can be expressed as the projection operator onto the states below the Fermi level, *viz.*

$$
\mathscr{P}(t_0) = \sum_{n} |\psi_n(t_0)\rangle \langle \psi_n(t_0)|\, \Theta\big(-E_n(t_0) \big) \quad , \tag{3.45}
$$

where $|\psi_n(t_0)\rangle$ is the instantaneous eigenstate of $H(t_0)$ with the eigenenergy $E_n(t_0)$, and $\Theta(x)$ is a step function guaranteeing that only negative energy states are included in the sum. The time evolution of the density matrix $\mathscr{P}$ follows Eq. (3.44) until t_{f} such that $m(t_{\mathrm{f}}) = 0.5$. The spatial distribution of any physical observable O can be computed as $O(\boldsymbol{r}) = \sum_\alpha \left\langle \boldsymbol{r},\alpha \,\middle|\, O\,\mathscr{P}(t_\mathrm{f}) \,\middle|\, \boldsymbol{r},\alpha \right\rangle$ for each random realization. We average the disorder over 50 different random realizations.

Following the recent study of Kibble-Zurek behavior in disordered Chern insulators[139], we utilize the spatial excitation density as a physical observable and extract the correlation length scale from the spatial autocorrelation function. The operator for the excitation density is the projector onto the positive energy bands of the final Hamiltonian $H(t_\mathrm{f})$, *viz.*

$$\mathscr{P}_{\mathrm{ex,f}} = \sum_n |\psi_n(t_\mathrm{f})\rangle\langle\psi_n(t_\mathrm{f})|\,\Theta\big(E_n(t_f)\big), \tag{3.46}$$

and the spatial excitation density is given by

$$f_{\mathrm{ex}}(\boldsymbol{r}) = \sum_\sigma \left\langle \boldsymbol{r},\sigma \,\middle|\, \mathscr{P}_{\mathrm{ex,f}}\,\mathscr{P}(t_\mathrm{f}) \,\middle|\, \boldsymbol{r},\sigma \right\rangle \quad . \tag{3.47}$$

The time evolution of the spatial excitation density in a specific random realization is shown in Fig. 3.8. Initially, the spatial excitation pattern is determined by the bond disorder. In the earliest stage of the evolution, the system evolves adiabatically, and the spatial excitation pattern remains almost unchanged until the freeze-out time $t/\tau = -0.2$. After $t/\tau = -0.2$, the evolution becomes diabatic and the spatial excitation pattern reshapes significantly. After passing the second freeze-out time $t/\tau = +0.2$, the evolution is again quasi-adiabatic and the pattern of the spatial excitation density again remains mostly unchanged.

To extract the length scale from the spatial excitation density $f_{\mathrm{ex}}(\boldsymbol{r})$, we compute the auto-correlation function $A(r)$,

$$A(r) = \sum_{\boldsymbol{r},\boldsymbol{r}'} \delta f_{\mathrm{ex}}(\boldsymbol{r})\,\delta f_{\mathrm{ex}}(\boldsymbol{r}')\,\delta_{|\boldsymbol{r}-\boldsymbol{r}'|,r} \Big/ \sum_{\boldsymbol{r}} \big(\delta f_{\mathrm{ex}}(\boldsymbol{r})\big)^2 \quad , \tag{3.48}$$

where $\bar{f}_{\mathrm{ex}} = V^{-1}\sum_{\boldsymbol{r}} f_{\mathrm{ex}}(\boldsymbol{r})$ is the average excitation density and $\delta f_{\mathrm{ex}}(\boldsymbol{r}) \equiv f_{\mathrm{ex}}(\boldsymbol{r}) - \bar{f}_{\mathrm{ex}}$. We collect the auto-correlation $A(r)$ for each random realization separately, which typically exhibits

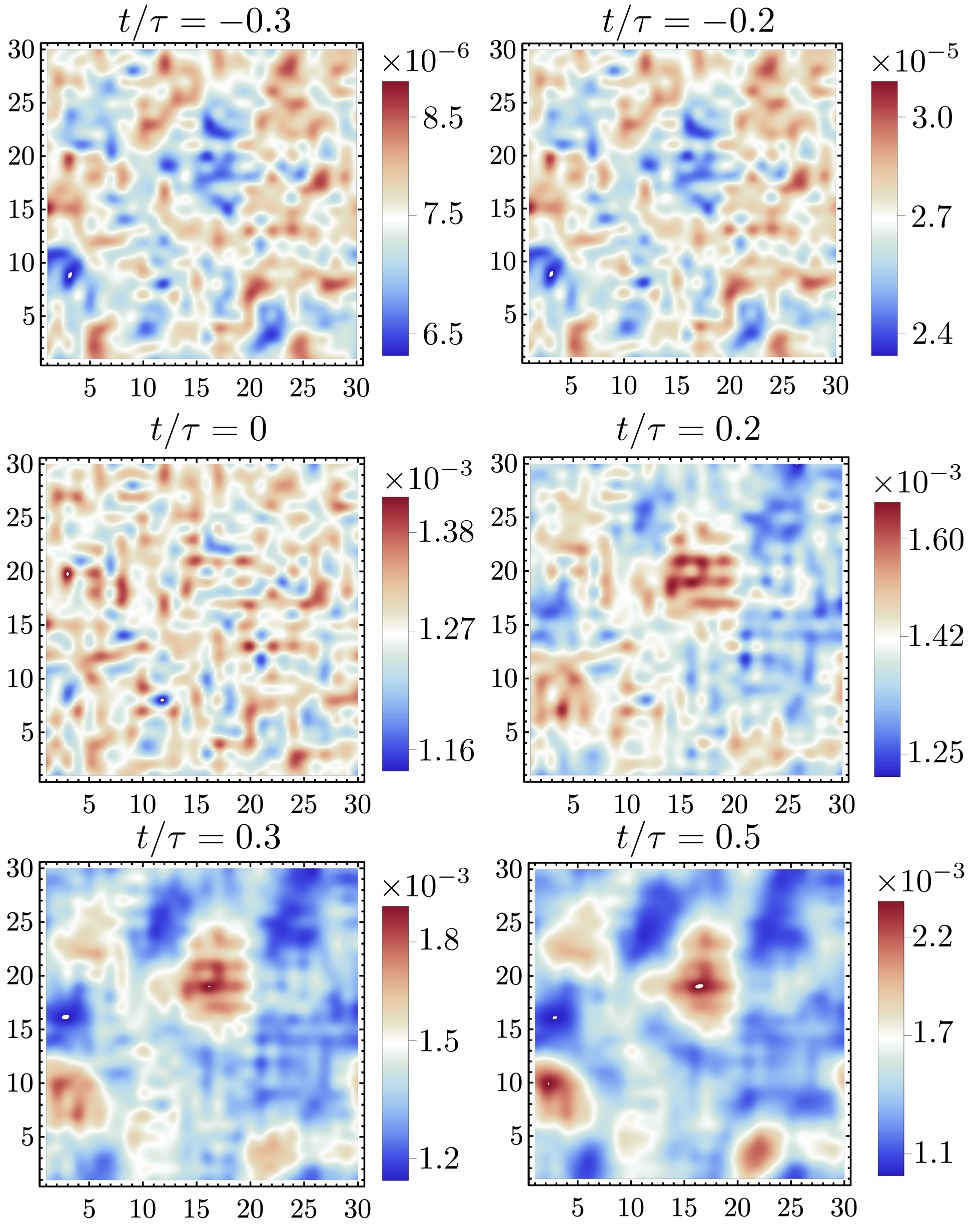

Figure 3.8. Time evolution of the excitation density distribution $f_{\text{ex}}(\boldsymbol{r})$ across the critical quench.

an exponentially decaying behavior in r. We define the correlation length ξ as the length scale when $A(\xi) \to 0$. For each quench rate $1/\tau$, we compute the disorder-averaged correlation length

$\bar{\xi}$. From the scaling behavior mentioned above, we expect the following scaling behavior of $\bar{\xi}$:

$$\bar{\xi} \sim \begin{cases} \tau^{1/3} & \text{for } \tau \ll \gamma^2, \\ \tau^{1/2} & \text{for } \tau \gg \gamma^2. \end{cases} \tag{3.49}$$

This behavior is supported by our numerical simulations, as shown in Fig. 3.9. Thus we have demonstrated that the scaling of the freeze-out length scale $\bar{\xi}$ can be extracted from the excitation density profiles after the quench, which provides another experimental scheme to test the proposed scaling behavior.

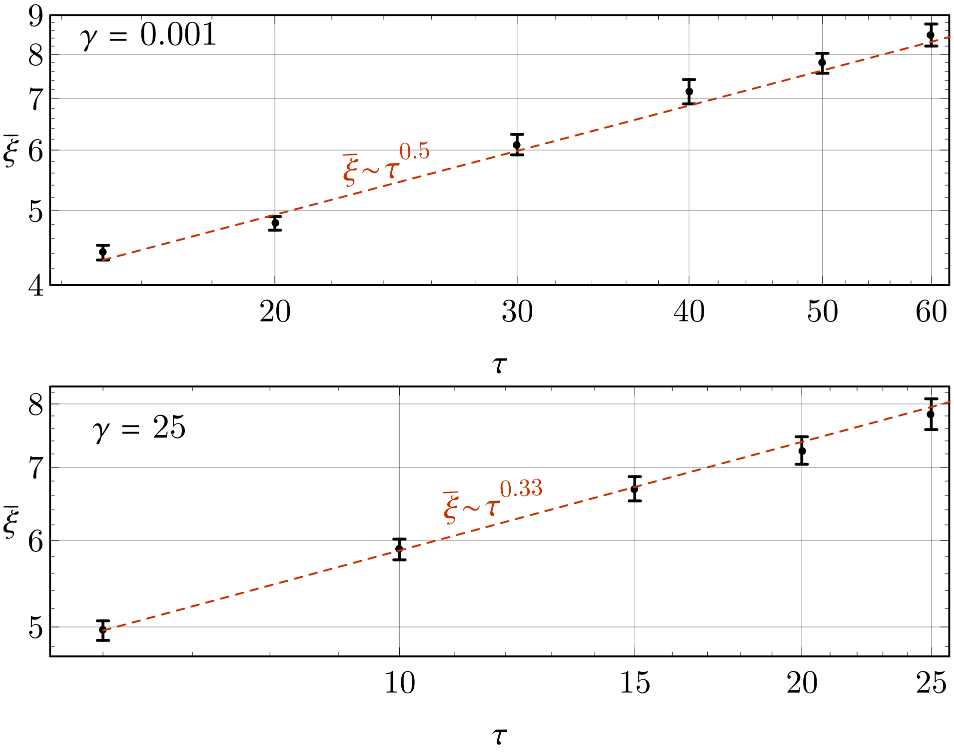

Figure 3.9. The correlation length scale ξ_r in each trial is defined by the spatial decay of auto-correlation function $A(\xi_r)$ defined inEq. (3.48). The disorder averaged $\bar{\xi}_r$ is obtained from 50 trials. The critical exponents in the strong and weak decoherence limits are consistent with Eq. (3.49).

3.5 Summary and outlook

In conclusion, we have offered a framework for studying the quantum critical quench dynamics in the presence of decoherence in the energy basis, corresponding to the system energy being continuously monitored by its environment. In the strong decoherence limit, we have found a cross-over to a scaling regime (Eq. (3.20)) that differs from that on the standard Kibble-Zurek form and is governed by the freeze-out time $\bar{t} \sim \tau^{2\nu z/(1+2\nu z)}$ and the freeze-out length $\bar{\xi} \sim \tau^{2\nu/(1+2\nu z)}$. This scaling behavior would be universal and manifest in a slew of observables, such as defect densities. We have applied our formulation to the case of quenching through a topological phase transition in a Chern insulating system and shown scaling in the relaxation of the Hall conductivity and in post-quench autocorrelations of post-quench spatial domains of excitation densities.

Immediate further work would involve analyses of scaling behavior in other measurable quantities, such as residual energies and entanglement entropy. While this work has been confined to global quenches, it can also provide a starting point for local quenches across topological transitions. In this case, we expect a highly interesting interplay between propagation of boundary modes and decoherence. As another direction of study, while the topological system in consideration here is two-dimensional, the analysis for such free fermionic models is very easily extendable to other dimensions. In three-dimensions, scaling analyses can be applied and contrasted for observables that target the bulk versus the surface. In one-dimension, the Kitaev chain would offer a beautiful prototype for studying much sought-after Majorana fermion physics and the crucial role of decoherence in topological qubits.

Our results apply to decoherent quench dynamics through generic quantum phase transitions, and is not limited to the topological transition examined in this work. For example, our analysis could be applied to symmetry breaking transitions in spin models of different dimensions, where the post-quench magnetic domain size will follow the scaling behavior of $\bar{\xi}$. In superconductors and Bose-Einstein condensates, our analyses would apply to the generation and dynamics of vortices, now with the twist of having decoherence present. In the presence of more complex order parameters, Kibble-Zurek physics has probed more exotic defects; here too, dissipation effects would give rise to new dynamics and possibly even stabilization of some of these defects.

The discussion of critical quench dynamics in open systems has also been emphasized within other scenarios[140, 141, 142, 143, 144, 145]. Specifically, Ref. [143] studied a critical quench as the system weakly couples to a thermal bath. Ref. [145] studied a critical quench in the presence of dissipation due to the system-environment interaction. The coherent unitary dynamics will compete with dissipative dynamics to determine the time scale when the system falls out of equilibrium. The scaling behavior will cross over from the weak dissipation to the strong dissipation regimes in the vicinity of a crossover temperature T_c [143] or a crossover dissipation rate u_c [145] which scale with the quench rate $1/\tau$ as

$$k_\mathrm{B} T_\mathrm{c} \sim \tau^{-\nu z/(1+\nu z)} \qquad \text{or} \qquad u_c \sim \tau^{-\nu z/(1+\nu z)} \quad . \tag{3.50}$$

In these cases, the system-environment coupling term generally does not commute with the system Hamiltonian, which allows the system to exchange both energy and quantum information with its environment (in the static limit). However, in this work, we considered a different class of system-environment interaction, where the interaction term commutes with the system Hamiltonian, such that the system only exchanges quantum information with the environment, with energy preserved (again in the static limit). In particular, we focused on decoherence in the energy eigenbasis, which can be realized by a quantum non-demolition measurement of the system Hamiltonian. In this case, the coherent dynamics will compete with the decoherent dynamics. Because the correlation time and the decoherence time scale differently with the excitation energy as the system approaches the critical point, their competition leads to the crossover from weak to strong decoherences regimes at a crossover decoherence rate (quantum non-demolition measurement strength) γ_c that scales as $\gamma_\mathrm{c} \sim \tau^{\nu z/(1+\nu z)}$, which resembles the case of dissipation in Eq. (3.50).

Finally, turning to experiments, the range of systems in which quantum Kibble-Zurek physics has been explored provides a very fertile arena for studying the effect of decoherence, both in terms of it being integral to physics systems as well as in accessing the new strong decoherence regime predicted in this work. Controlled tuning and state-of-the-art probes are enabling access to rich non-equilibrium regimes. Critical quantum quench dynamics and associated Kibble-Zurek behavior have been actively studied in superconductors[146, 147, 148] and a variety of ultracold atomic[149, 150, 151, 152, 153] and ionic systems[154, 155, 156]. Kibble-Zurek scaling has been recently applied to identify universality classes of quantum critical points in experiments[157, 158, 159]. While any of these systems could perhaps form candidates for probing decoherence effects, the specific instance of Chern insulators studied here could potentially be realized in cold atom systems[124, 125, 160] and Moire superlattice systems[161, 162, 163, 164, 165, 166, 167]. With regards to settings where decoherence is naturally present, perhaps the most germane situations involve qubits, and quantum simulators and annealers[168, 169, 170, 171, 172]; with the increasing focus on quantum information and computation, and the need to harness speed and efficient switching of quantum states, understanding the interplay between quantum quenching and decoherence is now crucial.

Chapter 3 is, in part, a reprint of material from published work done in collaboration with Daniel P. Arovas, Smitha Vishveshwara,and Yi-Zhuang You, as it appears on Scipost. Wei-Ting Kuo, Daniel P. Arovas, Smitha Vishveshwara, and Yi-Zhuang You, ”Decoherent Quench Dynamics across Quantum Phase Transitions,” SciPost Phys. 11, 084 (2021). The dissertation author was the primary investigator and author of this material.

Chapter 4

One particle perspective of nonequilibrium steady state property for Aubry-Andre-Harper model under dissipative and decoherent dynamics

4.1 Synopsis

We investigate the one-dimensional Aubry-André-Harper model of fermion hopping in a quasiperiodic potential and coupled to an external environment. The dynamics of the system's density matrix are modeled by the Gorini-Kossakowski-Sudarshan-Lindblad (GKLS) master equation, with jump operators corresponding to random dissipative and decohering processes. While the Liouvillian itself is non-Hermitian and has a complex eigenspectrum, the NESS itself is Hermitian and may be written as $\rho = \exp(-K)$. We investigate the properties of the resulting non-equilibrium steady state (NESS) density matrices, including participation ratio, von Neumann entropy, logarithmic negativity, and adjacent gap ratios for K. Our results indicate that there is one phase for the NESS, which undergoes a crossover behavior between regimes of small and large localization length.

4.1.1 Contribution of the author

The author has contributed in developing the formalism and in writing this paper. He has performed numerical analysis together with Jyotsna Gidugu.

4.2 Introduction

Identifying and investigating multiple phase properties under different theoretical or experimental settings is a key topic in condensed matter field. One important and common example is the delocalized phase which could result from periodic lattice structure[173]. The breaking of periodicity, by adding disorder or quasi-periodic potential, leads to the localization phase. In low dimensions ($d = 1, 2$), any non-vanishing disorder drives the system to the localization phase, also known as Anderson localization[174, 175]. As for the quasi-periodic potential, the delocalization-localization phase transition occurs at finite potential strength[176, 177, 178]. The localized and delocalized phases can be characterized by the static and dynamical probes. The static probes study the wave function distribution (e.g. localization length[179] and inverse participation ratio) or the spectral statistics of the Hamiltonian (e.g. adjacent gap ratio[180]); whereas the dynamical probe focuses on how the initial localized wave function spreads out over the system volume. These multiple probes help us identify and reveal different phase properties in closed system.

In open system, similar dynamical probes can be realized in boundary-driven system which couples the system boundaries with two reservoirs with different temperature/chemical potential. The energy/particle gradient created by the reservoirs leads to a persistent steady current j_∞ with the resistance $R = 1/j_\infty$. The size-dependent resistance in one dimension is $R \sim L^\beta$ and reveals diffusive ($\beta = 1$), subdiffusive ($\beta > 1$) and localization (divergent β) behaviors. The different transport properties are highly sensitive to the disorder[181, 182, 183, 184, 185], the incommensurate potential[186, 187, 188], many-body interaction term[189, 190, 191, 192], and recently studied on-site dephasing term[193, 194, 195]. The transport properties characterized by steady currents lead to rich discoveries of phases. However, if the system fails to maintain a conserved current, could we utilize different probes to diagnose the non-equilibrium system ? Here, we would like to address this problem by utilizing multiple one-particle probes to study the non-equilibrium steady state under dissipative and dephasing dynamics. One particle probes can be computed from the one particle correlation matrix alone. The reason for using one-particle probes is two-fold. First, the commonly used dynamical probe is also a one-particle probe. The off-diagonal entries of the one-particle correlation matrix were required to compute the dynamical probe. Its ability to distinguish different phases motivates us to use other one-particle probes. With more information from the one-particle correlation matrix, we expect to obtain richer information about different phases in open system. Second, one-particle probes can provide potential connections between open and closed system where many one-particle probes have provided much understanding of different phases. Using similar probes enables us to learn the similarity and difference between phases in open and closed system. The rest of this paper is organized as follows. In Sec. 4.3, we introduce our formalism to describe the dissipative and dephasing dynamics and define all the one-particle probes used in our study. Their results and further discussion are also provided. Sec. 4.4 summarizes our work and points out potential future directions.

4.3 Model and result

We start with the Lindblad master equation which describes the nonunitary dynamics of the system coupled to a Markovian environment[196] and is given by,

$$\frac{d\rho(t)}{dt} = -i[H,\rho(t)] + \sum_{\mu}\left(L_\mu \rho(t) L_\mu^\dagger - \frac{1}{2}\{L_\mu^\dagger L_\mu, \rho(t)\}\right) \tag{4.1}$$

where $\rho(t)$ and H are the density matrix and Hamiltonian of the system. L_μ is the Lindblad operator which represents how environmental coupling affects the system. To explore how one-dimensional localized and extended states evolve under environmental coupling, we consider the one-dimensional Aubry-Andre-Harper (AAH) Hamiltonian,

$$H = \sum_n c_{n+1}^\dagger c_n + c_n^\dagger c_{n+1} + 2\Delta \cos(2\pi n\beta) c_n^\dagger c_n. \tag{4.2}$$

where n labels the site index and β is an irrational number. The first term represents the nearest-neighboring hopping, and the second term stands for the quasi-periodic incommensurate potential. The competition between these two terms leads to the delocalization-localization phase transition at $\Delta = 1$ [176, 177, 178]. In our model setup, we apply open boundary condition and choose β as the inverse of the golden ratio ($\beta = (\sqrt{5}-1)/2$).

We consider three kinds of on-site Lindblad operators, the gain operator (L_g), the loss operator (L_l), and the dephasing operator (L_{de}),

$$L_{g,n} = \sqrt{W_n^+} c_n^\dagger, L_{l,n} = \sqrt{W_n^-} c_n, L_{de,n} = \sqrt{\Gamma_n} c_n^\dagger c_n. \tag{4.3}$$

The gain and loss operators add and remove particles in our system, which couple different particle number sectors and represent the dissipative dynamics. These two operators would be also called the dissipative Lindblad operators in our work. As for the dephasing operator, it adds dephasing noise to the system without changing the number of particles. In this work, we study the interplay between the strength of the incommensurate potential (Δ) and the strength of the dissipative (W_n^+, W_n^-) and dephasing (Γ_n) Lindblad operators. We consider two kinds of non-unitary evolutions: purely dissipative evolution and dissipative-dephasing evolution. In both cases, we sample the amplitude of the corresponding Lindblad operators (W_n^+, W_n^-)/(Γ_n) from a uniform distribution ranging from zero to W/Γ.

To probe the persistent feature under the dissipative and dephasing dynamics, we focus on the density matrix for the non-equilibrium steady state (NESS) ρ_{ness}. To extract essential features from ρ_{ness}, we utilize the one-particle correlation matrix of the NESS to compute several one-particle probes. The one-particle correlation matrix can be constructed as

$$C_{xy,ness} = \mathrm{Tr}(\rho_{ness} c_x^\dagger c_y). \tag{4.4}$$

To obtain $C_{xy,ness}$, we explicitly compute C_{ness} in purely dissipative dynamics (details in Appendix B.1). As for the dissipative-dephasing dynamics, we utilize iterative algorithm to obtain C_{ness} (details in Appendix B.1) [193, 194, 195].

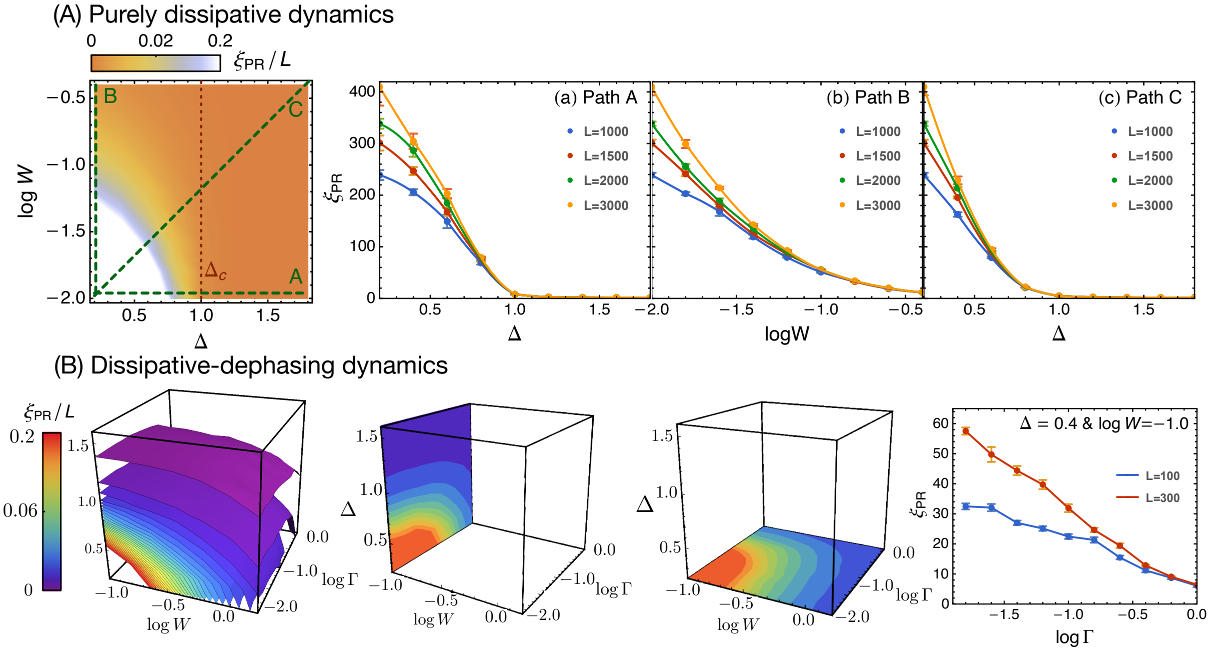

Figure 4.1. Participation ratio for purely dissipative and dissipative-dephasing dynamics. The color plots show the participation ratio under different parameter regimes. The curve plots show different scaling behaviors in the extended and localized phases.

Next, we use the one-particle correlation matrix to compute the following one-particle probes, the averaged participation ratio (PR)[197], von Neumann entropy, and logarithmic negativity. Note that von Neumann entropy and logarithmic negativity computed from the one-particle correlation matrix are exact when the density matrix of the NESS is Gaussian. In our cases, the density matrix would remain Gaussian during the purely dissipative evolution. As for the dissipative-dephasing dynamics, we still compute these quantities based on the one-particle correlation matrix and aim at exploring the phase structure from the one-particle perspective.

First, we start with defining the average participation ratio (PR) and presenting the corresponding results in both dissipative and dissipative-dephasing dynamics. The main ingredients in computing PR from $C_{xy,ness}$ are the eigenvalues $\{n_\alpha\}$ of $C_{xy,ness}$ and their corresponding eigenvectors $\{\psi_\alpha\}$ which are called natural orbitals. The α-th eigenvalue n_α represents the occupation number at the α-th natural orbital ψ_α. Effectively, these natural orbitals represent the eigenstates of the one-particle Hamiltonian H_{one} which can be defined from the one-particle density matrix as $\rho_{one} \sim \exp(-H_{one,ij}c_i^\dagger c_j)$. These are the orbitals where the particles would *naturally* live.

To quantify the property of each natural orbital, we can use the usual definition of the inverse participation ratio (IPR), $\sum_i |\psi_{\alpha,i}|^4$. Hence, the average IPR would be the sum of the IPR weighted by their respective particle number. The average PR ($\bar{\xi}_{PR}$) is simply the inverse of the average IPR,

$$\bar{\xi}_{PR} = (\sum_\alpha n_\alpha \sum_{i=1}^{L} |\psi_{\alpha,i}|^4/(\sum_\alpha n_\alpha))^{-1}. \tag{4.5}$$

When all natural orbitals are strictly localized/extended coherently, the average PR arrives at the value of one/the system size L. This size-dependence of the extended state enables us to distinguish the extended and localized states by computing the PR for multiple system sizes.

Before presenting our average PR results for different strengths of W and Γ, we first discuss the result when the dynamics only contain the dissipative operators and their strengths (W_n^+, W_n^-) are spatially uniform. One can show that the resultant correlation matrix of the NESS is an identity matrix multiplied by a factor ν. This factor ν represents the expectation value of the particle number per site and is controlled by the strength of the gain and loss operators.

The PR result of the NESS under random on-site dissipative and dephasing dynamics is presented in Fig. 4.1. The first row in Fig. 4.1 shows the phase diagram of the average PR when the time evolution is purely dissipative. When the random dissipative strength is weak ($W \sim 10^{-2}$), the system seems to preserve the eigenstate properties in the original AAH model. When $\Delta < \Delta_c$, the PR scales with the system size, which serves as a signature of the extended system. As for $\Delta > \Delta_c$ case, the system-size independent PR represents the localized system.

The main distinction is that the crossover occurs between these two phases instead of the phase transition in the AAH model. This crossover can be verified by both smoothly converging PR and the invariant order of the system size in PR when the system transits between two phases. Similar crossovers can be found if we increase the random dissipative strength such as the path B in Fig. 4.1. This similarity implies that the random on-site dissipation would drive the system to the localized NESS. The second row in Fig. 4.1 shows the phase diagram of the average PR when the time evolution is dissipative-dephasing dynamics. When the on-site potential strength and random dissipative strength are both small ($\Delta = 0.2$ and $W \sim 10^{-2}$), the NESS of the system also tends to cross from the extended phase to the localized phase as the random dephasing amplitude increases. This property suggests that the random on-site dephasing term would also lead to a localized NESS.

Here, we would like to comment the physical meaning of the localization in PR. The PR stands for the spatial coherence length. Since our setup has local dissipative and dephasing Lindbladian operators which lead to quantum decoherence in the positional basis, the system ultimately arrives at the localization in PR when the dissipation and dephasing are strong enough. This conclusion seems to contradict the previous studies which state that the dephasing noise leads to an enhanced transport and destroys the localization [193, 194, 195]. However, the ”localization” in the transport property is different from the ”localization” in PR. Here, we would like to demonstrate a simple example which shows a nonzero steady current and strong localization in PR. This example contains the tight-binding model with the gain and loss operators located on the opposite boundaries and uniform on-site dephasing operators. The hopping amplitude and the boundary couplings W_1^+, W_L^- are set to be one. We choose four different uniform dephasing amplitudes, $\Gamma_n = 0.01, 0.1, 1, 10$. In this setup, the steady current exists for all dephasing amplitudes. Fig. 4.2 show the diagonal entries of the correlation matrix at NESS and the PR for different dephasing amplitudes. The increasing dephasing amplitude drives the on-site particle number from mostly uniform distribution to a linear gradient distribution across the one-dimensional chain. Besides, the PR decreases with the increasing dephasing amplitude. This results from that the linearly decreasing gradient makes the eigenvectors of the one-particle correlation matrix more localized. Physically, this localization occurs due to the decoherence at the positional basis. This simple example demonstrates the possibility of non-vanishing steady current with localized PR.

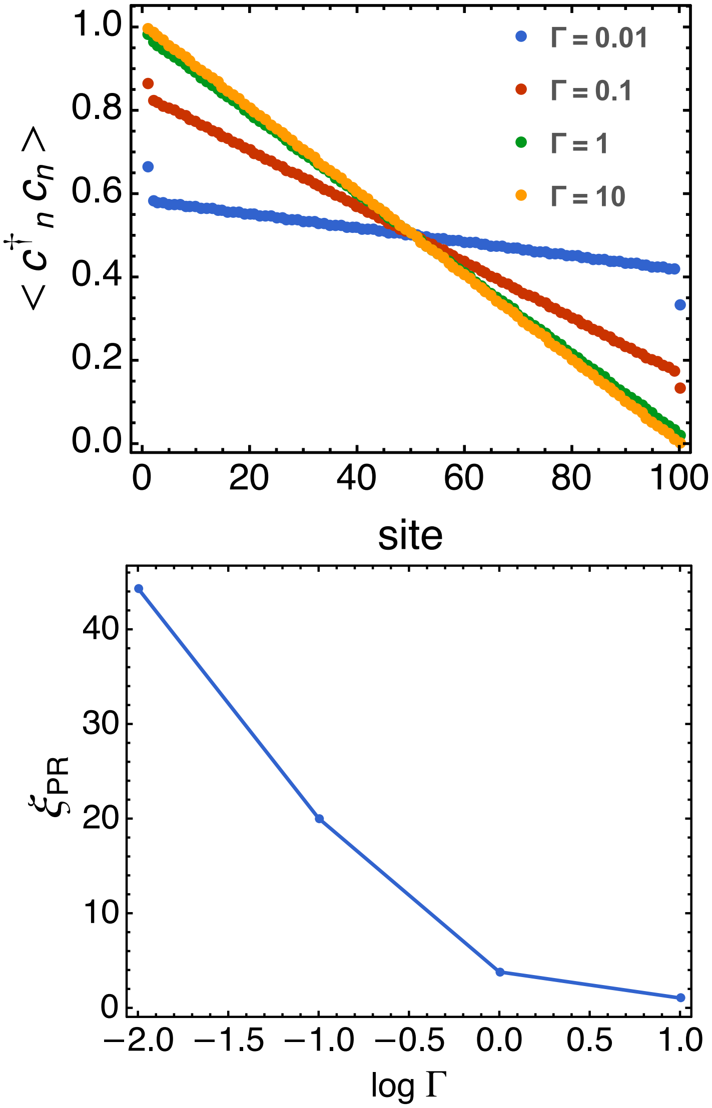

Figure 4.2. The on-site particle number and the PR result for the boundary-driven system under uniformly dephasing coupling.

In addition to the study of PR, we also investigated the spectral statistics of the one-particle Hamiltonian (the results and details are in Appendix B.2). Their results show similar phase structure with that of PR. To further explore the properties of the extended and localized phases in open system, we utilize two quantum information probes, the one-particle von-Neunmann entropy and logarithmic negativity. Typically, their scaling relation with respect to the system size reveals the nature of the phase. The one-particle von Neumann entropy (S_{one}) is defined as

$$S_{one} = -\sum_i [n_{i,sub} \log n_{i,sub} + (1 - n_{i,sub}) \log(1 - n_{i,sub})] \tag{4.6}$$

where $n_{i,sub}$ are the eigenvalues of the $n_{sub} \times n_{sub}$ submatrix of the full correlation matrix at NESS. For the mixed density matrix, the von Neumann entropy measures the classical correlations between the system and environment. Since our dissipative and dephasing Lindblad operators couples the system with environment locally, the von Neumann entropy would increase linearly with the sub-system size. This linear behavior can be also seen in the one-particle von Neumann entropy for both dissipative and dissipative-dephasing dynamics (in Fig. 4.3). Moreover, the extended and localized phases exhibit different entropy slopes in the plot of entropy versus system size. To better quantify this difference, we define the von Neumann entropy density, $s_{one} = S_{one}/N$, which represents the increment of classical correlation between system and environment when one extra site is added. The phase with larger entropy density (e.g. the extended phase) implies a stronger classical correlation. In purely dissipative dynamics, increasing the strength of the quasi-potential and dissipative operator both lead to decreasing entropy densities (shown in the first row in Fig. 4.4). Under the dephasing and dissipative dynamics, however, the entropy density increases with the dephasing amplitudes (shown in the second row in Fig. 4.4), especially in large quasi-potential strength regime. This dephasing-enhanced classical correlation resonates with the previous studies of the dephasing-enhanced transport phenomena.

The last probe is the one-particle logarithmic negativity [198, 199, 200, 201]. The logarithmic negativity is used as a probe to capture quantum correlation in the mixed state. To define the one-particle logarithmic negativity, we first define the covariance matrix (Ξ) from the

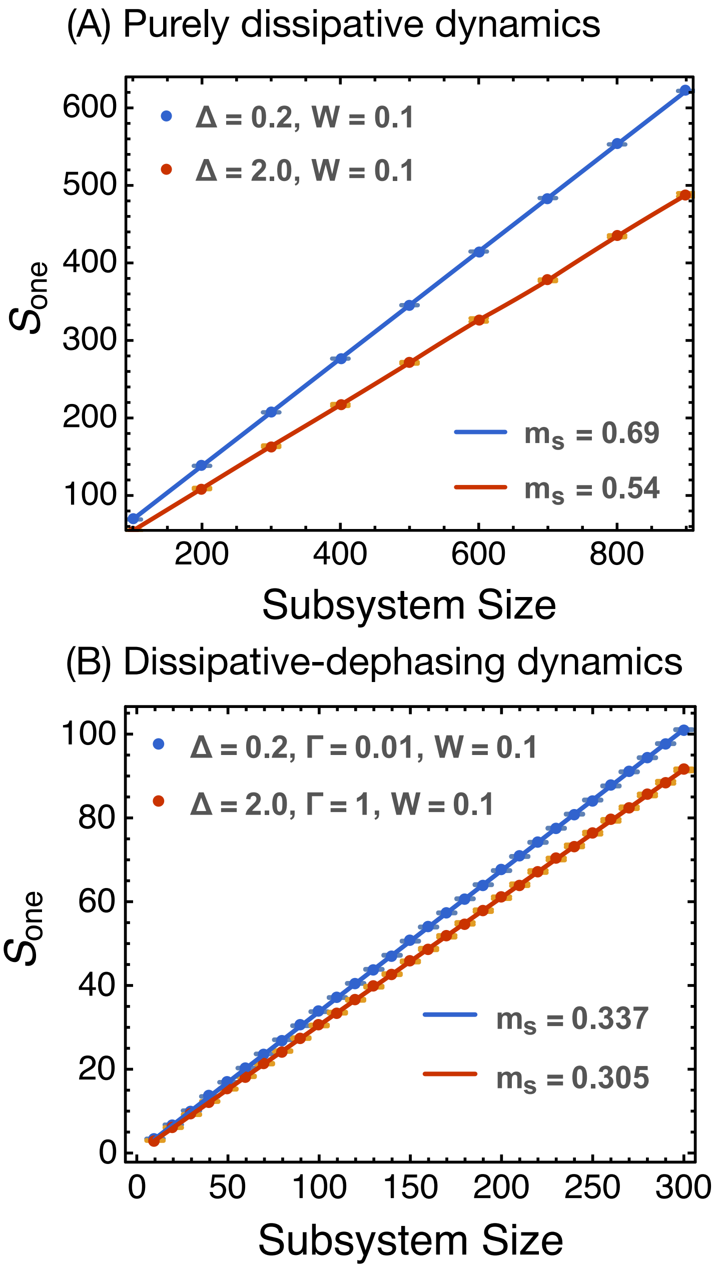

Figure 4.3. The plot of the one-particle entropy versus the subsystem size under purely dissipative and dissipative-dephaing dynamics.

one-particle correlation matrix (C) as $\Xi = \mathbb{I} - 2C$. Next, we divide the full system into two parts, $A, \bar{A}$ and construct the transformed matrix (C_Ξ) as

$$C_\Xi = \frac{1}{2}\left[\mathbb{I} - \left(\mathbb{I} + \Xi_+ \Xi_-\right)^{-1}\left(\Xi + + \Xi -\right)\right] \tag{4.7}$$

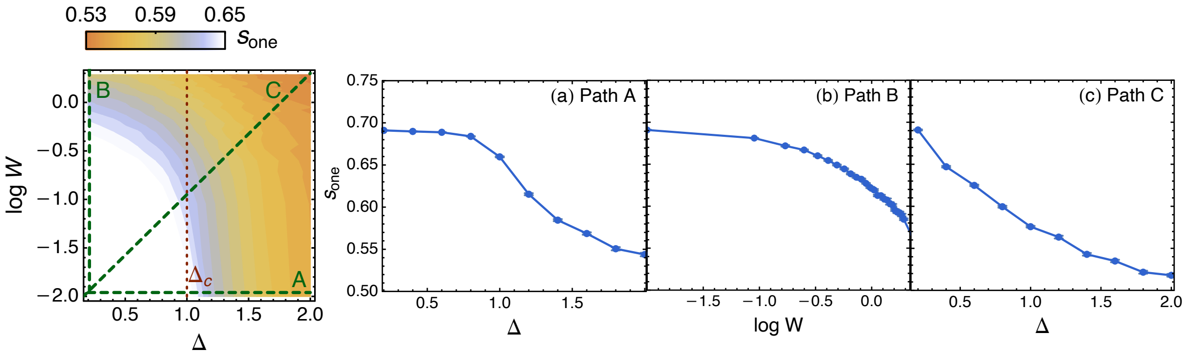

(A) Purely dissipative dynamics

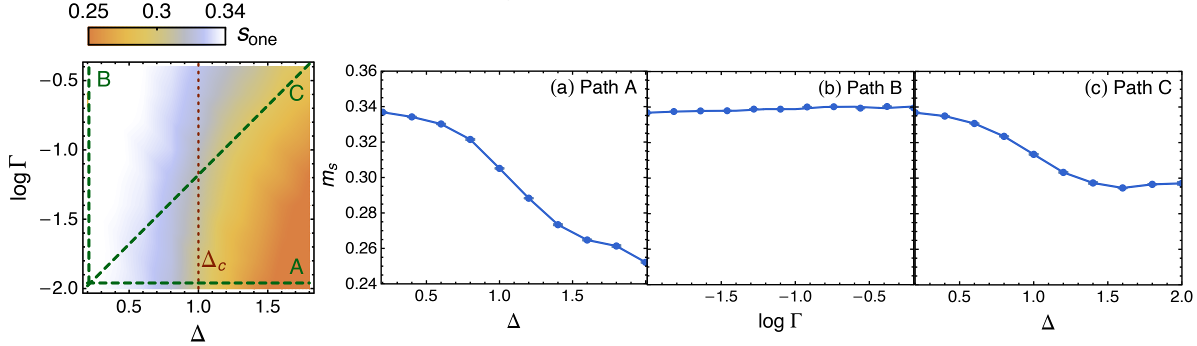

(B) Dissipative-dephasing dynamics for $\log W = -1.0$

Figure 4.4. The slope of the one-particle entropy volume-law curve for different parameter regimes.

where $\Xi_\pm$ can be constructed from the covariance matrix,

$$\Xi_\pm = \begin{pmatrix} -\Xi_{AA} & \pm \mathrm{i}\Xi_{A\bar{A}} \\ \pm \mathrm{i}\Xi_{\bar{A}A} & \Xi_{\bar{A}\bar{A}} \end{pmatrix} \tag{4.8}$$

Suppose the eigenvalues of the correlation matrix (C) and the transformed matrix (C_Ξ) are $\{n_i\}$ and $\{\xi_i\}$, the one-particle logarithmic negativity (E) is defined as

$$E = \sum_i \ln\left[\xi_i^{1/2} + (1-\xi_i)^{1/2}\right] + \frac{1}{2}\sum_i \ln\left((1-n_i)^2 + n_i^2\right). \tag{4.9}$$

Due to the widespread dissipative and dephasing operators in the system, the long-range quantum correlation would fail to persist and only live on the boundary, which would give us the area-law relation between the negativity and sub-system size. The one-particle logarithmic negativity (the panel (a) in Fig. 4.5) quickly increases for small sub-system sizes and then arrives at the plateau with a constant negativity value. This behavior appears in the extended and localized phases but with different plateau values. When both dephasing and dissipative strengths are weak, the plateau value for half-system size would cross from the extended value to the localized one as the quasi-potential strength increases. In strong dephasing limit, the plateau values stays small (the panel (b) in Fig. 4.5). This suggests that the on-site dissipative and dephasing Lindblad operators reduce the quantum correlation existing in the system.

(A) Purely dissipative dynamics

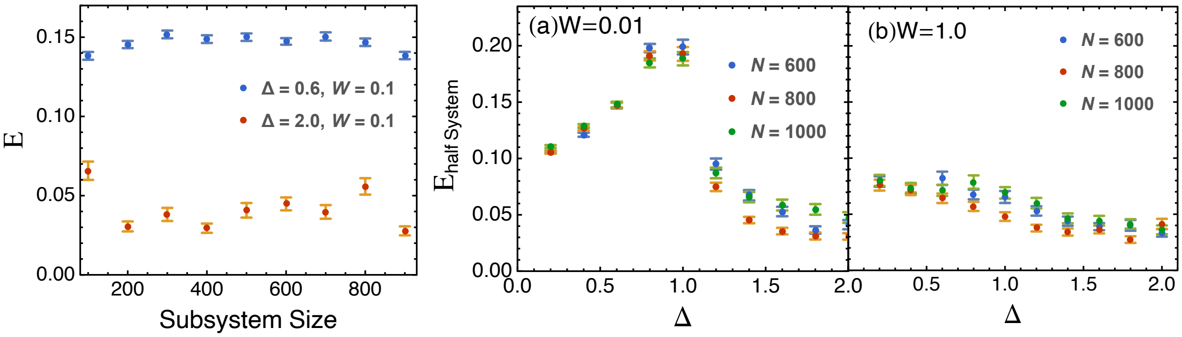

(B) Dissipative-dephasing dynamics

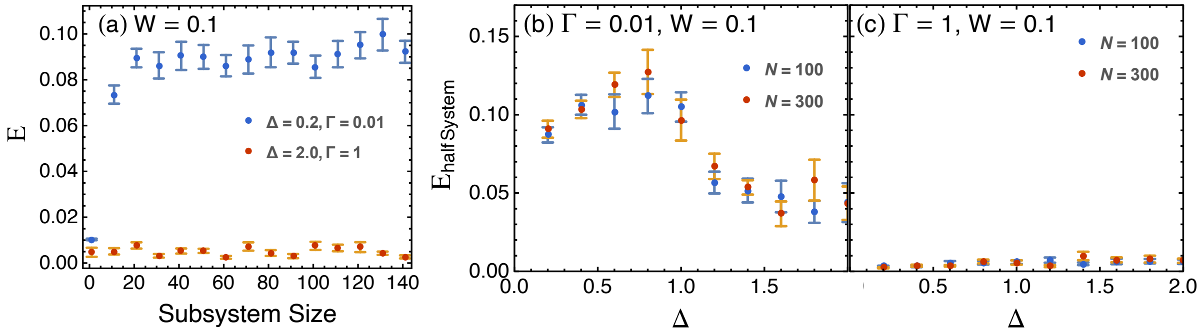

Figure 4.5. (a) The plot of the one-particle logarithmic negativity versus the subsystem size under purely dissipative and dissipative-dephaing dynamics. (b,c) The one-particle logarithmic negativity of the half-system size for different parameter regimes.

4.4 Summary and outlook

Here, we presented results from several one-particle probes for the non-equilibrium steady state of the Aubry-Andre model under dissipative and dephasing dynamics. For strong enough dissipative and dephasing Lindblad operators, the system would ultimately arrive at the localized NESS; whereas in the weak dissipative and dephasing cases, the system exhibits a delocalization-localization crossover when we tune the strength of the quasi-periodic potential. We also discussed and compare the difference between the localization in participation ratio and that in transport property. Both extended and localized phases show volume-law classical correlation and area-law quantum correlation but with different slopes and saturation plateau values. Our results show the ability of one-particle probes to identify fruitful phase structure in open system.

One potential future direction is to study whether the original fractal property still persists under dissipative and dephasing dynamics. One common probe to detect the fractal property in closed system is the generalized inverse participation ratio (GIPR) which computes different moments of the wave function. Following similar idea, we can compute GIPR of the natural orbitals around $\Delta = 1$ in weak dissipative and dephasing Lindblad operators to study whether the fractal critical point still exists.

Chapters 4 is, in part, a reprint of material from work done in collaboration with Jyotsna Gidugu and Daniel P. Arovas, as it will appear on the arXiv. The dissertation author was the primary investigator and author of this material.

Appendix A

Appendix for Chapter 2

A.1 Entanglement feature of page state

The Page state can be considered as a single random tensor. According to Ref. [39], the 2nd Rényi entanglement feature of a random tensor network can be calculated as the partition function of an Ising model,

$$W_{\text{RTN}}[\boldsymbol{\sigma}] = \frac{1}{Z}\sum_{\boldsymbol{\tau}} e^{-E_{\text{RTN}}[\boldsymbol{\sigma},\boldsymbol{\tau}]}, \tag{A.1}$$

where each random tensor is mapped to an Ising spin τ_i coupled together via the network, and the boundary condition pinned by external Zeeman field along the direction specified by $\boldsymbol{\sigma}$. Applying this result to the Page state,

$$W_{\text{Page}}[\boldsymbol{\sigma}] = \frac{1}{Z}\sum_{\tau} e^{\eta \sum_{i=1}^{L} \sigma_i \tau}, \tag{A.2}$$

where there is only one Ising spin τ because the Page state is only a single random tensor. The τ spin couples to the boundary condition $\boldsymbol{\sigma}$ via uniform field strength $\eta = \frac{1}{2}\log d$, which is determined by the qudit Hilbert space dimension d (see Ref. [39] for derivation). Completing the summation over Ising spin τ, we obtain

$$W_{\text{Page}}[\boldsymbol{\sigma}] = \frac{2}{Z}\cosh\left(\eta \sum_{i=1}^{L} \sigma_i\right). \tag{A.3}$$

The normalization constant Z is determined by the condition that $W_{\text{Page}}[\Uparrow] \equiv 1$, such that $Z = 2\cosh(\eta L)$, hence

$$W_{\text{Page}}[\boldsymbol{\sigma}] = \frac{\cosh(\eta \sum_{i=1}^{L} \sigma_i)}{\cosh(\eta L)}, \tag{A.4}$$

which can be rewritten as the EF state $|W_{\text{Page}}\rangle$ in Eq. (2.11).

A.2 Entanglement feature of two-qudit Haar random unitary

Here we derive the ensemble averaged EF operator for two-qudit Haar random unitary gate. We start with the definition

$$W_{U_{ij}}[\boldsymbol{\sigma}, \boldsymbol{\tau}] = \mathrm{Tr}(\mathscr{X}_{\boldsymbol{\sigma}} U_{ij}^{\otimes 2} \mathscr{X}_{\boldsymbol{\tau}} U_{ij}^{\dagger \otimes 2}). \tag{A.5}$$

U_{ij} is a two-qudit gate acting on qudits labeled by i and j. Focusing on these two qudits, the Ising variables $\boldsymbol{\sigma} = (\sigma_i, \sigma_j)$ and $\boldsymbol{\tau} = (\tau_i, \tau_j)$ both contain only two components. Consider averaging the EF $W_{U_{ij}}$ over unitary gates U_{ij} in the Haar random unitary ensemble,

$$\begin{aligned}\mathbb{E}_{U_{ij}\in\text{Haar}} W_{U_{ij}}[\boldsymbol{\sigma}, \boldsymbol{\tau}] &= \mathbb{E}_{U_{ij}\in\text{Haar}} \mathrm{Tr}(\mathscr{X}_{\boldsymbol{\sigma}} U_{ij}^{\otimes 2} \mathscr{X}_{\boldsymbol{\tau}} U_{ij}^{\dagger \otimes 2}) \\ &= \sum_{g,h\in S_2} \mathsf{Wg}(g^{-1}h, d^2)\,\mathrm{Tr}(\mathscr{X}_g \mathscr{X}_{\sigma_1})\,\mathrm{Tr}(\mathscr{X}_g \mathscr{X}_{\sigma_2})\,\mathrm{Tr}(\mathscr{X}_h \mathscr{X}_{\tau_1})\,\mathrm{Tr}(\mathscr{X}_h \mathscr{X}_{\tau_2}),\end{aligned} \tag{A.6}$$

where Wg is the Weingarten function[202, 203] and g, h are S_2 group elements

$$\mathsf{Wg}(g^{-1}h, d^2) = \begin{cases} \frac{1}{d^4-1} & g^{-1}h = \shortparallel \\ -\frac{1}{d^2(d^4-1)} & g^{-1}h = \times \end{cases}. \tag{A.7}$$

The cycle counting function $\mathrm{Tr}(\mathscr{X}_g \mathscr{X}_h)$ follows

$$\mathrm{Tr}(\mathscr{X}_g \mathscr{X}_h) = \begin{cases} d^2 & gh = \shortparallel \\ d & gh = \mathsf{X} \end{cases} . \tag{A.8}$$

Substituting Eq. (A.7) and Eq. (A.8) into Eq. (A.6), we can evaluate $\mathbb{E}_{U_{ij} \in \mathrm{Haar}} W_{U_{ij}}[\boldsymbol{\sigma}, \boldsymbol{\tau}]$ for all configurations of $\boldsymbol{\sigma}, \boldsymbol{\tau}$. In terms of Ising variables (following the identification $\shortparallel \Leftrightarrow \uparrow$ and $\mathsf{X} \Leftrightarrow \downarrow$), we can summarize the result as the following matrix in the Ising basis $\boldsymbol{\sigma}, \boldsymbol{\tau} = \uparrow\uparrow, \uparrow\downarrow, \downarrow\uparrow, \downarrow\downarrow$

$$\mathbb{E}_{U_{ij} \in \mathrm{Haar}} \hat{W}_{U_{ij}} = \begin{bmatrix} d^4 & d^3 & d^3 & d^2 \\ d^3 & \frac{2d^4}{d^2+1} & \frac{2d^4}{d^2+1} & d^3 \\ d^3 & \frac{2d^4}{d^2+1} & \frac{2d^4}{d^2+1} & d^3 \\ d^2 & d^3 & d^3 & d^4 \end{bmatrix} , \tag{A.9}$$

which is also the matrix representation of the (ensemble averaged) EF operator $\hat{W}_{U_{ij}}$. The matrix can as well be written in terms of Pauli operators as

$$\mathbb{E}_{U_{ij} \in \mathrm{Haar}} \hat{W}_{U_{ij}} = d^2(d + X_i)(d + X_j) - \frac{d^2(d^2-1)}{2(d^2+1)}(1 - Z_i Z_j)(d^2 - X_i X_j), \tag{A.10}$$

as claimed in Eq. (2.13). For simplicity, we have omitted $\mathbb{E}_{U_{ij} \in \mathrm{Haar}}$ notation in Eq. (2.13), with the understanding that the EF for an ensemble of unitaries is implicitly averaged.

A.3 Relation between state and unitary entanglement features

Here we prove Eq. (2.19). Consider a many-body state (multi-qudit) state $|\Psi\rangle$ and an unitary operator U_t in the same Hilbert space. Suppose that $|\Psi'\rangle = U_t |\Psi\rangle$, our goal is to derive the time evolution of the corresponding EF state. In general, this is not tractable since the unitary operator U_t contains many non-universal features that are specific to the choice of local basis.

Such features may affect the entanglement of the final state but such features are not captured in EF formalism. To keep track of universal features, we instead consider an ensemble of unitary operator U,

$$\mathscr{E}_U = \left\{ V^\dagger U V \middle| V = \bigotimes_{i=1}^{L} V_i, V_i \in \text{Haar} \right\}, \tag{A.11}$$

where each V_i independently follows Haar random unitary distribution on the ith qudit. Our goal is to compute $\mathbb{E}_{U'\in\mathscr{E}_U} W_{U'|\Psi\rangle}[\boldsymbol{\sigma}]$,

$$\begin{aligned}
\underset{U'\in\mathscr{E}_U}{\mathbb{E}} W_{U'|\Psi\rangle}[\boldsymbol{\sigma}] &= \underset{U'\in\mathscr{E}_U}{\mathbb{E}} \operatorname{Tr}[\mathscr{X}_{\boldsymbol{\sigma}}(U'|\Psi\rangle\langle\Psi|U'^\dagger)^{\otimes 2}] \\
&= \underset{V\in\text{Haar}}{\mathbb{E}} \operatorname{Tr}[\mathscr{X}_{\boldsymbol{\sigma}}(V^\dagger U V|\Psi\rangle\langle\Psi|V^\dagger U^\dagger V)^{\otimes 2}] \\
&= \underset{V\in\text{Haar}}{\mathbb{E}} \langle\Psi|^{\otimes 2} V^{\dagger\otimes 2} U^{\dagger\otimes 2} V^{\otimes 2} \mathscr{X}_{\boldsymbol{\sigma}} V^{\dagger\otimes 2} U^{\otimes 2} V^{\otimes 2} |\Psi\rangle^{\otimes 2} \\
&= \underset{V\in\text{Haar}}{\mathbb{E}} \langle\Psi|^{\otimes 2} V^{\dagger\otimes 2} U^{\dagger\otimes 2} \mathscr{X}_{\boldsymbol{\sigma}} U^{\otimes 2} V^{\otimes 2} |\Psi\rangle^{\otimes 2} \\
&= \sum_{\boldsymbol{\tau},\boldsymbol{\tau}'} \operatorname{Tr}(\mathscr{X}_{\boldsymbol{\tau}}|\Psi\rangle\langle\Psi|^{\otimes 2}) \operatorname{Tr}(\mathscr{X}_{\boldsymbol{\tau}'} U^\dagger(t)^{\otimes 2} \mathscr{X}_{\boldsymbol{\sigma}} U_t^{\otimes 2}) \prod_i \mathsf{Wg}(\tau_i'^{-1}\tau_i, d) \\
&= \sum_{\boldsymbol{\tau},\boldsymbol{\tau}'} W_{|\Psi\rangle}[\boldsymbol{\tau}] W_U[\boldsymbol{\sigma},\boldsymbol{\tau}'] \prod_i \mathsf{Wg}(\tau_i'^{-1}\tau_i, d),
\end{aligned} \tag{A.12}$$

where Wg denotes the Weingarten function[202, 203] originated from the Haar ensemble average of $V^{\dagger\otimes 2}V^{\otimes 2}$, and $\boldsymbol{\tau}, \boldsymbol{\tau}'$ are new set of Ising variables. The derivation in Eq. (A.12) can also be diagrammatically represented as Fig. A.1.

By definition, the Weingarten function, when viewed as a matrix indexed by $\boldsymbol{\tau}$ and $\boldsymbol{\tau}'$, is the inverse of the Gram matrix $\operatorname{Tr}\mathscr{X}_{\boldsymbol{\tau}}\mathscr{X}_{\boldsymbol{\tau}'} = \langle\boldsymbol{\tau}'|\hat{W}_{\mathbb{1}}|\boldsymbol{\tau}\rangle$, which is simply the matrix representation of the EF operator $\hat{W}_{\mathbb{1}}$ of the identity operator. So the Weingarten function is given by the matrix element of $\hat{W}_{\mathbb{1}}^{-1}$ as

$$\prod_i \mathsf{Wg}(\tau_i'^{-1}\tau_i, d) = \langle\boldsymbol{\tau}'|\hat{W}_{\mathbb{1}}^{-1}|\boldsymbol{\tau}\rangle. \tag{A.13}$$

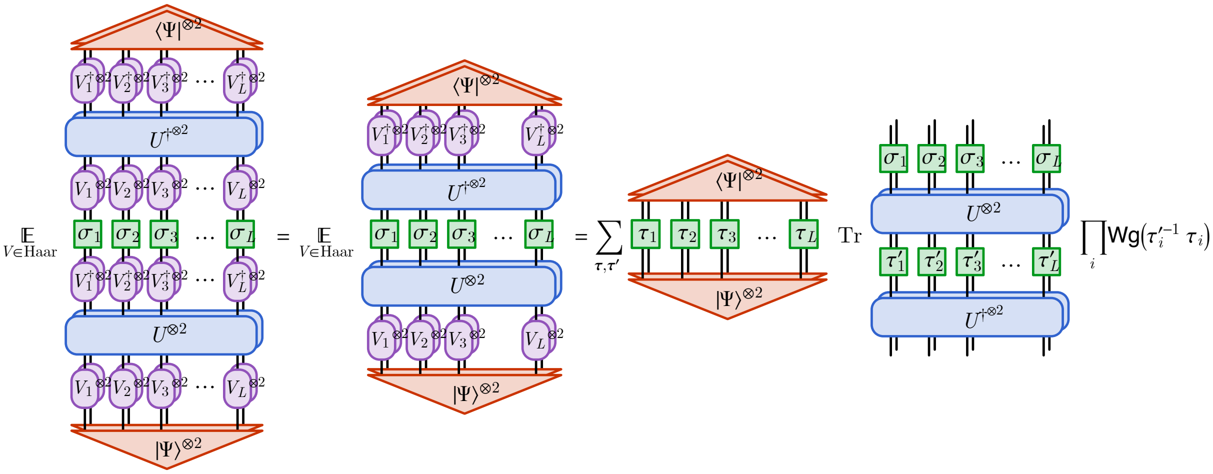

Figure A.1. Diagrammatic proof of Eq. (2.19)

Therefore, in operator form, we have

$$\begin{aligned}\mathbb{E}_{U'\in\mathscr{E}_U}|W_{U'\Psi}\rangle &= \sum_{\boldsymbol{\sigma}} W_{U'|\Psi\rangle}[\boldsymbol{\sigma}]|\boldsymbol{\sigma}\rangle \\ &= \sum_{\boldsymbol{\sigma},\boldsymbol{\tau}',\boldsymbol{\tau}} \big(|\boldsymbol{\sigma}\rangle W_U[\boldsymbol{\sigma},\boldsymbol{\tau}']\langle\boldsymbol{\tau}'|\big)\hat{W}_{\mathbb{1}}^{-1}\big(W_{|\Psi\rangle}[\boldsymbol{\tau}]|\boldsymbol{\tau}\rangle\big) \\ &= \hat{W}_U\hat{W}_{\mathbb{1}}^{-1}|W_\Psi\rangle,\end{aligned} \tag{A.14}$$

as stated in Eq. (2.19).

A.4 Spectral properties of entanglement Hamiltonian

Let us start with the most general form of the EF Hamiltonian $\hat{H}_{\text{EF}}$ given in Eq. (2.32) and investigate its spectral properties.

$$\hat{H}_{\text{EF}} = \sum_{i,j}\hat{H}_{ij}, \qquad \hat{H}_{ij} = g_{ij}\frac{1-Z_iZ_j}{2}e^{-\beta_{ij}X_iX_j-\delta(X_i+X_j)}, \tag{A.15}$$

with $\coth\delta = d$. Our first goal is to show that $\hat{H}_{\mathrm{EF}}$ is positive semi-definite. The trick is to first deform $\hat{H}_{\mathrm{EF}}$ to a Hermitian version $\hat{H}'_{\mathrm{EF}}$, given by

$$\hat{H}'_{\mathrm{EF}} = \hat{W}_{\mathbb{1}}^{-1/2}\hat{H}_{\mathrm{EF}}\hat{W}_{\mathbb{1}}^{1/2}. \tag{A.16}$$

Because $\hat{H}_{\mathrm{EF}}$ and $\hat{H}'_{\mathrm{EF}}$ are related by similarity transformation, they share the same set of eigenvalues. So the positivity of the original EF Hamiltonian $\hat{H}_{\mathrm{EF}}$ is equivalent to the positivity of the transformed Hermitian version $\hat{H}'_{\mathrm{EF}}$. The later turns out to be easier to prove. By the way, to see that $\hat{H}'_{\mathrm{EF}}$ is Hermitian (or real symmetric to be more precise), we use $\hat{W}_{\mathbb{1}}^{\mathsf{T}} = \hat{W}_{\mathbb{1}}$ and Eq. (2.35) that $\hat{W}_{\mathbb{1}}\hat{H}_{\mathrm{EF}}^{\mathsf{T}} = \hat{H}_{\mathrm{EF}}\hat{W}_{\mathbb{1}}$, then

$$\begin{aligned}\hat{H}'^{\mathsf{T}}_{\mathrm{EF}} &= \hat{W}_{\mathbb{1}}^{1/2}\hat{H}_{\mathrm{EF}}^{\mathsf{T}}\hat{W}_{\mathbb{1}}^{-1/2} = \hat{W}_{\mathbb{1}}^{-1/2}(\hat{W}_{\mathbb{1}}\hat{H}_{\mathrm{EF}}^{\mathsf{T}})\hat{W}_{\mathbb{1}}^{-1/2} = \hat{W}_{\mathbb{1}}^{-1/2}(\hat{H}_{\mathrm{EF}}\hat{W}_{\mathbb{1}})\hat{W}_{\mathbb{1}}^{-1/2} = \hat{W}_{\mathbb{1}}^{-1/2}\hat{H}_{\mathrm{EF}}\hat{W}_{\mathbb{1}}^{1/2}\\ &= \hat{H}'_{\mathrm{EF}},\end{aligned} \tag{A.17}$$

meaning that $\hat{H}'_{\mathrm{EF}}$ is transpose symmetric. Moreover $\hat{H}'_{\mathrm{EF}}$ is real by definition, so $\hat{H}'_{\mathrm{EF}}$ is real and symmetric and therefore Hermitian. As a real symmetric operator, $\hat{H}'_{\mathrm{EF}}$ admits the following spectral decomposition

$$\hat{H}'_{\mathrm{EF}} = \sum_a |V_a\rangle\lambda_a\langle V_a|, \tag{A.18}$$

with $|V_a\rangle = \langle V_a|^{\mathsf{T}}$ being the eigenvector corresponding to the eigenvalue λ_a. If we can show that the expectation value $\langle V|\hat{H}'_{\mathrm{EF}}|V\rangle \geq 0$ is non-negative on *any* state $|V\rangle$ in the EF Hilbert space (including the eigenstates $|V_a\rangle$), we will be able to prove that all eigenvalues $\lambda_a = \langle V_a|\hat{H}'_{\mathrm{EF}}|V_a\rangle \geq 0$ are non-negative, hence $\hat{H}'_{\mathrm{EF}}$ will be positive semi-definite.

We can show $\langle V|\hat{H}'_{\mathrm{EF}}|V\rangle \geq 0$ by finding the Cholesky decomposition for each terms in $\hat{H}'_{\mathrm{EF}}$. A useful trick is to note that $d(d+X_i) = e^{\delta X_i}/(\tanh\delta\sinh\delta)$ given $d = \coth\delta$, so $\hat{W}_{\mathbb{1}}$ can be rewritten as

$$\hat{W}_{\mathbb{1}} = \prod_{i=1}^{L} d(d+X_i) = \prod_{i=1}^{L} \frac{e^{\delta X_i}}{\tanh\delta \sinh\delta} = \frac{1}{(\tanh\delta\sinh\delta)^L} \prod_{i=1}^{L} e^{\delta X_i}, \tag{A.19}$$

such that any $\hat{W}_{\mathbb{1}}^{\alpha}$ can be simply calculated,

$$\hat{W}_{\mathbb{1}}^{\alpha} = (\tanh\delta\sinh\delta)^{-\alpha L} \prod_{i=1}^{L} e^{\alpha\delta X_i}. \tag{A.20}$$

With this, and substitute Eq. (A.15) in Eq. (A.16), we can show that

$$\begin{aligned}
\hat{H}'_{\mathrm{EF}} &= \sum_{i,j} \hat{H}'_{ij}, \\
\hat{H}'_{ij} &= \hat{W}_{\mathbb{1}}^{-1/2} \hat{H}_{ij} \hat{W}_{\mathbb{1}}^{1/2} \\
&= \prod_{i=1}^{L} e^{-\frac{\delta}{2}X_i} \hat{H}_{ij} \prod_{i=1}^{L} e^{\frac{\delta}{2}X_i} \\
&= e^{-\frac{\delta}{2}(X_i+X_j)} \hat{H}_{ij} e^{\frac{\delta}{2}(X_i+X_j)} \\
&= g_{ij} e^{-\frac{\delta}{2}(X_i+X_j)} \frac{1-Z_iZ_j}{2} e^{-\beta_{ij}X_iX_j} e^{-\frac{\delta}{2}(X_i+X_j)} \\
&= g_{ij} e^{-\frac{\delta}{2}(X_i+X_j)} \frac{1-Z_iZ_j}{2} e^{-\beta_{ij}X_iX_j} \frac{1-Z_iZ_j}{2} e^{-\frac{\delta}{2}(X_i+X_j)}.
\end{aligned} \tag{A.21}$$

In the last step, we use the fact that $\frac{1-Z_iZ_j}{2}$ is a projection operator, so $(\frac{1-Z_iZ_j}{2})^2 = \frac{1-Z_iZ_j}{2}$. Also $\frac{1-Z_iZ_j}{2}$ and $e^{-\beta_{ij}X_iX_j}$ commute with each other, so we are free to move $e^{-\beta_{ij}X_iX_j}$ through $\frac{1-Z_iZ_j}{2}$. The final form of $\hat{H}'_{ij}$ admits the following Cholesky decomposition explicitly

$$\hat{H}'_{ij} = \hat{A}_{ij}^{\intercal} \hat{A}_{ij}, \qquad \hat{A}_{ij} = g_{ij}^{1/2} e^{-\frac{\beta_{ij}}{2}X_iX_j} \frac{1-Z_iZ_j}{2} e^{-\frac{\delta}{2}(X_i+X_j)}. \tag{A.22}$$

For any state $|V\rangle$ in EF Hilbert space, the expectation value $\langle V|\hat{H}'_{ij}|V\rangle = \langle V|\hat{A}_{ij}^{\intercal}\hat{A}_{ij}|V\rangle \geq 0$ is non-negative, therefore $\hat{H}'_{ij}$ is positive semi-definite. In consequence, the transformed EF Hamiltonian $\hat{H}'_{\mathrm{EF}} = \sum_{i,j} \hat{H}'_{ij}$ is also positive semi-definite, as it is the sum of positive semi-definite terms $\hat{H}'_{ij}$. Recall that the similarity transformation does not affect the eigenvalues, so

$\hat{H}_{\mathrm{EF}} = \hat{W}_{\mathbb{1}}^{1/2} \hat{H}'_{\mathrm{EF}} \hat{W}_{\mathbb{1}}^{-1/2}$ is also positive semi-definite.

We can further show that $\hat{H}_{\mathrm{EF}}$ always has two zero modes: one is even under $\mathbb{Z}_2$ Ising symmetry, and the other is odd. Using the left-null-state property $\langle \Uparrow | \hat{H}_{\mathrm{EF}} = 0$ given in Eq. (2.34), it is ensured that $\langle \Uparrow |$ is an left-eigenstate of $\hat{H}_{\mathrm{EF}}$ with zero eigenvalue. Since $\hat{H}_{\mathrm{EF}}$ is $\mathbb{Z}_2$ symmetric, the $\mathbb{Z}_2$ related state $\langle \Downarrow | = \langle \Uparrow | \prod_i X_i$ is also a left zero mode. So by explicit construction, we have shown that $\hat{H}_{\mathrm{EF}}$ has at least two zero eigenvalues. The left zero mode subspace is spanned by $\langle \Uparrow |$ and $\langle \Downarrow |$. Using the relation between left- and right-eigenstate $|R_a\rangle \propto (\langle L_a | \hat{W}_{\mathbb{1}})^{\intercal}$, the corresponding right zero mode subspace is spanned by $\hat{W}_{\mathbb{1}} | \Uparrow\rangle$ and $\hat{W}_{\mathbb{1}} | \Downarrow\rangle$.

Since we are most interested about the EF of pure states, we should focus on the $\mathbb{Z}_2$ even state in the zero mode subspace. In that regard, the left and right zero modes in the $\mathbb{Z}_2$ even sector are given by

$$\begin{aligned}
\langle L_0| &= \frac{\langle \Uparrow | + \langle \Downarrow |}{2}, \\
|R_0\rangle &\propto \hat{W}_{\mathbb{1}} \frac{| \Uparrow\rangle + | \Downarrow\rangle}{2} \\
&= \frac{1}{2}\left(\prod_{i=1}^{L} d(d+X_i)\right)(| \Uparrow\rangle + | \Downarrow\rangle) \\
&= \frac{1}{2} d^{3L/2}\left(\prod_{i=1}^{L} (e^{\eta} + e^{-\eta} X_i)\right)(| \Uparrow\rangle + | \Downarrow\rangle) \qquad (\eta \equiv \tfrac{1}{2}\log d) \\
&= \frac{1}{2} d^{3L/2} \sum_{\boldsymbol{\sigma}} \left(\prod_{i=1}^{L} e^{\eta\sigma_i} |\boldsymbol{\sigma}\rangle + \prod_{i=1}^{L} e^{-\eta\sigma_i} |\boldsymbol{\sigma}\rangle\right) \\
&= d^{3L/2} \sum_{\boldsymbol{\sigma}} \cosh\left(\eta \sum_{i=1}^{L} \sigma_i\right) |\boldsymbol{\sigma}\rangle.
\end{aligned} \tag{A.23}$$

The normalization of $|R_0\rangle$ is determined by the condition $\langle L_0 | R_0\rangle = 1$, such that

$$|R_0\rangle = \sum_{\boldsymbol{\sigma}} \frac{\cosh\left(\eta \sum_{i=1}^{L} \sigma_i\right)}{\cosh(\eta L)} |\boldsymbol{\sigma}\rangle = |W_{\mathrm{Page}}\rangle. \tag{A.24}$$

In summary, we have shown that in the $\mathbb{Z}_2$ even sector, the EF Hamiltonian $\hat{H}_{\mathrm{EF}}$ has at least one zero eigenvalue $\lambda_0 = 0$, whose left- and right-eigenstates are given by

$$\langle L_0| = \frac{\langle \Uparrow | + \langle \Downarrow |}{2}, \qquad |R_0\rangle = |W_{\text{Page}}\rangle, \tag{A.25}$$

as claimed in Eq. (2.41).

A.5 Derivation of the dispersion relation for two-domain-wall ansatz

Here, we show the derivation of Eq. (2.52). Our goal here is to obtain the analytical expression of excited state energy, namely dispersion relation, $\omega(k)$. Note that the left and right eigenstates are *not* simply each other's conjugate transpose due to the non-hermitian nature of EF Hamiltonian (Eq. (2.32)). For simplicity, we focus on the excitation of left eigenstates and construct the corresponding right eigenstate with $|R\rangle = (\langle L|\hat{W}_{\mathbb{1}})^{\intercal}$. From the discussion in Sec. 3.3, the universal left ground state for any parameters g_{ij}, β is the linear combination of all spin-up and spin-down state,

$$\langle L_0| = \frac{\langle \Uparrow | + \langle \Downarrow |}{2}. \tag{A.26}$$

Based on our ED result in Fig. 2.5, the low energy left excited state mainly consists of two-domain-wall states. The generic form of two-domain-wall state can be expressed as

$$\langle k| \equiv C_k \sum_{n,a} \langle k_n, a| \equiv C_k \sum_{n,a} e^{ikn} \phi^*(a) \langle \Uparrow | \prod_{i=n}^{n+a} X_i \tag{A.27}$$

where C_k is the normalization constant and $\langle k_n, a|$ represents the two-domain-wall state ranging from n to $n+a$.

We start by deriving the normalization constant.

$$\langle k|k\rangle = |C_k|^2 \sum_{n,m,a,b} e^{ik(n-m)} \phi^*(a)\phi(b) \langle \Uparrow | \prod_{i=n}^{n+a} X_i \hat{W}_{\mathbb{1}} \prod_{i=m}^{m+b} X_i | \Uparrow\rangle = 1. \tag{A.28}$$

The next step is to evaluate $\langle \Uparrow | \prod_{i=n}^{n+a} X_i \hat{W}_{\mathbb{1}} \prod_{j=m}^{m+b} X_j | \Uparrow \rangle$. The physical meaning is the transition amplitude between two Bethe string states with evolution as $\hat{W}_{\mathbb{1}}$. There are two possibilities for each site. When both Bethe strings have/do not have excitation at site i, the answer would be $\langle \Uparrow | (\hat{W}_{\mathbb{1}})_i | \Uparrow \rangle = d^2$. When either Bethe string has excitation on site i, the result becomes $\langle \Uparrow | X_i (\hat{W}_{\mathbb{1}})_i | \Uparrow \rangle = d$. To evaluate this quantity, we perform perturbative expansion as $1/d$ series. To obtain analytical expression of $|C_k|^2$, we also approximate $\phi(a)$ as plane wave $\sim e^{-ika/2}$. Physical intuition is that we assume these domain walls have little interaction with each other and thus they can move through each other almost freely. Consequently, plane wave solution is assumed and $a/2$ represents the center location of domain wall. Let's start evaluating the normalization constant up to the order of $1/d^2$,

$$\begin{aligned}
\langle \Uparrow | \prod_{i=n}^{n+a} X_i \hat{W}_{\mathbb{1}} \prod_{j=m}^{m+b} X_j | \Uparrow \rangle &= \delta_{n,m}\delta_{a,b} d^{2N} \\
&+ (\delta_{n,m}\delta_{a,b+1} + \delta_{n,m}\delta_{a,b-1} + \delta_{n,m+1}\delta_{a,b-1} + \delta_{n,m-1}\delta_{a,b+1}) d^{2N-1} \\
&+ (\delta_{n,m}\delta_{a,b+2} + \delta_{n,m}\delta_{a,b-2} + \delta_{n,m-2}\delta_{a,b+2} + \delta_{n,m+2}\delta_{a,b-2} \\
&+ \delta_{n,m+1}\delta_{a,b} + \delta_{n,m+1}\delta_{a,b-2} + \delta_{n,m-1}\delta_{a,b} + \delta_{n,m-1}\delta_{a,b+2}) d^{2N-2} \\
&+ \mathscr{O}(d^{2N-3})
\end{aligned} \tag{A.29}$$

For $b = 0, 1$, we would have different terms,

$$\begin{aligned}
\langle \Uparrow | \prod_{i=n}^{n+a} X_i \hat{W}_{\mathbb{1}} X_m | \Uparrow \rangle = \delta_{n,m}\delta_{a,0} d^{2N} &+ (\delta_{n,m}\delta_{a,1} + \delta_{n,m-1}\delta_{a,1}) d^{2N-1} \\
&+ (\delta_{n,m}\delta_{a,2} + \delta_{n,m-2}\delta_{a,2} + \delta_{n,m+1}\delta_{a,0} + \delta_{n,m-1}\delta_{a,0} + \delta_{n,m-1}\delta_{a,2}) d^{2N-2} \\
&+ \mathscr{O}(d^{2N-3})
\end{aligned} \tag{A.30}$$

$$
\begin{aligned}
&\langle \Uparrow | \prod_{i=n}^{n+a} X_i \hat{W}_{\mathbb{1}} X_m X_{m+1} | \Uparrow \rangle = \delta_{n,m}\delta_{a,1} d^{2N} + (\delta_{n,m}\delta_{a,2} + \delta_{n,m}\delta_{a,0} + \delta_{n,m+1}\delta_{a,0} + \delta_{n,m-1}\delta_{a,2}) d^{2N-1} \\
&+ (\delta_{n,m}\delta_{a,3} + \delta_{n,m-2}\delta_{a,3} + \delta_{n,m+1}\delta_{a,1} + \delta_{n,m-1}\delta_{a,1} + \delta_{n,m-1}\delta_{a,3}) d^{2N-2} + \mathscr{O}(d^{2N-3})
\end{aligned}
\tag{A.31}
$$

Put them back to Eq. (A.28) and we can obtain

$$
\begin{aligned}
&|C_k|^2 d^{2N} N^2 \{ \frac{N-2}{N} [1 + \frac{4}{d}\cos\frac{k}{2} + \frac{1}{d^2}(2 + 6\cos k)] + \frac{1}{N}[1 + \frac{2}{d}\cos\frac{k}{2} + \frac{1}{d^2}(1 + 4\cos k)] \\
&+ \frac{1}{N}[1 + \frac{4}{d}\cos\frac{k}{2} + \frac{1}{d^2}(1 + 4\cos k)] + \mathscr{O}(d^{-3}) \} = 1
\end{aligned}
\tag{A.32}
$$

To simplify the whole calculation, the thermodynamics limit is taken $N \to \infty$. The main effect of thermodynamic limit is that the contribution from short two domain wall states (e.g. single-site or two-site excitations) is fully suppressed. Thus, up to $\mathscr{O}(\frac{1}{d^2})$, we have

$$
|C_k|^2 d^{2N} N^2 [1 + \frac{4}{d}\cos\frac{k}{2} + \frac{1}{d^2}(2 + 6\cos k)] = 1 \tag{A.33}
$$

Now, we are ready to evaluate the energy expectation value of our two-domain-wall state, $\langle k | H_{EF} | k \rangle$. For simplicity, we assume $g_{ij} = 1, \beta_{ij} = \beta$ and reorganize the EF Hamiltonian

$$
\begin{aligned}
\hat{H}_{\mathrm{EF}} &= \sum_{i,j} \frac{1 - Z_i Z_j}{2} e^{-\beta X_i X_j - \delta(X_i + X_j)} \\
&= \sum_{i,j} \frac{1 - Z_i Z_j}{2} \frac{d^2}{d^2 - 1} [\cosh\beta - \sinh\beta X_i X_j][1 - \frac{1}{d}(X_i + X_j) + \frac{1}{d^2} X_i X_j] \\
&= \sum_{i,j} \frac{1 - Z_i Z_j}{2} \frac{d^2}{d^2 - 1} [\cosh\beta - \frac{\sinh\beta}{d^2} - \frac{1}{d}(\cosh\beta - \sinh\beta)(X_i + X_j) + (\frac{\cosh\beta}{d^2} - \sinh\beta) X_i X_j] \\
&\equiv \sum_{i} \frac{1 - Z_i Z_{i+1}}{2} \left[a(\beta, d) + b(\beta, d)(X_i + X_{i+1}) + c(\beta, d) X_i X_{i+1} \right]
\end{aligned}
\tag{A.34}
$$

where

$$\begin{aligned}
a(\beta,d) &= \frac{d^2}{d^2-1}(\cosh\beta - \frac{\sinh\beta}{d^2}) = \cosh\beta + \frac{\cosh\beta-\sinh\beta}{d^2} + \mathscr{O}(\frac{1}{d^4}) \\
b(\beta,d) &= -\frac{d}{d^2-1}(\cosh\beta - \sinh\beta) = -\frac{1}{d}(\cosh\beta-\sinh\beta) + \mathscr{O}(\frac{1}{d^3}) \\
c(\beta,d) &= \frac{d^2}{d^2-1}(\frac{\cosh\beta}{d^2} - \sinh\beta) = \frac{\cosh\beta-\sinh\beta}{d^2} - \sinh\beta + \mathscr{O}(\frac{1}{d^4}).
\end{aligned} \tag{A.35}$$

The first term in $\langle k|H_{EF}|k\rangle$ is

$$\begin{aligned}
&|C_k|^2 a(\beta,d)\sum_{n,m,a,b} e^{ik(n-m)}e^{ik(a-b)/2}\langle\Uparrow|\prod_{i=n}^{n+a}X_i\sum_l\frac{1-Z_lZ_{l+1}}{2}\hat{W}_{\mathbb{1}}\prod_{j=m}^{m+b}X_j|\Uparrow\rangle \\
&= 2a(\beta,d)|C_k|^2\sum_{n,m,a,b} e^{ik(n-m)}e^{ik(a-b)/2}\langle\Uparrow|\prod_{i=n}^{n+a}X_i\hat{W}_{\mathbb{1}}\prod_{j=m}^{m+b}X_j|\Uparrow\rangle = 2a(\beta,d)
\end{aligned} \tag{A.36}$$

As for the second term, since $b(\beta,d)$ already contains $1/d$ power, we just compute the terms up to $1/d$ order and the result is

$$\begin{aligned}
&|C_k|^2 b(\beta,d)\sum_{n,m,a,b} e^{ik(n-m)}e^{ik(a-b)/2}\langle\Uparrow|\prod_{i=n}^{n+a}X_i\sum_l\frac{1-Z_lZ_{l+1}}{2}(X_l+X_{l+1})\hat{W}_{\mathbb{1}}\prod_{j=m}^{m+b}X_j|\Uparrow\rangle \\
&= |C_k|^2 b(\beta,d)\sum_{n,m,a,b} e^{ik(n-m)}e^{ik(a-b)/2} \\
&\times[h(n-1,m,a+1,b)+h(n+1,m,a-1,b)+h(n,m,a+1,b)+h(n,m,a-1,b)]
\end{aligned} \tag{A.37}$$

where

$$h(n,m,a,b) = \langle\Uparrow|\prod_{i=n}^{n+a}X_i\hat{W}_{\mathbb{1}}\prod_{j=m}^{m+b}X_j|\Uparrow\rangle. \tag{A.38}$$

For each $h(n,m,a,b)$, the boundary terms would have different result. For example, the results of $h(n-1,m,a+1,b)$ are as follows

$$\begin{aligned}
&h(n-1,m,a+1,0) = (\delta_{n,m+1}\delta_{a,0}+\delta_{n,m}\delta_{a,0})d^{2N-1}+\mathscr{O}(d^{2N-2})\\
&h(n-1,m,a+1,1) = \delta_{n,m+1}\delta_{a,0}d^{2N}+(\delta_{n,m+1}\delta_{a,1}+\delta_{n,m}\delta_{a,1})d^{2N-1}+\mathscr{O}(d^{2N-2})\\
&h(n-1,m,a+1,2) = \delta_{n,m+1}\delta_{a,1}d^{2N}\\
&+(\delta_{n,m+1}\delta_{a,2}+\delta_{n,m+1}\delta_{a,0}+\delta_{n,m+2}\delta_{a,0}+\delta_{n,m}\delta_{a,2})d^{2N-1}+\mathscr{O}(d^{2N-2})\\
&h(n-1,m,a+1,b\neq 0,1,2) = \delta_{n,m+1}\delta_{a,b-1}d^{2N}\\
&+(\delta_{n,m+1}\delta_{a,b}+\delta_{n,m+1}\delta_{a,b-2}+\delta_{n,m+2}\delta_{a,b-2}+\delta_{n,m}\delta_{a,b})d^{2N-1}+\mathscr{O}(d^{2N-2}).
\end{aligned} \tag{A.39}$$

Since the thermodynamics limit would be taken ($N\to\infty$), the "boundary effect" from short two-domain-wall states would be suppressed. Consequently, we only keep the last term in our calculation. Combine these four terms and compute the sum with thermodynamic limit,

$$\begin{aligned}
&|C_k|^2 b(\beta,d)d^{2N}N^2[4\cos\frac{k}{2}+\frac{8}{d}(1+\cos k)]+\mathscr{O}(\frac{1}{d^2})\\
&=b(\beta,d)[4\cos\frac{k}{2}-\frac{16}{d}\cos^2\frac{k}{2}+\frac{4}{d}(2+2\cos k)]+\mathscr{O}(\frac{1}{d^2})
\end{aligned} \tag{A.40}$$

For the third term, the following quantity is computed

$$|C_k|^2 c(\beta,d)\sum_{n,m,a,b} e^{ik(n-m)}e^{ik(a-b)/2}\langle\Uparrow|\prod_{i=n}^{n+a}X_i\sum_{l}\frac{1-Z_lZ_{l+1}}{2}X_lX_{l+1}\hat{W}_I\prod_{j=m}^{m+b}X_j|\Uparrow\rangle. \tag{A.41}$$

The EF Hamiltonian would give extra X_iX_{i+1} term. In most two-domain-wall states (length > 1), the two-domain-wall structure would destroyed. However, for single site excitation, this X_iX_{i+1} term would only shift the position of excitation with one site. Due to the suppression of thermodynamic limit, we would also drop this term. Eventually, we obtain

$$\begin{aligned}
&c(\beta,d)\big[\frac{4}{d}\cos\frac{k}{2}+\frac{1}{d^2}(8+8\cos k)\big](1-\frac{4}{d}\cos\frac{k}{2})+\mathscr{O}(\frac{1}{d^3})=\\
&c(\beta,d)\big[\frac{4}{d}\cos\frac{k}{2}+\frac{1}{d^2}(8+8\cos k)-\frac{16}{d^2}\cos^2\frac{k}{2}\big]+\mathscr{O}(\frac{1}{d^3}).
\end{aligned} \tag{A.42}$$

Combining Eq. (A.36), Eq. (A.40) and Eq. (A.42) and keeping terms up to $\mathscr{O}(\frac{1}{d^3})$, $\langle k|H_{EF}|k\rangle$ is

$$\begin{aligned}
&\langle k|H_{EF}|k\rangle = 2[\cosh\beta + \frac{\cosh\beta - \sinh\beta}{d^2}] \\
&-\frac{1}{d}(\cosh\beta - \sinh\beta)[4\cos\frac{k}{2} - \frac{16}{d}\cos^2\frac{k}{2} + \frac{4}{d}(2+2\cos k)] \\
&-\sinh\beta\,[\frac{4}{d}\cos\frac{k}{2} + \frac{1}{d^2}(8+8\cos k) - \frac{16}{d^2}\cos^2\frac{k}{2}] + \mathscr{O}(\frac{1}{d^3})
\end{aligned} \tag{A.43}$$

A.6 Derivation of the dispersion relation for single-site excitation ansatz

This appendix is similar with the calculation in Appendix A.5. The only difference is the ansatz state we use. The single-site excitation ansatz is defined as

$$\langle k| = C_k\langle\Uparrow|\sum_n X_n e^{ikn}, |k\rangle = \hat{W}_{\mathbb{1}}\sum_n X_n e^{-ikn}|\Uparrow\rangle. \tag{A.44}$$

First, we start from the normalization condition $\langle k|k\rangle = 1$,

$$\langle k|k\rangle = 1 = C_k\langle\Uparrow|\sum_{n,m} e^{ik(n-m)}X_n\hat{W}_{\mathbb{1}}X_m|\Uparrow\rangle = C_k[Nd^{2(N-1)}(d^2-1) + N^2\delta_{k,0}d^{2(N-1)}]. \tag{A.45}$$

Following the expression in Eq. (A.46),

$$\hat{H}_{\mathrm{EF}} = \sum_i \frac{1 - Z_iZ_{i+1}}{2}\left[a(\beta,d) + b(\beta,d)(X_i + X_{i+1}) + c(\beta,d)X_iX_{i+1}\right] \tag{A.46}$$

where

$$\begin{aligned}
a(\beta,d) &= \frac{d^2}{d^2-1}(\cosh\beta - \frac{\sinh\beta}{d^2}), \\
b(\beta,d) &= -\frac{d}{d^2-1}(\cosh\beta - \sinh\beta), \\
c(\beta,d) &= \frac{d^2}{d^2-1}(\frac{\cosh\beta}{d^2} - \sinh\beta).
\end{aligned} \tag{A.47}$$

The first term is

$$\begin{aligned}
a(\beta,d)\langle k|\sum_{l}\frac{1-Z_lZ_{l+1}}{2}W_I|k\rangle &= a(\beta,d)C_k\sum_{m,n}e^{ik(n-m)}\langle n|\sum_{l}\frac{1-Z_lZ_{l+1}}{2}\hat{W}_{\mathbb{1}}|m\rangle \\
&= a(\beta,d)C_k\sum_{m,n}e^{ik(n-m)}\langle n|\sum_{l}(\delta_{l,n-1}+\delta_{l,n})\hat{W}_{\mathbb{1}}|m\rangle \\
&= 2a(\beta,d)C_k\sum_{m,n}e^{ik(n-m)}\langle n|\hat{W}_{\mathbb{1}}|m\rangle \\
&= 2a(\beta,d)C_k\sum_{m,n}e^{ik(n-m)}[\delta_{n,m}d^{2N}+(1-\delta_{n,m})d^{2(N-1)}] \\
&= 2a(\beta,d)C_k[Nd^{2(N-1)}(d^2-1)+N^2\delta_{k,0}d^{2(N-1)}] = 2a(\beta,d).
\end{aligned} \tag{A.48}$$

The second term is

$$\begin{aligned}
& b(\beta,d)\langle k|\sum_{l}\frac{1-Z_lZ_{l+1}}{2}(X_l+X_{l+1})W_I|k\rangle \\
&= b(\beta,d)C_k\sum_{m,n}e^{ik(n-m)}\langle n|\sum_{l}\frac{1-Z_lZ_{l+1}(X_l+X_{l+1})}{2}\hat{W}_{\mathbb{1}}|m\rangle \\
&= b(\beta,d)C_k\sum_{m,n}e^{ik(n-m)}\langle n|(X_{n-1}+2X_n+X_{n+1})\hat{W}_{\mathbb{1}}|m\rangle \\
&= b(\beta,d)C_k\sum_{m,n}e^{ik(n-m)}(\langle n,n-1|W_I|m\rangle+\langle n,n+1|\hat{W}_{\mathbb{1}}|m\rangle+2\langle \Uparrow|\hat{W}_{\mathbb{1}}|m\rangle) \\
&= b(\beta,d)C_k\sum_{m,n}e^{ik(n-m)}[d^{2N-3}(1-\delta_{m,n})(1-\delta_{m,n-1})+d^{2N-3}(1-\delta_{m,n})(1-\delta_{m,n+1}) \\
&+d^{2N-1}(\delta_{m,n}+\delta_{m,n-1})+d^{2N-1}(\delta_{m,n}+\delta_{m,n+1})+2d^{2N-1}] \\
&= b(\beta,d)C_k\sum_{m,n}e^{ik(n-m)}[2d^{2N-3}+2d^{2N-1}+(d^{2N-1}-d^{2N-3})(\delta_{m,n-1}+2\delta_{m,n}+\delta_{m,n+1})] \\
&= b(\beta,d)C_k[N^2\delta_{k,0}2d^{2N-3}(d^2+1)+2d^{2N-3}(d^2-1)N(1+\cos k)].
\end{aligned} \tag{A.49}$$

For single-site excitation, we focus on the region which $k \neq 0$. The result would be

$$2b(\beta,d)\frac{1+\cos k}{d}\times C_k[Nd^{2(N-2)}(d^2-1)] = \frac{2b(\beta,d)}{d}(1+\cos k). \tag{A.50}$$

The third term is

$$\begin{aligned}
&c(\beta,d)\langle k|\sum_l \frac{1-Z_lZ_{l+1}}{2}X_lX_{l+1}\hat{W}_{\mathbb{1}}|k\rangle = c(\beta,d)C_k\sum_{m,n}e^{ik(n-m)}\langle n|\sum_l \frac{(1-Z_lZ_{l+1})X_lX_{l+1}}{2}\hat{W}_{\mathbb{1}}|m\rangle\\
&= c(\beta,d)C_k\sum_{m,n}e^{ik(n-m)}\langle n|\sum_l(\delta_{l,n-1}+\delta_{l,n})X_lX_{l+1}\hat{W}_{\mathbb{1}}|m\rangle\\
&= c(\beta,d)C_k\sum_{m,n}e^{ik(n-m)}(\langle n-1|\hat{W}_{\mathbb{1}}|m\rangle+\langle n+1|\hat{W}_{\mathbb{1}}|m\rangle)\\
&= c(\beta,d)C_k\sum_{m,n}e^{ik(n-m)}(2d^{2(N-1)}+(\delta_{m,n-1}+\delta_{m,n+1})(d^{2N}-d^{2(N-1)})\\
&= 2c(\beta,d)C_k[Nd^{2(N-1)}(d^2-1)\cos k+N^2d^{2(N-1)}\delta_{k,0}] = 2c(\beta,d)\cos k
\end{aligned} \tag{A.51}$$

The overall result would be

$$\begin{aligned}
&\langle k|\hat{H}_{EF}|k\rangle = 2a(\beta,d)+\frac{2b(\beta,d)}{d}(1+\cos k)+2c(\beta,d)\cos k\\
&= 2a(\beta,d)+\frac{2b(\beta,d)}{d}+\cos k[2c(\beta,d)+\frac{2b(\beta,d)}{d}]\\
&= \frac{2d^2}{d^2-1}(\cosh\beta-\frac{\sinh\beta}{d^2})-\frac{2}{d^2-1}(\cosh\beta-\sinh\beta)\\
&+\cos k[\frac{2d^2}{d^2-1}(\frac{\cosh\beta}{d^2}-\sinh\beta)-\frac{2}{d^2-1}(\cosh\beta-\sinh\beta)]
\end{aligned} \tag{A.52}$$

A.7 Diagrammatic expansion of entanglement feature Hamiltonian

In this appendix, we derive the EF Hamiltonian for the locally scrambled Hamiltonian dynamics. We start from the definition of the EF for $e^{-\mathrm{i}\varepsilon H}$ following Eq. (2.5),

$$W_{e^{-\mathrm{i}\varepsilon H}}[\boldsymbol{\sigma},\boldsymbol{\tau}] = \mathrm{Tr}\left(\mathscr{X}_{\boldsymbol{\sigma}}(e^{-\mathrm{i}\varepsilon H})^{\otimes 2}\mathscr{X}_{\boldsymbol{\tau}}(e^{\mathrm{i}\varepsilon H})^{\otimes 2}\right) = \mathrm{Tr}\left(\mathscr{X}_{\boldsymbol{\sigma}}e^{-\mathrm{i}\varepsilon\mathbb{H}}\mathscr{X}_{\boldsymbol{\tau}}e^{\mathrm{i}\varepsilon\mathbb{H}}\right), \tag{A.53}$$

where we have introduced $\mathbb{H} = H\otimes\mathbb{1}+\mathbb{1}\otimes H$ to denote the double Hamiltonian. Given the locality of $H=\sum_x H_x$, the double Hamiltonian $\mathbb{H}$ is also a sum of local terms $\mathbb{H}=\sum_x\mathbb{H}_x$ with $\mathbb{H}_x = H_x\otimes\mathbb{1}+\mathbb{1}\otimes H_x$ being the doubled version of H_x. Expanding around $\varepsilon\to 0$ to the order of ε^2, we obtain

$$\begin{aligned}W_{e^{-\mathrm{i}\varepsilon H}}[\boldsymbol{\sigma},\boldsymbol{\tau}] &= \mathrm{Tr}(\mathscr{X}_{\boldsymbol{\sigma}}\mathscr{X}_{\boldsymbol{\tau}}) - \varepsilon^2\,\mathrm{Tr}(\mathscr{X}_{\boldsymbol{\sigma}}\mathscr{X}_{\boldsymbol{\tau}}\mathbb{H}^2 - \mathscr{X}_{\boldsymbol{\sigma}}\mathbb{H}\mathscr{X}_{\boldsymbol{\tau}}\mathbb{H}) + \mathscr{O}(\varepsilon^4),\\ &= W_{\mathbb{1}}[\boldsymbol{\sigma},\boldsymbol{\tau}] - \varepsilon^2\sum_{x,x'}\mathrm{Tr}(\mathscr{X}_{\boldsymbol{\sigma}}\mathscr{X}_{\boldsymbol{\tau}}\mathbb{H}_x\mathbb{H}_{x'} - \mathscr{X}_{\boldsymbol{\sigma}}\mathbb{H}_x\mathscr{X}_{\boldsymbol{\tau}}\mathbb{H}_{x'}) + \mathscr{O}(\varepsilon^4),\\ &= W_{\mathbb{1}}[\boldsymbol{\sigma},\boldsymbol{\tau}] - \varepsilon^2\sum_{x}\mathrm{Tr}(\mathscr{X}_{\boldsymbol{\sigma}}\mathscr{X}_{\boldsymbol{\tau}}\mathbb{H}_x^2 - \mathscr{X}_{\boldsymbol{\sigma}}\mathbb{H}_x\mathscr{X}_{\boldsymbol{\tau}}\mathbb{H}_{x}) + \mathscr{O}(\varepsilon^4)\end{aligned} \tag{A.54}$$

where the first order term in ε vanishes by the cyclic identity of trace, confirming the argument in Sec. 2.3.5 that $W_{U(\varepsilon)}$ will be even in ε. The last equality in Eq. (A.54) relies on the fact that $\mathrm{Tr}(\mathscr{X}_{\boldsymbol{\sigma}}\mathscr{X}_{\boldsymbol{\tau}}\mathbb{H}_x\mathbb{H}_{x'} - \mathscr{X}_{\boldsymbol{\sigma}}\mathbb{H}_x\mathscr{X}_{\boldsymbol{\tau}}\mathbb{H}_{x'}) = 0$ as long as $x\neq x'$. To prove this, we first consider the case when $x = \langle ij\rangle$ and $x' = \langle kl\rangle$ do not overlap,

$$\begin{aligned}
\operatorname{Tr} \mathscr{X}_{\boldsymbol{\sigma}} \mathbb{H}_{\langle ij\rangle} \mathscr{X}_{\boldsymbol{\tau}} \mathbb{H}_{\langle kl\rangle} &= \operatorname{Tr} \mathscr{X}_{\boldsymbol{\sigma}} \mathbb{H}_{\langle ij\rangle} \Big(\mathscr{X}_{\tau_i} \mathscr{X}_{\tau_j} \mathscr{X}_{\tau_k} \mathscr{X}_{\tau_l} \bigotimes_{m\neq i,j,k,l} \mathscr{X}_{\tau_m} \Big) \mathbb{H}_{\langle kl\rangle} \\
&= \operatorname{Tr} \mathscr{X}_{\boldsymbol{\sigma}} \Big(\mathscr{X}_{\tau_k} \mathscr{X}_{\tau_l} \bigotimes_{m\neq i,j,k,l} \mathscr{X}_{\tau_m} \Big) \mathbb{H}_{\langle ij\rangle} \mathbb{H}_{\langle kl\rangle} (\mathscr{X}_{\tau_i} \mathscr{X}_{\tau_j}) \\
&= \operatorname{Tr} (\mathscr{X}_{\tau_i} \mathscr{X}_{\tau_j}) \mathscr{X}_{\boldsymbol{\sigma}} \Big(\mathscr{X}_{\tau_k} \mathscr{X}_{\tau_l} \bigotimes_{m\neq i,j,k,l} \mathscr{X}_{\tau_m} \Big) \mathbb{H}_{\langle ij\rangle} \mathbb{H}_{\langle kl\rangle} \qquad \text{(A.55)} \\
&= \operatorname{Tr} \mathscr{X}_{\boldsymbol{\sigma}} \Big(\mathscr{X}_{\tau_i} \mathscr{X}_{\tau_j} \mathscr{X}_{\tau_k} \mathscr{X}_{\tau_l} \bigotimes_{m\neq i,j,k,l} \mathscr{X}_{\tau_m} \Big) \mathbb{H}_{\langle ij\rangle} \mathbb{H}_{\langle kl\rangle} \\
&= \operatorname{Tr} \mathscr{X}_{\boldsymbol{\sigma}} \mathscr{X}_{\boldsymbol{\tau}} \mathbb{H}_{\langle ij\rangle} \mathbb{H}_{\langle kl\rangle},
\end{aligned}$$

where we have used the fact that $[\mathbb{H}_{\langle ij\rangle}, \mathscr{X}_{\tau_k} \mathscr{X}_{\tau_l}] = 0$ for $i, j \neq k, l$, and $[\mathscr{X}_{\sigma_i}, \mathscr{X}_{\tau_j}] = 0$ for any i, j as the S_2 group is Abelian. We then consider the case when $x = \langle ij\rangle$ and $x' = \langle jk\rangle$ overlaps on a single site j,

$$\begin{aligned}
\operatorname{Tr} \mathscr{X}_{\boldsymbol{\sigma}} \mathbb{H}_{\langle ij\rangle} \mathscr{X}_{\boldsymbol{\tau}} \mathbb{H}_{\langle jk\rangle} &= \operatorname{Tr} \mathscr{X}_{\boldsymbol{\sigma}} \mathbb{H}_{\langle ij\rangle} \Big(\mathscr{X}_{\tau_i} \mathscr{X}_{\tau_j} \mathscr{X}_{\tau_k} \bigotimes_{m\neq i,j,k} \mathscr{X}_{\tau_m} \Big) \mathbb{H}_{\langle jk\rangle} \\
&= \operatorname{Tr} \mathscr{X}_{\boldsymbol{\sigma}} \Big(\mathscr{X}_{\tau_k} \bigotimes_{m\neq i,j,k} \mathscr{X}_{\tau_m} \Big) \mathbb{H}_{\langle ij\rangle} \mathscr{X}_{\tau_j} \mathbb{H}_{\langle jk\rangle} \mathscr{X}_{\tau_i}.
\end{aligned} \qquad \text{(A.56)}$$

At this point, it seems that $\mathscr{X}_{\tau_j}$ is caught between $\mathbb{H}_{\langle ij\rangle}$ and $\mathbb{H}_{\langle jk\rangle}$. The solution is to make use of the property that $\mathbb{H}_{\langle jk\rangle} = \mathscr{X}_{\alpha_j}^{-1} \mathscr{X}_{\alpha_k}^{-1} \mathbb{H}_{\langle jk\rangle} \mathscr{X}_{\alpha_k} \mathscr{X}_{\alpha_j}$ for any $\alpha_j = \alpha_k \in S_2$, due to the permutation symmetry to exchange the two replicas of the double Hamiltonian. Now we choose $\alpha_j = \alpha_k = \tau_j$, such that $\mathscr{X}_{\tau_j}\mathscr{X}_{\alpha_j}^{-1} = 1$, then

$$\begin{aligned}
\operatorname{Tr}\mathscr{X}_{\boldsymbol{\sigma}}\mathbb{H}_{\langle ij\rangle}\mathscr{X}_{\boldsymbol{\tau}}\mathbb{H}_{\langle jk\rangle} &= \operatorname{Tr}\mathscr{X}_{\boldsymbol{\sigma}}\Big(\mathscr{X}_{\tau_k}\bigotimes_{m\neq i,j,k}\mathscr{X}_{\tau_m}\Big)\mathbb{H}_{\langle ij\rangle}\mathscr{X}_{\tau_j}\mathscr{X}_{\alpha_j}^{-1}\mathscr{X}_{\alpha_k}^{-1}\mathbb{H}_{\langle jk\rangle}\mathscr{X}_{\alpha_k}\mathscr{X}_{\alpha_j}\mathscr{X}_{\tau_i}\\
&= \operatorname{Tr}\mathscr{X}_{\boldsymbol{\sigma}}\Big(\mathscr{X}_{\tau_k}\bigotimes_{m\neq i,j,k}\mathscr{X}_{\tau_m}\Big)\mathbb{H}_{\langle ij\rangle}\mathscr{X}_{\alpha_k}^{-1}\mathbb{H}_{\langle jk\rangle}\mathscr{X}_{\alpha_k}\mathscr{X}_{\alpha_j}\mathscr{X}_{\tau_i}\\
&= \operatorname{Tr}\mathscr{X}_{\boldsymbol{\sigma}}\Big(\mathscr{X}_{\tau_i}\mathscr{X}_{\alpha_j}\mathscr{X}_{\alpha_k}\mathscr{X}_{\tau_k}\mathscr{X}_{\alpha_k}^{-1}\bigotimes_{m\neq i,j,k}\mathscr{X}_{\tau_m}\Big)\mathbb{H}_{\langle ij\rangle}\mathbb{H}_{\langle jk\rangle} \qquad \text{(A.57)}\\
&= \operatorname{Tr}\mathscr{X}_{\boldsymbol{\sigma}}\Big(\mathscr{X}_{\tau_i}\mathscr{X}_{\tau_j}\mathscr{X}_{\tau_k}\bigotimes_{m\neq i,j,k}\mathscr{X}_{\tau_m}\Big)\mathbb{H}_{\langle ij\rangle}\mathbb{H}_{\langle jk\rangle}\\
&= \operatorname{Tr}\mathscr{X}_{\boldsymbol{\sigma}}\mathscr{X}_{\boldsymbol{\tau}}\mathbb{H}_{\langle ij\rangle}\mathbb{H}_{\langle jk\rangle}.
\end{aligned}$$

Hence we have shown that $\operatorname{Tr}\mathscr{X}_{\boldsymbol{\sigma}}\mathbb{H}_{\langle ij\rangle}\mathscr{X}_{\boldsymbol{\tau}}\mathbb{H}_{\langle kl\rangle} = \operatorname{Tr}\mathscr{X}_{\boldsymbol{\sigma}}\mathscr{X}_{\boldsymbol{\tau}}\mathbb{H}_{\langle ij\rangle}\mathbb{H}_{\langle kl\rangle}$ as long as $\langle ij\rangle \neq \langle kl\rangle$, meaning that $\operatorname{Tr}(\mathscr{X}_{\boldsymbol{\sigma}}\mathscr{X}_{\boldsymbol{\tau}}\mathbb{H}_x\mathbb{H}_{x'} - \mathscr{X}_{\boldsymbol{\sigma}}\mathbb{H}_x\mathscr{X}_{\boldsymbol{\tau}}\mathbb{H}_{x'}) = \delta_{xx'}\operatorname{Tr}(\mathscr{X}_{\boldsymbol{\sigma}}\mathscr{X}_{\boldsymbol{\tau}}\mathbb{H}_x^2 - \mathscr{X}_{\boldsymbol{\sigma}}\mathbb{H}_x\mathscr{X}_{\boldsymbol{\tau}}\mathbb{H}_x)$. Thus the derivation of Eq. (A.54) is justified.

If we consider the difference between $W_{e^{-\mathrm{i}\varepsilon H}}$ and $W_{\mathbb{1}}$, denoted as δW,

$$\delta W[\boldsymbol{\sigma},\boldsymbol{\tau}] \equiv W_{e^{-\mathrm{i}\varepsilon H}}[\boldsymbol{\sigma},\boldsymbol{\tau}] - W_{\mathbb{1}}[\boldsymbol{\sigma},\boldsymbol{\tau}] = -\varepsilon^2\sum_x \operatorname{Tr}(\mathscr{X}_{\boldsymbol{\sigma}}\mathscr{X}_{\boldsymbol{\tau}}\mathbb{H}_x^2 - \mathscr{X}_{\boldsymbol{\sigma}}\mathbb{H}_x\mathscr{X}_{\boldsymbol{\tau}}\mathbb{H}_x) + \mathscr{O}(\varepsilon^4). \quad \text{(A.58)}$$

$\delta W[\boldsymbol{\sigma},\boldsymbol{\tau}] = \sum_x \delta W_x[\boldsymbol{\sigma},\boldsymbol{\tau}] W_{\mathbb{1}_{\bar{x}}}[\boldsymbol{\sigma},\boldsymbol{\tau}]$ can be expressed as a sum of terms on each bond x (at least to the order of ε^2). To carry out the ε expansion more systematically, we choose to focus on a single bond, and define the EF difference

$$\delta W_x[\boldsymbol{\sigma},\boldsymbol{\tau}] \equiv W_{e^{-\mathrm{i}\varepsilon H_x}}[\boldsymbol{\sigma},\boldsymbol{\tau}] - W_{\mathbb{1}_x}[\boldsymbol{\sigma},\boldsymbol{\tau}] = \operatorname{Tr}\left(\mathscr{X}_{\boldsymbol{\sigma}} e^{-\mathrm{i}\varepsilon\mathbb{H}_x}\mathscr{X}_{\boldsymbol{\tau}} e^{\mathrm{i}\varepsilon\mathbb{H}_x}\right) - \operatorname{Tr}\left(\mathscr{X}_{\boldsymbol{\sigma}}\mathscr{X}_{\boldsymbol{\tau}}\right), \qquad \text{(A.59)}$$

where $\boldsymbol{\sigma} = (\sigma_i, \sigma_j)$ is restricted to the two sites i, j connected by the bond x and similarly for $\boldsymbol{\tau}$. $\delta W_x[\boldsymbol{\sigma},\boldsymbol{\tau}] = 0$ vanishes as long as $\sigma_i = \sigma_j$ or $\tau_i = \tau_j$, because in that case, $\mathscr{X}_{\boldsymbol{\sigma}}$ or $\mathscr{X}_{\boldsymbol{\tau}}$ will commute with $\mathbb{H}_x$ and hence the two traces will cancel with each other. Therefore there are only two independent non-trivial components of $\delta W[\boldsymbol{\sigma},\boldsymbol{\tau}]$, which we denote as u and v:

$$\begin{aligned} u &= \delta W[\mathsf{II}_i\mathsf{X}_j,\mathsf{II}_i\mathsf{X}_j] = \delta W[\mathsf{X}_i\mathsf{II}_j,\mathsf{X}_i\mathsf{II}_j], \\ v &= \delta W[\mathsf{II}_i\mathsf{X}_j,\mathsf{X}_i\mathsf{II}_j] = \delta W[\mathsf{X}_i\mathsf{II}_j,\mathsf{II}_i\mathsf{X}_j]. \end{aligned} \tag{A.60}$$

So we only need to focus on these terms and perform the ε expansion following the definition

$$\begin{aligned} \delta W_x[\boldsymbol{\sigma},\boldsymbol{\tau}] &= \mathrm{Tr}\left(\mathscr{X}_{\boldsymbol{\sigma}} e^{-\mathrm{i}\varepsilon H_x} \otimes e^{-\mathrm{i}\varepsilon H_x} \mathscr{X}_{\boldsymbol{\tau}} e^{\mathrm{i}\varepsilon H_x} \otimes e^{\mathrm{i}\varepsilon H_x}\right) - \mathrm{Tr}\left(\mathscr{X}_{\boldsymbol{\sigma}} \mathscr{X}_{\boldsymbol{\tau}}\right) \\ &= \sum_{k=1}^{\infty} \varepsilon^{2k} \sum_{n_1+n_2+n_3+n_4=2k} \frac{\mathrm{i}^{-n_1-n_2+n_3+n_4}}{n_1!n_2!n_3!n_4!} \mathrm{Tr}\left(\mathscr{X}_{\boldsymbol{\sigma}} H_x^{n_1} \otimes H_x^{n_2} \mathscr{X}_{\boldsymbol{\tau}} H_x^{n_3} \otimes H_x^{n_4}\right). \end{aligned} \tag{A.61}$$

The ε odd power terms must vanish because $\delta W_x[\boldsymbol{\sigma},\boldsymbol{\tau}]$ must be real. To the ε^4 order, we found

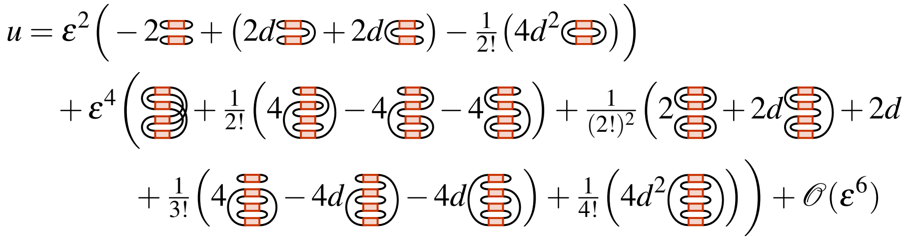

$$\begin{aligned} &= -\varepsilon^2\left(2R^{(1)(2)}_{(1)(2)} - 2d\left(R^{(12)}_{(1)(2)} + R^{(1)(2)}_{(12)}\right) + 2d^2 R^{(12)}_{(12)}\right) \\ &\quad + \varepsilon^4\Big(R^{(13)(24)}_{(12)(34)} + 2\left(R^{(124)(3)}_{(123)(4)} - R^{(12)(34)}_{(123)(4)} - R^{(123)(4)}_{(12)(34)}\right) + \tfrac{1}{2}\left(R^{(12)(34)}_{(12)(34)} + dR^{(1234)}_{(12)(34)} + dR^{(12)(34)}_{(1234)}\right) \\ &\qquad + \tfrac{2}{3}\left(R^{(123)(4)}_{(123)(4)} - dR^{(1234)}_{(123)(4)} - dR^{(123)(4)}_{(1234)}\right) + \tfrac{1}{6}d^2 R^{(1234)}_{(1234)}\Big) + \mathscr{O}(\varepsilon^6), \end{aligned} \tag{A.62}$$

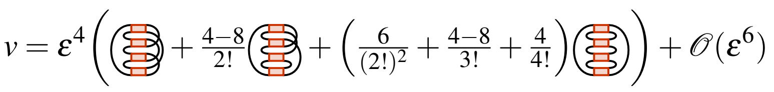

$$= \varepsilon^4\left(R^{(1432)}_{(1234)} - 2R^{(1243)}_{(1234)} + R^{(1234)}_{(1234)}\right) + \mathscr{O}(\varepsilon^6).$$

In the diagrams, each small red block represents a copy of the bond Hamiltonian H_x. Their legs are contracted according to the assignment of the permutations $\boldsymbol{\sigma}$ and $\boldsymbol{\tau}$. The result can be expressed in terms of the generalized spectral form factor $R^{g_j}_{g_i}$, labeled by two permutations $g_i, g_j \in S_n$ acting separately on sites i and j,

$$R^{g_j}_{g_i} = \mathrm{Tr}(H_{ij}^{\otimes n} \mathscr{X}_{g_i g_j}). \tag{A.63}$$

where $\mathscr{X}_{g_ig_j} = \mathscr{X}_{g_i}\mathscr{X}_{g_j}$ is the representation of g_i and g_j in the n-replicated Hilbert space. For example, $R^{(1)(2)}_{(1)(2)} = (\mathrm{Tr} H_{ij})^2$, $R^{(12)}_{(1)(2)} = \mathrm{Tr}_j(\mathrm{Tr}_i H_{ij})^2$ (where Tr_i denotes the partial trace over site i), and $R^{(12)}_{(12)} = \mathrm{Tr}(H^2_{ij})$.

Given the components u and v, we can rewrite $\delta W_x[\boldsymbol{\sigma}, \boldsymbol{\tau}]$ in the operator form

$$\delta \hat{W}_x = \frac{1-Z_iZ_j}{2}(u+vX_iX_j)\frac{1-Z_iZ_j}{2}, \tag{A.64}$$

therefore the EF operator reads

$$\hat{W}_{e^{-\mathrm{i}\varepsilon H}} = \hat{W}_{\mathbb{1}} + \sum_x \delta\hat{W}_x \otimes \hat{W}_{\mathbb{1}_{\bar{x}}} = \hat{W}_{\mathbb{1}} + \sum_{ij} \frac{1-Z_iZ_j}{2}(u+vX_iX_j)\frac{1-Z_iZ_j}{2} \otimes \hat{W}_{\mathbb{1}_{\bar{ij}}}. \tag{A.65}$$

The EF Hamiltonian is therefore given by

$$\begin{aligned}\hat{H}_{\mathrm{EF}} &= \frac{1}{\varepsilon^2}(\mathbb{1} - \hat{W}_{e^{-\mathrm{i}\varepsilon H}}\hat{W}_{\mathbb{1}}^{-1})\\ &= -\frac{1}{\varepsilon^2}\sum_{ij}\frac{1-Z_iZ_j}{2}(u+vX_iX_j)\frac{1-Z_iZ_j}{2}\hat{W}_{\mathbb{1}_{ij}}^{-1}\\ &= -\frac{1}{\varepsilon^2}\sum_{ij}\frac{1-Z_iZ_j}{2}(u+vX_iX_j)\frac{1-Z_iZ_j}{2}\frac{1}{d^2(d^2-1)}e^{-\delta(X_i+X_j)}\\ &= -\sum_{ij}\frac{1-Z_iZ_j}{2}\frac{u+vX_iX_j}{\varepsilon^2 d^2(d^2-1)}e^{-\delta(X_i+X_j)}\end{aligned} \tag{A.66}$$

Therefore the EF Hamiltonian generally take the form of

$$\hat{H}_{\mathrm{EF}} = \sum_{ij} g\frac{1-Z_iZ_j}{2}e^{-\beta X_iX_j - \delta(X_i+X_j)}, \tag{A.67}$$

consistent with the general form in Eq. (2.32). Comparing Eq. (A.66) with Eq. (A.67), we should identify

$$ge^{-\beta X_iX_j} = -\frac{u+vX_iX_j}{\varepsilon^2 d^2(d^2-1)}, \tag{A.68}$$

which indicates

$$\begin{aligned} g\cosh\beta &= -\frac{u}{\varepsilon^2 d^2(d^2-1)} = \frac{1}{d^2(d^2-1)}(u_2 - u_4\varepsilon^2 + \mathscr{O}(\varepsilon^4)) \\ g\sinh\beta &= \frac{v}{\varepsilon^2 d^2(d^2-1)} = \frac{1}{d^2(d^2-1)}(v_4\varepsilon^2 + \mathscr{O}(\varepsilon^4)), \end{aligned} \tag{A.69}$$

where the coefficients u_2, u_4, v_4 are defined in terms of generalized spectral form factors $R_{g_i}^{g_j}$ as

$$\begin{aligned} u_2 &= 2R_{(1)(2)}^{(1)(2)} - 2d\big(R_{(1)(2)}^{(12)} + R_{(12)}^{(1)(2)}\big) + 2d^2 R_{(12)}^{(12)}, \\ u_4 &= R_{(12)(34)}^{(13)(24)} + 2\big(R_{(123)(4)}^{(124)(3)} - R_{(123)(4)}^{(12)(34)} - R_{(12)(34)}^{(123)(4)}\big) + \tfrac{1}{2}\big(R_{(12)(34)}^{(12)(34)} + dR_{(12)(34)}^{(1234)} + dR_{(1234)}^{(12)(34)}\big) \\ &\quad + \tfrac{2}{3}\big(R_{(123)(4)}^{(123)(4)} - dR_{(123)(4)}^{(1234)} - dR_{(1234)}^{(123)(4)}\big) + \tfrac{1}{6}d^2 R_{(1234)}^{(1234)}, \\ v_4 &= R_{(1234)}^{(1432)} - 2R_{(1234)}^{(1243)} + R_{(1234)}^{(1234)}. \end{aligned} \tag{A.70}$$

For specific model of H_{ij}, we can evaluate the generalized spectral form factors, then we can determine the parameters g and β as well as the EF Hamiltonian. In the following, we will perform the calculation for random U(d) spin model and the locally scrambled Ising model.

For two-qudit GUE Hamiltonians, the generalized spectral form factors, defined in Eq. (A.63), can be evaluated under the GUE average using the basic property that

$$\mathop{\mathbb{E}}_{\text{GUE}} H_{ij}^{\otimes 2} \equiv \mathop{\mathbb{E}}_{\text{GUE}}$$

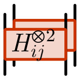

$$= \frac{1}{d^2}$$

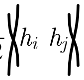

$$\equiv \frac{1}{d^2}\mathscr{X}_{(12)_i(12)_j}, \tag{A.71}$$

the GUE average of n-replicated Hamiltonian H_{ij} can be obtained by summing over Wick contractions

$$\mathop{\mathbb{E}}_{\text{GUE}} H_{ij}^{\otimes n} = \begin{cases} d^{-n}\sum_{h_i = h_j \in P_n} \mathscr{X}_{h_i h_j} & n \in \text{even}, \\ 0 & n \in \text{odd}, \end{cases} \tag{A.72}$$

where P_n denotes all possible pair-wise exchange of n replicas. Then the generalized spectral form factor reads

$$\mathop{\mathbb{E}}_{\mathrm{GUE}} R_{g_i}^{g_j} = \frac{1}{d^n} \sum_{h \in P_n} \mathrm{Tr}(\mathscr{X}_{g_i} \mathscr{X}_h)\, \mathrm{Tr}(\mathscr{X}_{g_j} \mathscr{X}_h), \tag{A.73}$$

whose results are enumerated in Tab. A.1. Substituting these results to Eq. (A.70), we find $u_2 = 2(d^2-1)^2$, $u_4 = \frac{11}{6}(d^2-1)^2$, and $v_4 = 2(d^2-1)^2/d^2$. By solving Eq. (A.69), we can determine the parameters g and β to the order of ε^2,

$$\begin{aligned} g &= 2(1-d^{-2})\big(1 - \tfrac{11}{12}\varepsilon^2 + \mathscr{O}(\varepsilon^4)\big), \\ \beta &= \varepsilon^2/d^2 + \mathscr{O}(\varepsilon^4). \end{aligned} \tag{A.74}$$

In conclusion, as we consider the locally scrambled quantum dynamics by alternatively applying the small unitary $e^{-\mathrm{i}\varepsilon H}$ and the local scramblers, the evolution of the corresponding EF state will be governed by $\partial_t |W_{\Psi_t}\rangle = -\hat{H}_{\mathrm{EF}} |W_{\Psi_t}\rangle$, with the EF Hamiltonian $\hat{H}_{\mathrm{EF}}$ given by Eq. (A.67). The random $\mathrm{U}(d)$ spin model H in Eq. (2.74) corresponds to the set of parameters in Eq. (A.74) for $\hat{H}_{\mathrm{EF}}$.

Table A.1. Spectral form factor of two-qudit GUE Hamiltonian

$R_{(1)(2)}^{(1)(2)}$		1	$R_{(1)(2)}^{(12)}$		d	$R_{(12)}^{(1)(2)}$		d
$R_{(123)(4)}^{(123)(4)}$	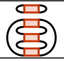	3	$R_{(123)(4)}^{(124)(3)}$	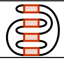	3	$R_{(123)(4)}^{(1234)}$	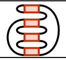	$2d+\frac{1}{d}$
$R_{(123)(4)}^{(12)(34)}$	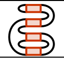	d^2+2	$R_{(1234)}^{(1243)}$	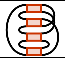	d^2+2	$R_{(12)(34)}^{(123)(4)}$	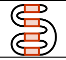	d^2+2
$R_{(1234)}^{(1234)}$	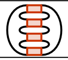	$2d^2+\frac{1}{d^2}$	$R_{(1234)}^{(1432)}$	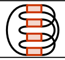	$2d^2+\frac{1}{d^2}$	$R_{(1234)}^{(12)(34)}$	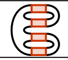	$d^3+d+\frac{1}{d}$
$R_{(12)(34)}^{(12)(34)}$	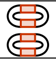	d^4+2	$R_{(12)}^{(12)}$		d^2	$R_{(1234)}^{(123)(4)}$	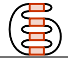	$2d+\frac{1}{d}$
$R_{(12)(34)}^{(13)(24)}$	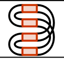	$2d^2+1$	$R_{(12)(34)}^{(1234)}$	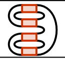	$d^3+d+\frac{1}{d}$			

Appendix B

Appendix for Chapter 4

B.1 Detailed calculations of the two-point correlation matrix of the non-equilibrium steady state

B.1.1 Dissipative Lindblad operator

Liouville space

In this section, we define the original Hilbert space $\mathscr{H}$ spanned by the ket vectors $|n_1, \cdots, n_L\rangle$. These basis ket vectors are generated by applying creation operators $c_i^\dagger$ $(i = 1, \cdots, L)$ on the vacuum state $|0\rangle$. The creation and annihilation operators $c_i^\dagger, c_i$ satisfy the following anti-commutation relation,

$$\{c_i, c_j\} = \{c_i^\dagger, c_j^\dagger\} = 0, \{c_i^\dagger, c_j\} = \delta_{ij}. \tag{B.1}$$

The Liouville space $\mathscr{H}_L$ is defined as a linear space spanned by all the linear operators acting on $\mathscr{H}$. For a general linear operator $A(c^\dagger, c)$ acting on in $\mathscr{H}$, we can define a ket vector $|A\rangle$ in $\mathscr{H}_L$. The orthonormal basis in $\mathscr{H}_L$ can be constructed from the orthonormal basis in $\mathscr{H}$. Suppose $|n_1, \cdots, n_L\rangle \in \mathscr{H}$ and satisfies

$$\sum_{\mathbf{n}} |n_1, \cdots, n_L\rangle\langle n_1, \cdots, n_L| = \sum_{\mathbf{n}} |\mathbf{n}\rangle\langle\mathbf{n}| = 1_L, \langle n_1', \cdots, n_L'|n_1, \cdots, n_L\rangle = \langle\mathbf{n}'|\mathbf{n}\rangle = \delta_{\mathbf{n}'\mathbf{n}}, \tag{B.2}$$

the orthonormal basis in $\mathscr{H}_L$ can be constructed as $|\mathbf{n},\mathbf{m}\rangle$ which satisfies

$$\sum_{\mathbf{n},\mathbf{m}} |\mathbf{n},\mathbf{m}\rangle\langle\mathbf{n},\mathbf{m}| = 1_{L^2}, \langle\mathbf{n}',\mathbf{m}'|\mathbf{n},\mathbf{m}\rangle = \delta_{\mathbf{n}'\mathbf{n}}\delta_{\mathbf{m}'\mathbf{m}}. \tag{B.3}$$

Thus, we can express the ket vector $|A\rangle$ as

$$|A\rangle = \sum_{\mathbf{n},\mathbf{m}} |\mathbf{n},\mathbf{m}\rangle\langle\mathbf{n},\mathbf{m}|A\rangle \tag{B.4}$$

where $\langle\mathbf{n},\mathbf{m}|A\rangle \equiv \langle\mathbf{n}|A(c^\dagger,c)|\mathbf{m}\rangle$. Henceforth, we will use the eigenstate of the number operator $n_i = c_i^\dagger c_i$ to be the orthonormal basis. Each n_i can be either 0 or 1. Besides, we define the superoperators $c_i^\dagger, c_i, d_i^\dagger, d_i$ as

$$\begin{aligned}
c_i^\dagger|\mathbf{n},\mathbf{m}\rangle &= c_i^\dagger|\mathbf{n}\rangle\langle\mathbf{m}| \\
c_i|\mathbf{n},\mathbf{m}\rangle &= c_i|\mathbf{n}\rangle\langle\mathbf{m}| \\
d_i^\dagger|\mathbf{n},\mathbf{m}\rangle &= (-1)^F|\mathbf{n}\rangle\langle\mathbf{m}|c_i \\
d_i|\mathbf{n},\mathbf{m}\rangle &= (-1)^F|\mathbf{n}\rangle\langle\mathbf{m}|c_i^\dagger.
\end{aligned} \tag{B.5}$$

From these superoperators, we can explicitly write down the identity state $|I\rangle$ as

$$|I\rangle = \sum_{\mathbf{m}} |\mathbf{m},\mathbf{m}\rangle = \exp(\sum_i c_i^\dagger d_i^\dagger)|0,0\rangle = \prod_{i=1}^{L}(1+c_i^\dagger d_i^\dagger)|0,0\rangle \Rightarrow \langle I| = \langle 0,0|\prod_{i=1}^{L}(1+d_i c_i). \tag{B.6}$$

The ensemble average of the operator $A(c^\dagger,c)$ can be expressed as

$$\mathrm{Tr}(\rho A) = \langle I|A(c^\dagger,c)|\rho\rangle = \langle 0,0|\prod_{i=1}^{L}(1+d_i c_i)A(c^\dagger,c)|\rho\rangle. \tag{B.7}$$

Before we plug in our target operators, we need to command normalization on the density matrix,

$$\mathrm{Tr}(\rho) = 1 \Rightarrow \langle I|\rho\rangle = 1. \tag{B.8}$$

This condition is very important to determine the correct normalization condition for the eigenvector.

Formalism for the quadratic Hamiltonian under dissipative dynamics[204]

The Lindblad master equation of the density matrix ρ is written as

$$\frac{d\rho(t)}{dt} = -i[H,\rho(t)] + \sum_{\mu} \Big(L_\mu \rho(t) L_\mu^\dagger - \frac{1}{2}\{L_\mu^\dagger L_\mu, \rho(t)\} \Big) \tag{B.9}$$

where L_μ represents the μth Lindblad operator. The generic density matrix can be written as $\rho(t) = \sum_{\mathbf{m},\mathbf{n}} \rho_{\mathbf{mn}}(t)|\mathbf{m}\rangle\langle\mathbf{n}|$ where $|\mathbf{m}\rangle$ is the complete orthonormal basis which spans the Hilbert space $\mathscr{H}$. First, we perform the vectorization of the density matrix as $|\rho(t)\rangle = \sum_{\mathbf{m},\mathbf{n}} \rho_{\mathbf{mn}}(t)|\mathbf{m},\mathbf{n}\rangle$. The Lindblad master equation can be recast as $i\partial_t|\rho(t)\rangle = \mathscr{M}|\rho(t)\rangle$ where $\mathscr{M}$ is non-Hermitian superoperator, $|\rho(t)\rangle$,

$$\mathscr{M} = H \otimes \mathbb{1} - \mathbb{1} \otimes H + i\sum_{\mu} \Big(L_\mu \otimes L_\mu^\dagger - \frac{1}{2}(L_\mu^\dagger L_\mu \otimes \mathbb{1} + \mathbb{1} \otimes L_\mu^\dagger L_\mu) \Big). \tag{B.10}$$

Hereinafter, we focus on the quadratic fermionic Hamiltonian and the Lindblad operators which involves the linear combination of gain and loss operators,

$$H = \sum_{x,y} H_{x,y} c_x^\dagger c_y, L_\mu^+ = \sum_{\alpha} l_{\alpha,x}^+ c_x^\dagger, L_\mu^- = \sum_{\alpha} l_{\alpha,x}^- c_x. \tag{B.11}$$

For convenience, we define $P_{x,x'}^+ = \sum_\mu l_{\mu,x}^+ l_{\mu,x'}^{+*}$ and $P_{x,x'}^- = \sum_\mu l_{\mu,x}^{-*} l_{\mu,x}^-$. One can derive the corresponding non-Hermitian superoperator $\mathscr{M}$ as

$$\mathscr{M} = \sum_{x,y} \begin{bmatrix} c_x^\dagger & d_x^\dagger \end{bmatrix} \begin{bmatrix} \mathscr{M}_{11} & \mathscr{M}_{12} \\ \mathscr{M}_{21} & \mathscr{M}_{22} \end{bmatrix} \begin{bmatrix} c_y \\ d_y \end{bmatrix} - \sum_{x} \big(H_{x,x} + \frac{i}{2}(P_{x,x}^+ + P_{x,x}^-) \big) \tag{B.12}$$

where

$$M_{11} = H_{x,y} + \frac{i}{2}(P^+_{x,y} - P^-_{x,y}), M_{22} = H_{x,y} + \frac{i}{2}(P^-_{x,y} - P^+_{x,y}), M_{12} = iP^+_{x,y}, M_{21} = iP^-_{x,y}. \tag{B.13}$$

Solving the one-particle correlation matrix at NESS from the eigenvectors of the non-Hermitian superoperator $\mathscr{M}$

Here, we would like to investigate the eigenvalues and eigenvectors of the non-Hermitian superoperator $\mathscr{M}$ which can be recast as

$$\mathscr{M} = \begin{bmatrix} c^\dagger & d^\dagger \end{bmatrix} \begin{bmatrix} i\Lambda + iP^+ & iP^+ \\ iP^- & i\Lambda + iP^- \end{bmatrix} \begin{bmatrix} c \\ d \end{bmatrix} + i\,\mathrm{Tr}\Lambda^+ = \begin{bmatrix} c^\dagger & d^\dagger \end{bmatrix} M \begin{bmatrix} c \\ d \end{bmatrix} + i\,\mathrm{Tr}\Lambda^+ \tag{B.14}$$

where $c^\dagger, d^\dagger, c, d$ are all L dimensional vectors. Let's analyze the eigenvector and eigenvalue of M. Suppose the eigenvector of M can be written as $\begin{bmatrix} \phi, \psi \end{bmatrix}^t$, we can derive the following equations,

$$i(\Lambda + P^+)\phi + iP^+\psi = \omega\phi, i(\Lambda + P^-)\psi + iP^-\phi = \omega\psi \tag{B.15}$$

where ω is the corresponding eigenvalue. By setting $\phi = -\psi$, we can obtain $i\Lambda\phi = \omega\phi$. If we add two equations in Eq. (B.15) together, we would obtain $-i\Lambda^\dagger(\phi + \psi) = \omega(\phi + \psi)$. This suggests that the eigenvalues of M must come in pairs, $(i\lambda_\alpha, -i\lambda_\alpha^*)$. This motivates us to rewrite M as

$$M = i\sum_\alpha \left(\lambda_\alpha |R^-_\alpha\rangle\langle L^-_\alpha| - \lambda^*_\alpha |R^+_\alpha\rangle\langle L^+_\alpha|\right). \tag{B.16}$$

By defining $|\chi\rangle = \begin{bmatrix} c & d \end{bmatrix}^t, \langle\chi| = \begin{bmatrix} c^\dagger & d^\dagger \end{bmatrix}$, the eigen-fermionic operators can be defined

$$f_{\alpha,\pm} = \langle L^\pm_\alpha|\chi\rangle, f^\ddagger_{\alpha,\pm} = \langle\chi|R^\pm_\alpha\rangle. \tag{B.17}$$

Therefore, the superoperator $\mathscr{M}$ would become

$$\mathscr{M} = \sum_{\alpha} \left(i\lambda_{\alpha} f^{\ddagger}_{\alpha,-} f_{\alpha,-} - i\lambda^{*}_{\alpha} f^{\ddagger}_{\alpha,+} f_{\alpha,+} \right) + i \sum_{\alpha} \lambda^{*}_{\alpha}. \tag{B.18}$$

Note that the NESS state is the state with zero eigenvalue. Thus, the NESS ket vector can be constructed as $|\rho_{ness}\rangle = \prod_{\alpha} f^{\ddagger}_{\alpha,+} |0\rangle$. The normalization condition for $|\rho_{ness}\rangle$ is to demand $\langle I|\rho_{ness}\rangle = 1$. One way to obtain the $\langle I|$ in terms of $f^{\ddagger}_{\alpha,+}, f_{\alpha,+}$ operators is to start with $\langle I|M = 0$. Thus, we can easily see the left identity vector is simply $\langle 0| \prod_{\alpha} f_{\alpha,+}$. To compute the correlation matrix,

$$\langle I| c^{\dagger}_{x} c_{y} |\rho_{ness}\rangle = S_{x,\alpha} V_{y,\beta} \langle I| f^{\ddagger}_{\alpha} f_{\beta} |\rho_{ness}\rangle = \sum_{\lambda^{*}_{\alpha}} S_{x,\alpha} V_{y,\alpha}. \tag{B.19}$$

Note that S, V can be constructed from the transformation matrix which transforms the original basis to the diagonal basis. The transformation matrices are

$$f_{\alpha} = R_{\alpha,j} c_{j}, f^{\ddagger}_{\beta} = L_{\beta,j} c^{\dagger}_{j} \Rightarrow S = L^{-1}, V = R^{-1}. \tag{B.20}$$

Thus, the one-particle correlation matrix can be computed by

$$G_{xy} = \sum_{\lambda^{*}_{\alpha}} L^{-1}_{x,\alpha} R^{-1}_{y,\alpha} \tag{B.21}$$

B.1.2 Dephasing Lindblad operator

The generic dephasing Lindblad operator is defined as

$$L_{\alpha} = \sum_{x} m_{\alpha,x} c^{\dagger}_{x} c_{x}. \tag{B.22}$$

The dynamics of the two-point correlation matrix G_{xy} can be derived as

$$\frac{d}{dt}G_{xy} = \mathrm{Tr}\left[(\partial_t\rho)c_x^\dagger c_y\right], \partial_t\rho = -i[H,\rho] + \sum_\alpha \left(L_\alpha\rho L_\alpha^\dagger - \frac{1}{2}L_\alpha^\dagger L_\alpha\rho - \frac{1}{2}\rho L_\alpha^\dagger L_\alpha\right). \tag{B.23}$$

The only difference between the dissipative and dephasing Lindblad operators is the second term. By plugging the dephasing Lindblad operator (Eq. (B.22)), one can obtain

$$\begin{aligned}
&\sum_{u,v,\alpha} m_{\alpha,u}m_{\alpha,v}^* \,\mathrm{Tr}\left[c_u^\dagger c_u\rho c_v^\dagger c_v c_x^\dagger c_y - \frac{1}{2}c_v^\dagger c_v c_u^\dagger c_u\rho c_x^\dagger c_y - \frac{1}{2}\rho c_v^\dagger c_v c_u^\dagger c_u c_x^\dagger c_y\right] \\
&= \sum_{u,v,\alpha} m_{\alpha,u}m_{\alpha,v}^* \,\mathrm{Tr}\left[\rho\left(c_v^\dagger c_v c_x^\dagger c_y c_u^\dagger c_u - \frac{1}{2}c_x^\dagger c_y c_v^\dagger c_v c_u^\dagger c_u - \frac{1}{2}c_v^\dagger c_v c_u^\dagger c_u c_x^\dagger c_y\right)\right].
\end{aligned} \tag{B.24}$$

Let’s move the fermonic operators explicitly,

$$\begin{aligned}
&c_v^\dagger c_v c_x^\dagger c_y c_u^\dagger c_u - \frac{1}{2}c_x^\dagger c_y c_v^\dagger c_v c_u^\dagger c_u - \frac{1}{2}c_v^\dagger c_v c_u^\dagger c_u c_x^\dagger c_y \\
&= c_v^\dagger c_v c_x^\dagger c_y c_u^\dagger c_u - \frac{1}{2}\delta_{yv}c_x^\dagger c_v c_u^\dagger c_u - \frac{1}{2}c_v^\dagger c_x^\dagger c_y c_v c_u^\dagger c_u - \delta_{ux}\frac{1}{2}c_v^\dagger c_v c_u^\dagger c_y - \frac{1}{2}c_v^\dagger c_v c_u^\dagger c_x^\dagger c_y c_u \\
&= -\frac{1}{2}\delta_{yv}c_x^\dagger c_v c_u^\dagger c_u + \frac{1}{2}\delta_{xv}c_v^\dagger c_y c_u^\dagger c_u - \frac{1}{2}\delta_{ux}c_v^\dagger c_v c_u^\dagger c_y + \frac{1}{2}\delta_{yu}c_v^\dagger c_v c_x^\dagger c_u. \\
&= \frac{1}{2}\delta_{xv}c_v^\dagger c_y c_u^\dagger c_u - \frac{1}{2}\delta_{ux}\delta_{uv}c_v^\dagger c_y - \frac{1}{2}\delta_{ux}c_u^\dagger c_v^\dagger c_v c_y + \frac{1}{2}\delta_{yu}c_v^\dagger c_v c_x^\dagger c_u - \frac{1}{2}\delta_{yv}\delta_{uv}c_x^\dagger c_u - \frac{1}{2}\delta_{yv}c_u^\dagger c_x^\dagger c_v c_u \\
&= \frac{1}{2}\delta_{xv}c_v^\dagger c_y c_u^\dagger c_u - \frac{1}{2}\delta_{ux}\delta_{uv}c_v^\dagger c_y - \frac{1}{2}\delta_{ux}c_u^\dagger c_y c_v^\dagger c_v + \frac{1}{2}\delta_{ux}\delta_{vy}c_u^\dagger c_v \\
&+ \frac{1}{2}\delta_{yu}c_v^\dagger c_v c_x^\dagger c_u - \frac{1}{2}\delta_{yv}\delta_{uv}c_x^\dagger c_u - \frac{1}{2}\delta_{yv}c_u^\dagger c_u c_x^\dagger c_v + \frac{1}{2}\delta_{yv}\delta_{xu}c_u^\dagger c_v \\
&= \frac{1}{2}\delta_{xv}c_v^\dagger c_y c_u^\dagger c_u - \frac{1}{2}\delta_{ux}c_u^\dagger c_y c_v^\dagger c_v + \frac{1}{2}\delta_{yu}c_v^\dagger c_v c_x^\dagger c_u - \frac{1}{2}\delta_{yv}c_u^\dagger c_u c_x^\dagger c_v \\
&- \frac{1}{2}\delta_{ux}\delta_{uv}c_v^\dagger c_y + \frac{1}{2}\delta_{ux}\delta_{vy}c_u^\dagger c_v - \frac{1}{2}\delta_{yv}\delta_{uv}c_x^\dagger c_u + \frac{1}{2}\delta_{yv}\delta_{xu}c_u^\dagger c_v
\end{aligned} \tag{B.25}$$

Let’s define $M_{uv} = \sum_\alpha m_{\alpha,u}m_{\alpha,v}^*$ and one can combine the first four terms together as

$$\sum_{u,v}(M_{uv} - M_{vu})(\mathrm{Tr}\left[\frac{1}{2}\rho(\delta_{xv}c_v^\dagger c_y c_u^\dagger c_u)\right] + \mathrm{Tr}\left[\frac{1}{2}\rho(\delta_{yu}c_v^\dagger c_c c_x^\dagger c_u)\right]). \tag{B.26}$$

If we assume that $M_{uv} = M_{vu}$, the four-point correlation functions would not appear in the dynamics of the two-point correlation function. The last four terms in the last line of Eq. (B.25) can be combined as

$$\frac{1}{2}(M_{xy} + M_{yx} - M_{xx} - M_{yy})G_{xy} = M_{xy}G_{xy} - \frac{1}{2}(M_{xx} + M_{yy}) \tag{B.27}$$

The dynamical equation of two-point correlation function becomes

$$\frac{d}{dt}G_{xy} = -i\sum_u (G_{xu}H^T_{uy} + H^T_{xu}G_{uy}) + \frac{1}{2}(2M_{xy} - M_{xx} - M_{yy})G_{xy}. \tag{B.28}$$

For the on-site dephasing Lindblad operator, we have $m_{\alpha,u} = \sqrt{\gamma_\alpha}\delta_{\alpha,u} \Rightarrow M_{xy} = \delta_{xy}\gamma_x$. Thus, one can derive

$$\begin{aligned}\frac{d}{dt}G_{xy} &= -i\sum_u (G_{xu}H^T_{uy} + H^T_{xu}G_{uy}) + \frac{1}{2}(2\sum_\alpha \delta_{\alpha,x}\delta_{\alpha,y}\gamma_\alpha - \gamma_x - \gamma_y)G_{xy} \\ &= -i\sum_u (G_{xu}H^T_{uy} + H^T_{xu}G_{uy}) + \delta_{xy}\gamma_x G_{xy} - \frac{1}{2}\Gamma_{x,x'}G_{x'y} - \frac{1}{2}G_{xy'}\Gamma_{y'y}.\end{aligned} \tag{B.29}$$

where $\Gamma_{x,x'} = \gamma_x\delta_{x,x'}$. The dynamical equation can be recast in matrix form,

$$\frac{d}{dt}G = -i[G, H^T] - \frac{1}{2}\{\Gamma, G\} + \Gamma * G \tag{B.30}$$

where $*$ represents the element-wise multiplication. Combined with the dynamical equation with the dissipator, one can derive

$$\begin{aligned}&\frac{d}{dt}G = -i[G, H^T] - \frac{1}{2}\{P^+ + P^- + \Gamma, G\} + \Gamma * G + P^+ \\ &\Rightarrow \frac{d}{dt}G^T = i[G^T, H] - \frac{1}{2}\{P^+ + P^- + \Gamma, G^T\} + \Gamma * G^T + P^+\end{aligned} \tag{B.31}$$

The two-point correlation matrix for the non-equilibrium steady state can be obtained from

$$i[G^T, H] - \frac{1}{2}\{P^+ + P^- + \Gamma, G^T\} + \Gamma * G^T + P^+ = 0. \tag{B.32}$$

The solution of G^T for the long time limit can be constructed from

$$G^T(t=\infty) = \int_0^\infty ds e^{sW} \tilde{P} e^{sW^\dagger}, W \equiv -iH - \frac{1}{2}(P^+ + P^- + \Gamma), \tilde{P} = \Gamma * G^T + P^+. \tag{B.33}$$

To compute this integral, we express $W/W^\dagger$ in terms of their left/right eigenvectors,

$$W = \sum_\alpha \lambda_\alpha |R^\alpha\rangle\langle L^\alpha|, W^\dagger = \sum_\beta \nu_\beta |\bar{L}^\beta\rangle\langle \bar{R}^\beta| \Rightarrow e^{sW} = \sum_\alpha e^{s\lambda_\alpha}|R^\alpha\rangle\langle L^\alpha|, e^{sW^\dagger} = \sum_\beta e^{s\nu_\beta}|\bar{L}^\beta\rangle\langle \bar{R}^\beta|. \tag{B.34}$$

With assumption for $\mathrm{Re}(\lambda_\alpha + \nu_\beta) > 0$ for any α, β, one can derive

$$G^T(t=\infty) = -\sum_{\alpha,\beta} \frac{D_{\alpha\beta}}{\lambda_\alpha + \nu_\beta}|R^\alpha\rangle\langle \bar{R}^\beta|, D_{\alpha\beta} \equiv \langle L^\alpha|\Gamma * G^T + P^+|\bar{L}^\beta\rangle. \tag{B.35}$$

To solve this equation, we iteratively update the two-point correlation function until $|\sum_k (G_{kk}(t+1) - G_{kk}(t))| < 10^{-5}$.

B.2 Spectral statistics of the one-particle Hamiltonian

The second probe is the adjacent gap ratio $\langle r_n\rangle$ of the one-particle Hamiltonian. The adjacent gap ratio is defined as: let E_{n-1}, E_n, E_{n+1} be three successive eigenvalues of H_{one}. Then, the adjacent gap ratio can be computed from

$$r_n = \frac{\min\{E_n - E_{n-1}, E_{n+1} - E_n\}}{\max\{E_n - E_{n-1}, E_{n+1} - E_n\}}. \tag{B.36}$$

The adjacent ratio reflects the spectral statistics of the one-particle Hamiltonian. The two most common examples are the ergodic phase and localized phase. The ergodic phase gives the value of Gaussian Unitary Ensemble statistics (~ 0.599), whereas the localization phase would be the value of Poisson statistics (~ 0.386). Our results for both dissipative and dissipative-dephasing dynamics are shown in Fig. B.1, which shares a similar structure with the phase diagram of PR. In addition, the extended/localized phase exhibit GUE-like/Poisson values, which suggests that the localization/delocalized phase under non-unitary dynamics behave more similarly with those in the disordered Hamiltonian instead of quasi-periodic Hamiltonian.

(A) Purely dissipative dynamics

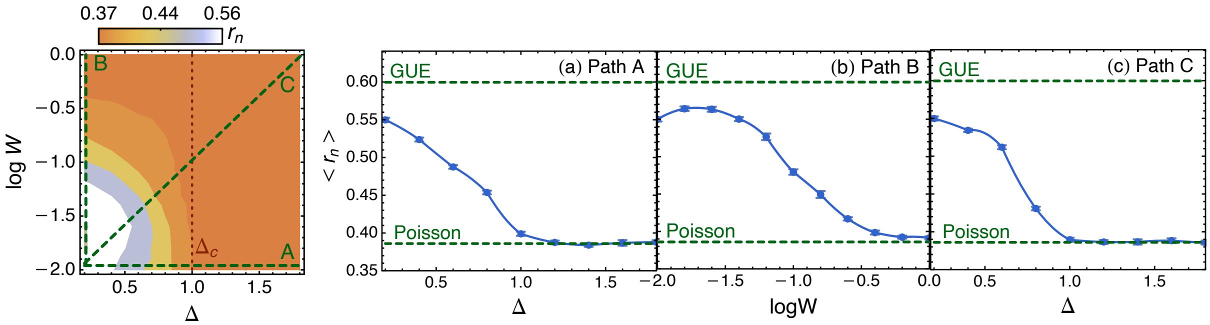

(B) Dissipative-dephasing dynamics for $\log W = -1.0$

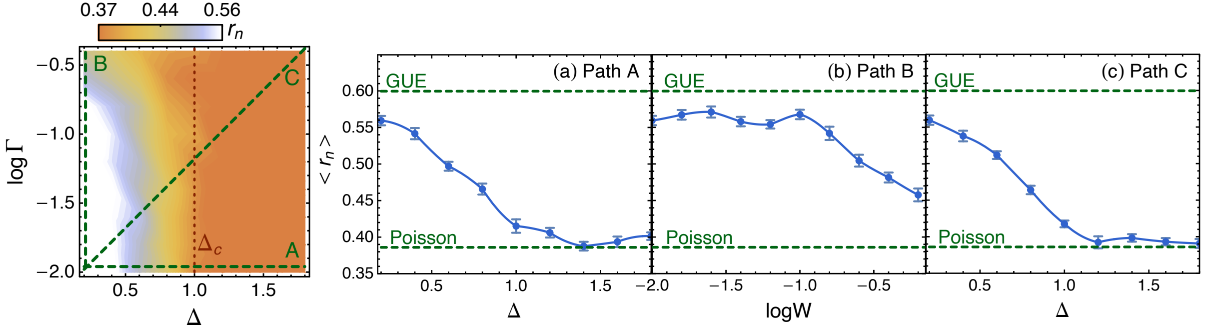

Figure B.1. The adjacent gap ratio for the one-particle Hamiltonian of the NESS

B.3 Detailed calculations of one-particle von Neumann entropy

To calculate the one-particle von Neumann entropy, we divide the system into two subsystems A and $\bar{A}$ of sizes L_A and L_B respectively. Let $\rho_{ness,A}$ be the NESS density matrix corresponding to the subsystem A. We can construct the one-particle correlation matrix as

$$C_{xy,ness} = \mathrm{Tr}(\rho_{ness,A} c_x^\dagger c_y). \tag{B.37}$$

This correlation matrix contains all the one-particle correlation functions within region A. Our goal is to use this one-particle correlation matrix to construct the corresponding Gaussian density matrix,

$$\rho_{A,one} = \frac{1}{Z} \exp\left(- \sum_{x,y \in A} K_{x,y} c_x^\dagger c_y \right) \tag{B.38}$$

The one-particle von Neumann entropy can be defined as

$$S_{A,one} = -\,\mathrm{Tr}\,\rho_{A,one} \ln \rho_{A,one} \tag{B.39}$$

With $n_{i,A}$ being the eigenvalues of $C_{xy,ness}$,

$$S_{A,one} = -\sum_i \big(n_{i,A} \ln n_{i,A} + (1 - n_{i,A} \ln(1 - n_{i,A})) \big) \tag{B.40}$$

Bibliography

[1] Timothy H. Hsieh and Liang Fu. Bulk Entanglement Spectrum Reveals Quantum Criticality within a Topological State. *Physical Review Letter*, 113(10):106801, 2014.

[2] P. W. Anderson. More is different. *Science*, 177(4047):393–396, 1972.

[3] R.K. Pathria. *Statistical Mechanics*. International series of monographs in natural philosophy. Elsevier Science & Technology Books, 1972.

[4] T W B Kibble. Topology of cosmic domains and strings. *Journal of Physics A: Mathematical and General*, 9(8):1387–1398, 1976.

[5] T.W.B. Kibble. Some implications of a cosmological phase transition. *Physics Reports*, 67(1):183 – 199, 1980.

[6] W. H. Zurek. Cosmological experiments in superfluid helium? *Nature*, 317(6037):505–508, 1985.

[7] W. H. Zurek. Cosmological experiments in condensed matter systems. *Physics Reports*, 276(4):177–221, 1996.

[8] Pasquale Calabrese and John Cardy. Evolution of entanglement entropy in one-dimensional systems. *Journal of Statistical Mechanics: Theory and Experiment*, 2005(4):04010, 2005.

[9] Hyungwon Kim and David A. Huse. Ballistic spreading of entanglement in a diffusive nonintegrable system. *Phys. Rev. Lett.*, 111:127205, 2013.

[10] Hong Liu and S. Josephine Suh. Entanglement tsunami: Universal scaling in holographic thermalization. *Phys. Rev. Lett.*, 112:011601, 2014.

[11] Adam M. Kaufman, M. Eric Tai, Alexander Lukin, Matthew Rispoli, Robert Schittko, Philipp M. Preiss, and Markus Greiner. Quantum thermalization through entanglement in an isolated many-body system. *Science*, 353(6301):794–800, 2016.

[12] Wen Wei Ho and Dmitry A. Abanin. Entanglement dynamics in quantum many-body systems. *Physical Review B*, 95(9):094302, 2017.

[13] J. Eisert, M. Friesdorf, and C. Gogolin. Quantum many-body systems out of equilibrium. *Nature Physics*, 11(2):124–130, 2015.

[14] Pedro Ponte, Anushya Chandran, Z. Papić, and Dmitry A. Abanin. Periodically driven ergodic and many-body localized quantum systems. *Annals of Physics*, 353:196 – 204, 2015.

[15] R. Moessner and S. L. Sondhi. Equilibration and order in quantum floquet matter. *Nature Physics*, 13:424 EP –, 2017.

[16] Jens H. Bardarson, Frank Pollmann, and Joel E. Moore. Unbounded Growth of Entanglement in Models of Many-Body Localization. *Physical Review Letter*, 109(1):017202, 2012.

[17] Jonas A. Kjäll, Jens H. Bardarson, and Frank Pollmann. Many-Body Localization in a Disordered Quantum Ising Chain. *Physical Review Letter*, 113(10):107204, 2014.

[18] David J. Luitz, Nicolas Laflorencie, and Fabien Alet. Many-body localization edge in the random-field Heisenberg chain. *Physical Review B*, 91(8):081103, 2015.

[19] Rahul Nandkishore and David A. Huse. Many-Body Localization and Thermalization in Quantum Statistical Mechanics. *Annual Review of Condensed Matter Physics*, 6:15–38, 2015.

[20] Romain Vasseur and Joel E. Moore. Nonequilibrium quantum dynamics and transport: from integrability to many-body localization. *Journal of Statistical Mechanics: Theory and Experiment*, 6:064010, 2016.

[21] Dmitry A. Abanin, Ehud Altman, Immanuel Bloch, and Maksym Serbyn. Colloquium: Many-body localization, thermalization, and entanglement. *Rev. Mod. Phys.*, 91:021001, 2019.

[22] Xiaoguang Wang, Shohini Ghose, Barry C. Sanders, and Bambi Hu. Entanglement as a signature of quantum chaos. *Phys. Rev. E*, 70:016217, 2004.

[23] Pavan Hosur, Xiao-Liang Qi, Daniel A. Roberts, and Beni Yoshida. Chaos in quantum channels. *Journal of High Energy Physics*, 2016(2):4, 2016.

[24] Márk Mezei and Douglas Stanford. On entanglement spreading in chaotic systems. *Journal of High Energy Physics*, 2017(5):65, 2017.

[25] Bruno Bertini, Pavel Kos, and Tomaž Prosen. Entanglement Spreading in a Minimal Model of Maximal Many-Body Quantum Chaos. *Physical Review X*, 9(2):021033, 2019.

[26] Hrant Gharibyan, Masanori Hanada, Brian Swingle, and Masaki Tezuka. Quantum Lyapunov spectrum. *Journal of High Energy Physics*, 2019(4):82, 2019.

[27] A. Chandran, C. R. Laumann, and V. Oganesyan. Finite size scaling bounds on many-body localized phase transitions. *arXiv e-prints*, page arXiv:1509.04285, 2015.

[28] Adam Nahum, Jonathan Ruhman, Sagar Vijay, and Jeongwan Haah. Quantum entanglement growth under random unitary dynamics. *Phys. Rev. X*, 7:031016, 2017.

[29] Tianci Zhou and David J. Luitz. Operator entanglement entropy of the time evolution operator in chaotic systems. *Physical Review B*, 95(9):094206, 2017.

[30] Cheryne Jonay, David A. Huse, and Adam Nahum. Coarse-grained dynamics of operator and state entanglement. *arXiv e-prints*, page arXiv:1803.00089, 2018.

[31] C. W. von Keyserlingk, Tibor Rakovszky, Frank Pollmann, and S. L. Sondhi. Operator hydrodynamics, otocs, and entanglement growth in systems without conservation laws. *Phys. Rev. X*, 8:021013, 2018.

[32] Adam Nahum, Sagar Vijay, and Jeongwan Haah. Operator spreading in random unitary circuits. *Phys. Rev. X*, 8:021014, 2018.

[33] Adam Nahum, Jonathan Ruhman, and David A. Huse. Dynamics of entanglement and transport in one-dimensional systems with quenched randomness. *Phys. Rev. B*, 98:035118, 2018.

[34] Tibor Rakovszky, Frank Pollmann, and C. W. von Keyserlingk. Diffusive hydrodynamics of out-of-time-ordered correlators with charge conservation. *Phys. Rev. X*, 8:031058, 2018.

[35] Vedika Khemani, Ashvin Vishwanath, and David A. Huse. Operator spreading and the emergence of dissipative hydrodynamics under unitary evolution with conservation laws. *Phys. Rev. X*, 8:031057, 2018.

[36] Sarang Gopalakrishnan, David A. Huse, Vedika Khemani, and Romain Vasseur. Hydrodynamics of operator spreading and quasiparticle diffusion in interacting integrable systems. *Physical Review B*, 98(22):220303, 2018.

[37] Tibor Rakovszky, C. W. von Keyserlingk, and Frank Pollmann. Entanglement growth after inhomogenous quenches. *Phys. Rev. B*, 100:125139, Sep 2019.

[38] Yi-Zhuang You and Yingfei Gu. Entanglement features of random Hamiltonian dynamics. *Physical Review B*, 98(1):014309, 2018.

[39] Patrick Hayden, Sepehr Nezami, Xiao-Liang Qi, Nathaniel Thomas, Michael Walter, and Zhao Yang. Holographic duality from random tensor networks. *Journal of High Energy Physics*, 2016(11):9, 2016.

[40] Tianci Zhou and Adam Nahum. Emergent statistical mechanics of entanglement in random unitary circuits. *Phys. Rev. B*, 99:174205, May 2019.

[41] Márk Mezei. Membrane theory of entanglement dynamics from holography. *Physical Review D*, 98(10):106025, 2018.

[42] Romain Vasseur, Andrew C. Potter, Yi-Zhuang You, and Andreas W. W. Ludwig. Entanglement transitions from holographic random tensor networks. *Phys. Rev. B*, 100:134203, Oct 2019.

[43] Yi-Zhuang You, Zhao Yang, and Xiao-Liang Qi. Machine learning spatial geometry from entanglement features. *Phys. Rev. B*, 97:045153, 2018.

[44] Laimei Nie, Masahiro Nozaki, Shinsei Ryu, and Mao Tian Tan. Signature of quantum chaos in operator entanglement in 2d CFTs. *arXiv e-prints*, page arXiv:1812.00013, 2018.

[45] Jonah Kudler-Flam, Masahiro Nozaki, Shinsei Ryu, and Mao Tian Tan. Quantum vs. classical information: operator negativity as a probe of scrambling. *Journal of High Energy Physics*, 2020(1):31, 2020.

[46] Ruihua Fan, Pengfei Zhang, Huitao Shen, and Hui Zhai. Out-of-time-order correlation for many-body localization. *Science Bulletin*, 62(10):707 – 711, 2017.

[47] Yuri D. Lensky and Xiao-Liang Qi. Chaos and high temperature pure state thermalization. *Journal of High Energy Physics*, 2019(6):25, 2019.

[48] Don N. Page. Average entropy of a subsystem. *Phys. Rev. Lett.*, 71:1291–1294, 1993.

[49] R. Oliveira, O. C. O. Dahlsten, and M. B. Plenio. Generic entanglement can be generated efficiently. *Phys. Rev. Lett.*, 98:130502, 2007.

[50] Marko Žnidarič. Optimal two-qubit gate for generation of random bipartite entanglement. *Phys. Rev. A*, 76:012318, 2007.

[51] Sagar Vijay and Ashvin Vishwanath. Finite-Temperature Scrambling of a Random Hamiltonian. *arXiv.org*, 2018.

[52] Zi-Wen Liu, Seth Lloyd, Elton Zhu, and Huangjun Zhu. Entanglement, quantum randomness, and complexity beyond scrambling. *Journal of High Energy Physics*, 2018(7):41, 2018.

[53] Daniel A. Rowlands and Austen Lamacraft. Noisy coupled qubits: Operator spreading and the fredrickson-andersen model. *Phys. Rev. B*, 98:195125, 2018.

[54] Amos Chan, Andrea De Luca, and J. T. Chalker. Spectral Statistics in Spatially Extended Chaotic Quantum Many-Body Systems. *Physical Review Letter*, 121(6):060601, 2018.

[55] Amos Chan, Andrea De Luca, and J. T. Chalker. Solution of a Minimal Model for Many-Body Quantum Chaos. *Physical Review X*, 8(4):041019, 2018.

[56] Xiao-Liang Qi, Zhao Yang, and Yi-Zhuang You. Holographic coherent states from random tensor networks. *Journal of High Energy Physics*, 2017(8):60, Aug 2017.

[57] Chao-Ming Jian, Yi-Zhuang You, Romain Vasseur, and Andreas W. W. Ludwig. Measurement-induced criticality in random quantum circuits. *Phys. Rev. B*, 101:104302, Mar 2020.

[58] Yimu Bao, Soonwon Choi, and Ehud Altman. Theory of the phase transition in random unitary circuits with measurements. *Phys. Rev. B*, 101:104301, Mar 2020.

[59] Brian Skinner, Jonathan Ruhman, and Adam Nahum. Measurement-Induced Phase Transitions in the Dynamics of Entanglement. *Physical Review X*, 9(3):031009, 2019.

[60] Shriya Pai, Michael Pretko, and Rahul M. Nandkishore. Localization in Fractonic Random Circuits. *Physical Review X*, 9(2):021003, 2019.

[61] Daniel E. Parker, Xiangyu Cao, Alexander Avdoshkin, Thomas Scaffidi, and Ehud Altman. A universal operator growth hypothesis. *Phys. Rev. X*, 9:041017, 2019.

[62] Hoi Chun Po, Lukasz Fidkowski, Takahiro Morimoto, Andrew C. Potter, and Ashvin Vishwanath. Chiral Floquet Phases of Many-Body Localized Bosons. *Physical Review X*, 6(4):041070, 2016.

[63] Jong Yeon Lee, Junyeong Ahn, Hengyun Zhou, and Ashvin Vishwanath. Topological correspondence between hermitian and non-hermitian systems: Anomalous dynamics. *Phys. Rev. Lett.*, 123:206404, Nov 2019.

[64] Thomas Hartman and Juan Maldacena. Time evolution of entanglement entropy from black hole interiors. *Journal of High Energy Physics*, 2013:14, 2013.

[65] Hong Liu and S. Josephine Suh. Entanglement Tsunami: Universal Scaling in Holographic Thermalization. *Physical Review Letter*, 112(1):011601, 2014.

[66] Nima Lashkari, Douglas Stanford, Matthew Hastings, Tobias Osborne, and Patrick Hayden. Towards the fast scrambling conjecture. *Journal of High Energy Physics*, 2013:22, 2013.

[67] Huzihiro Araki and Elliott H. Lieb. Entropy inequalities. *Communications in Mathematical Physics*, 18(2):160–170, 1970.

[68] Marko Znidaric. Exact convergence times for generation of random bipartite entanglement. *Phys. Rev. A*, 78:032324, 2008.

[69] E. N. Gilbert and J. Riordan. Symmetry types of periodic sequences. *Illinois J. Math.*, 5:657–665, 1961.

[70] Shenglong Xu and Brian Swingle. Locality, quantum fluctuations, and scrambling. *Phys. Rev. X*, 9:031048, Sep 2019.

[71] Hrant Gharibyan, Masanori Hanada, Stephen H. Shenker, and Masaki Tezuka. Onset of random matrix behavior in scrambling systems. *Journal of High Energy Physics*, 2018(7):124, 2018.

[72] Tianci Zhou and Xiao Chen. Operator dynamics in a Brownian quantum circuit. *Physical Review E*, 99(5):052212, 2019.

[73] Xiao Chen and Tianci Zhou. Quantum chaos dynamics in long-range power law interaction systems. *Physical Review B*, 100(6):064305, 2019.

[74] Xiao-Liang Qi, Emily J. Davis, Avikar Periwal, and Monika Schleier-Smith. Measuring operator size growth in quantum quench experiments. *arXiv e-prints*, page arXiv:1906.00524, 2019.

[75] Yaodong Li, Xiao Chen, and Matthew P. A. Fisher. Quantum Zeno effect and the many-body entanglement transition. *Phys. Rev. B*, 98(20):205136, 2018.

[76] Amos Chan, Rahul M. Nandkishore, Michael Pretko, and Graeme Smith. Unitary-projective entanglement dynamics. *Phys. Rev. B*, 99(22):224307, 2019.

[77] Yaodong Li, Xiao Chen, and Matthew P. A. Fisher. Measurement-driven entanglement transition in hybrid quantum circuits. *Phys. Rev. B*, 100:134306, Oct 2019.

[78] M. Szyniszewski, A. Romito, and H. Schomerus. Entanglement transition from variable-strength weak measurements. *Phys. Rev. B*, 100:064204, 2019.

[79] Soonwon Choi, Yimu Bao, Xiao-Liang Qi, and Ehud Altman. Quantum error correction in scrambling dynamics and measurement-induced phase transition. *Phys. Rev. Lett.*, 125:030505, 2020.

[80] Qicheng Tang and W. Zhu. Measurement-induced phase transition: A case study in the nonintegrable model by density-matrix renormalization group calculations. *Phys. Rev. Research*, 2:013022, Jan 2020.

[81] Ruihua Fan, Sagar Vijay, Ashvin Vishwanath, and Yi-Zhuang You. Self-organized error correction in random unitary circuits with measurement. *Phys. Rev. B*, 103:174309, 2021.

[82] Kai-Hsin Wu, Tsung-Cheng Lu, Chia-Min Chung, Ying-Jer Kao, and Tarun Grover. Entanglement renyi negativity across a finite temperature transition: A monte carlo study. *Phys. Rev. Lett.*, 125:140603, 2020.

[83] Tsung-Cheng Lu, Timothy H. Hsieh, and Tarun Grover. Detecting topological order at finite temperature using entanglement negativity. *Phys. Rev. Lett.*, 125:116801, 2020.

[84] Pasquale Calabrese, John Cardy, and Erik Tonni. Entanglement negativity in quantum field theory. *Phys. Rev. Lett.*, 109:130502, 2012.

[85] Pasquale Calabrese, John Cardy, and Erik Tonni. Entanglement negativity in extended systems: a field theoretical approach. *Journal of Statistical Mechanics: Theory and Experiment*, 2013(02):P02008, 2013.

[86] Vincenzo Alba. Entanglement negativity and conformal field theory: a monte carlo study. *Journal of Statistical Mechanics: Theory and Experiment*, 2013(05):P05013, 2013.

[87] Chia-Min Chung, Vincenzo Alba, Lars Bonnes, Pochung Chen, and Andreas M. Läuchli. Entanglement negativity via the replica trick: A quantum monte carlo approach. *Phys. Rev. B*, 90:064401, 2014.

[88] Vincenzo Alba and Pasquale Calabrese. Entanglement and thermodynamics after a quantum quench in integrable systems. *Proceedings of the National Academy of Science*, 114(30):7947–7951, 2017.

[89] Alba, Vincenzo and Calabrese, Pasquale. Quantum information dynamics in multipartite integrable systems. *EPL*, 126(6):60001, 2019.

[90] Michael J. Gullans and David A. Huse. Dynamical purification phase transition induced by quantum measurements. *Phys. Rev. X*, 10:041020, Oct 2020.

[91] Sébastien Gleyzes, Stefan Kuhr, Christine Guerlin, Julien Bernu, Samuel Deléglise, Ulrich Busk Hoff, Michel Brune, Jean-Michel Raimond, and Serge Haroche. Quantum jumps of light recording the birth and death of a photon in a cavity. *Nature*, 446(7133):297–300, 2007.

[92] D. B. Hume, T. Rosenband, and D. J. Wineland. High-fidelity adaptive qubit detection through repetitive quantum nondemolition measurements. *Phys. Rev. Lett.*, 99:120502, 2007.

[93] Kai Eckert, Oriol Romero-Isart, Mirta Rodriguez, Maciej Lewenstein, Eugene S. Polzik, and Anna Sanpera. Quantum non-demolition detection of strongly correlated systems. *Nature Physics*, 4(1):50–54, 2008.

[94] B. R. Johnson, M. D. Reed, A. A. Houck, D. I. Schuster, Lev S. Bishop, E. Ginossar, J. M. Gambetta, L. DiCarlo, L. Frunzio, S. M. Girvin, and R. J. Schoelkopf. Quantum non-demolition detection of single microwave photons in a circuit. *Nature Physics*, 6(9):663–667, 2010.

[95] Jürgen Volz, Roger Gehr, Guilhem Dubois, Jérôme Estève, and Jakob Reichel. Measurement of the internal state of a single atom without energy exchange. *Nature*, 475(7355):210–213, 2011.

[96] Shay Hacohen-Gourgy, Leigh S. Martin, Emmanuel Flurin, Vinay V. Ramasesh, K. Birgitta Whaley, and Irfan Siddiqi. Quantum dynamics of simultaneously measured non-commuting observables. *Nature*, 538(7626):491–494, 2016.

[97] Jean-Claude Besse, Simone Gasparinetti, Michele C. Collodo, Theo Walter, Philipp Kurpiers, Marek Pechal, Christopher Eichler, and Andreas Wallraff. Single-shot quantum nondemolition detection of individual itinerant microwave photons. *Phys. Rev. X*, 8:021003, 2018.

[98] Dayou Yang, Andrey Grankin, Lukas M. Sieberer, Denis V. Vasilyev, and Peter Zoller. Quantum non-demolition measurement of a many-body hamiltonian. *Nature Communications*, 11(1):775, 2020.

[99] Denis V. Vasilyev, Andrey Grankin, Mikhail A. Baranov, Lukas M. Sieberer, and Peter Zoller. Monitoring quantum simulators via quantum nondemolition couplings to atomic clock qubits. *PRX Quantum*, 1:020302, 2020.

[100] Shengqi Sang and Timothy H. Hsieh. Measurement-protected quantum phases. *Phys. Rev. Research*, 3:023200, 2021.

[101] Ali Lavasani, Yahya Alavirad, and Maissam Barkeshli. Measurement-induced topological entanglement transitions in symmetric random quantum circuits. *Nature Physics*, 17(3):342–347, 2021.

[102] Nicolai Lang and Hans Peter Büchler. Entanglement transition in the projective transverse field Ising model. *Phys. Rev. B*, 102(9):094204, 2020.

[103] H. D. Zeh. On the interpretation of measurement in quantum theory. *Foundations of Physics*, 1(1):69–76, 1970.

[104] Wojciech Hubert Zurek. Decoherence, einselection, and the quantum origins of the classical. *Rev. Mod. Phys.*, 75:715–775, 2003.

[105] Seth Lloyd. Capacity of the noisy quantum channel. *Phys. Rev. A*, 55:1613–1622, 1997.

[106] K. Kraus. General state changes in quantum theory. *Annals of Physics*, 64(2):311–335, 1971.

[107] Abraham G. Kofman, Sahel Ashhab, and Franco Nori. Nonperturbative theory of weak pre- and post-selected measurements. *Physics Reports*, 520(2):43–133, 2012.

[108] W. H. Zurek. Pointer basis of quantum apparatus: Into what mixture does the wave packet collapse? *Phys. Rev. D*, 24:1516–1525, 1981.

[109] W. H. Zurek. Environment-induced superselection rules. *Phys. Rev. D*, 26:1862–1880, 1982.

[110] Ch. Wunderlich and Ch. Balzer. Quantum measurements and new concepts for experiments with trapped ions. *Advances in Atomic Molecular and Optical Physics*, 49:293–372, 2003.

[111] Wayne M Itano. Perspectives on the quantum zeno paradox. *Journal of Physics: Conference Series*, 196:012018, 2009.

[112] Akira Ozawa, Josue Davila-Rodriguez, Theodor W. Hänsch, and Thomas Udem. Quantum zeno effect assisted spectroscopy of a single trapped ion. *Scientific Reports*, 8(1):10643, 2018.

[113] G. Lindblad. On the generators of quantum dynamical semigroups. *Communications in Mathematical Physics*, 48(2):119–130, 1976.

[114] A.O. Caldeira and A.J. Leggett. Path integral approach to quantum brownian motion. *Physica A: Statistical Mechanics and its Applications*, 121(3):587 – 616, 1983.

[115] E. Joos and H. D. Zeh. The emergence of classical properties through interaction with the environment. *Zeitschrift für Physik B Condensed Matter*, 59(2):223–243, 1985.

[116] Aditi Mitra. Quantum Quench Dynamics. *Annual Review of Condensed Matter Physics*, 9:245–259, 2018.

[117] Subir Sachdev. *Quantum Phase Transitions*. Cambridge University Press, 2 edition, 2011.

[118] Luca D'Alessio and Marcos Rigol. Dynamical preparation of Floquet Chern insulators. *Nature Communications*, 6:8336, 2015.

[119] M. D. Caio, N. R. Cooper, and M. J. Bhaseen. Quantum quenches in chern insulators. *Phys. Rev. Lett.*, 115:236403, 2015.

[120] Zhoushen Huang and Alexander V. Balatsky. Dynamical Quantum Phase Transitions: Role of Topological Nodes in Wave Function Overlaps. *Physical Review Letters*, 117(8):086802, 2016.

[121] Ying Hu, Peter Zoller, and Jan Carl Budich. Dynamical Buildup of a Quantized Hall Response from Nontopological States. *Physical Review Letters*, 117(12):126803, 2016.

[122] M. D. Caio, N. R. Cooper, and M. J. Bhaseen. Hall response and edge current dynamics in Chern insulators out of equilibrium. *Physical Review B*, 94(15):155104, 2016.

[123] Justin H. Wilson, Justin C. W. Song, and Gil Refael. Remnant Geometric Hall Response in a Quantum Quench. *Physical Review Letters*, 117(23):235302, 2016.

[124] Ce Wang, Pengfei Zhang, Xin Chen, Jinlong Yu, and Hui Zhai. Scheme to measure the topological number of a chern insulator from quench dynamics. *Phys. Rev. Lett.*, 118:185701, 2017.

[125] Jinlong Yu. Phase vortices of the quenched Haldane model. *Phys. Rev. A*, 96(2):023601, 2017.

[126] Chao Yang, Linhu Li, and Shu Chen. Dynamical topological invariant after a quantum quench. *Physical Review B*, 97(6):060304, 2018.

[127] Po-Yao Chang. Topology and entanglement in quench dynamics. *Phys. Rev. B*, 97(22):224304, 2018.

[128] Lin Zhang, Long Zhang, Sen Niu, and Xiong-Jun Liu. Dynamical classification of topological quantum phases. *Science Bulletin*, 63(21):1385–1391, 2018.

[129] Motohiko Ezawa. Topological quantum quench dynamics carrying arbitrary Hopf and second Chern numbers. *Physical Review B*, 98(20):205406, 2018.

[130] Zongping Gong and Masahito Ueda. Topological Entanglement-Spectrum Crossing in Quench Dynamics. *Physical Review Letters*, 121(25):250601, 2018.

[131] Jinlong Yu. Measuring Hopf links and Hopf invariants in a quenched topological Raman lattice. *Phys. Rev. A*, 99(4):043619, 2019.

[132] Long Zhang, Lin Zhang, and Xiong-Jun Liu. Characterizing topological phases by quantum quenches: A general theory. *Phys. Rev. A*, 100(6):063624, 2019.

[133] Tanay Nag, Vladimir Juričić, and Bitan Roy. Out of equilibrium higher-order topological insulator: Floquet engineering and quench dynamics. *Physical Review Research*, 1(3):032045, 2019.

[134] Haiping Hu and Erhai Zhao. Topological Invariants for Quantum Quench Dynamics from Unitary Evolution. *Physical Review Letters*, 124(16):160402, 2020.

[135] Wei Jia, Lin Zhang, Long Zhang, and Xiong-Jun Liu. Dynamically characterizing topological phases by high-order topological charges. *Phys. Rev. A*, 103:052213, 2021.

[136] F. Barratt, Aleix Bou Comas, P. Crowley, V. Oganesyan, P. Sollich, and A. G. Green. Dissipative failure of adiabatic quantum transport as a dynamical phase transition. *Phys. Rev. A*, 103:052427, May 2021.

[137] B. Andrei Bernevig, Taylor L. Hughes, and Shou-Cheng Zhang. Quantum Spin Hall Effect and Topological Phase Transition in HgTe Quantum Wells. *Science*, 314(5806):1757, 2006.

[138] A B Harris. Effect of random defects on the critical behaviour of ising models. *Journal of Physics C: Solid State Physics*, 7(9):1671–1692, 1974.

[139] Lara Ulčakar, Jernej Mravlje, and Tomaž Rejec. Kibble-Zurek Behavior in Disordered Chern Insulators. *Physical Review Letters*, 125(21):216601, 2020.

[140] Dario Patanè, Alessandro Silva, Luigi Amico, Rosario Fazio, and Giuseppe E. Santoro. Adiabatic dynamics in open quantum critical many-body systems. *Phys. Rev. Lett.*, 101:175701, 2008.

[141] Dario Patanè, Luigi Amico, Alessandro Silva, Rosario Fazio, and Giuseppe E. Santoro. Adiabatic dynamics of a quantum critical system coupled to an environment: Scaling and kinetic equation approaches. *Phys. Rev. B*, 80:024302, 2009.

[142] Shuai Yin, Peizhi Mai, and Fan Zhong. Nonequilibrium quantum criticality in open systems: The dissipation rate as an additional indispensable scaling variable. *Phys. Rev. B*, 89:094108, 2014.

[143] P. Nalbach, Smitha Vishveshwara, and Aashish A. Clerk. Quantum Kibble-Zurek physics in the presence of spatially correlated dissipation. *Physical Review B*, 92(1):014306, 2015.

[144] Patrik Hedvall and Jonas Larson. Dynamics of non-equilibrium steady state quantum phase transitions. *arXiv preprint*, 2017.

[145] Davide Rossini and Ettore Vicari. Dynamic kibble-zurek scaling framework for open dissipative many-body systems crossing quantum transitions. *Phys. Rev. Research*, 2:023211, 2020.

[146] R. Monaco, J. Mygind, and R. J. Rivers. Zurek-kibble domain structures: The dynamics of spontaneous vortex formation in annular josephson tunnel junctions. *Phys. Rev. Lett.*, 89:080603, 2002.

[147] R. Monaco, J. Mygind, M. Aaroe, R. J. Rivers, and V. P. Koshelets. Zurek-kibble mechanism for the spontaneous vortex formation in $\mathrm{Nb}-\mathrm{Al}/\mathrm{al}_{\mathrm{ox}}/\mathrm{Nb}$ josephson tunnel junctions: New theory and experiment. *Phys. Rev. Lett.*, 96:180604, 2006.

[148] D J Weir, R Monaco, V P Koshelets, J Mygind, and R J Rivers. Gaussianity revisited: exploring the kibble–zurek mechanism with superconducting rings. *Journal of Physics: Condensed Matter*, 25(40):404207, 2013.

[149] Chad N. Weiler, Tyler W. Neely, David R. Scherer, Ashton S. Bradley, Matthew J. Davis, and Brian P. Anderson. Spontaneous vortices in the formation of bose–einstein condensates. *Nature*, 455(7215):948–951, 2008.

[150] Giacomo Lamporesi, Simone Donadello, Simone Serafini, Franco Dalfovo, and Gabriele Ferrari. Spontaneous creation of kibble–zurek solitons in a bose–einstein condensate. *Nature Physics*, 9(10):656–660, 2013.

[151] Lauriane Chomaz, Laura Corman, Tom Bienaimé, Rémi Desbuquois, Christof Weitenberg, Sylvain Nascimbène, Jérôme Beugnon, and Jean Dalibard. Emergence of coherence via transverse condensation in a uniform quasi-two-dimensional Bose gas. *Nature Communications*, 6:6162, 2015.

[152] Nir Navon, Alexander L. Gaunt, Robert P. Smith, and Zoran Hadzibabic. Critical dynamics of spontaneous symmetry breaking in a homogeneous bose gas. *Science*, 347(6218):167–170, 2015.

[153] Bumsuk Ko, Jee Woo Park, and Y. Shin. Kibble-Zurek universality in a strongly interacting Fermi superfluid. *Nature Physics*, 15(12):1227–1231, 2019.

[154] S. Ulm, J. Roßnagel, G. Jacob, C. Degünther, S. T. Dawkins, U. G. Poschinger, R. Nigmatullin, A. Retzker, M. B. Plenio, F. Schmidt-Kaler, and K. Singer. Observation of the Kibble-Zurek scaling law for defect formation in ion crystals. *Nature Communications*, 4:2290, 2013.

[155] K. Pyka, J. Keller, H. L. Partner, R. Nigmatullin, T. Burgermeister, D. M. Meier, K. Kuhlmann, A. Retzker, M. B. Plenio, W. H. Zurek, A. Del Campo, and T. E. Mehlstäubler. Topological defect formation and spontaneous symmetry breaking in ion Coulomb crystals. *Nature Communications*, 4:2291, 2013.

[156] S. Ejtemaee and P. C. Haljan. Spontaneous nucleation and dynamics of kink defects in zigzag arrays of trapped ions. *Phys. Rev. A*, 87:051401, 2013.

[157] M. Anquez, B. A. Robbins, H. M. Bharath, M. Boguslawski, T. M. Hoang, and M. S. Chapman. Quantum Kibble-Zurek Mechanism in a Spin-1 Bose-Einstein Condensate. *Physical Review Letters*, 116(15):155301, 2016.

[158] Logan W. Clark, Lei Feng, and Cheng Chin. Universal space-time scaling symmetry in the dynamics of bosons across a quantum phase transition. *Science*, 354(6312):606–610, 2016.

[159] Alexander Keesling, Ahmed Omran, Harry Levine, Hannes Bernien, Hannes Pichler, Soonwon Choi, Rhine Samajdar, Sylvain Schwartz, Pietro Silvi, Subir Sachdev, Peter Zoller, Manuel Endres, Markus Greiner, Vladan Vuletić, and Mikhail D. Lukin. Quantum kibble–zurek mechanism and critical dynamics on a programmable rydberg simulator. *Nature*, 568(7751):207–211, 2019.

[160] Matthias Tarnowski, F. Nur Ünal, Nick Fläschner, Benno S. Rem, André Eckardt, Klaus Sengstock, and Christof Weitenberg. Measuring topology from dynamics by obtaining the chern number from a linking number. *Nature Communications*, 10(1):1728, Apr 2019.

[161] Hoi Chun Po, Liujun Zou, T. Senthil, and Ashvin Vishwanath. Faithful tight-binding models and fragile topology of magic-angle bilayer graphene. *Phys. Rev. B*, 99:195455, May 2019.

[162] Ya-Hui Zhang, Dan Mao, Yuan Cao, Pablo Jarillo-Herrero, and T. Senthil. Nearly flat Chern bands in moiré superlattices. *Phys. Rev. B*, 99(7):075127, 2019.

[163] Junyeong Ahn, Sungjoon Park, and Bohm-Jung Yang. Failure of nielsen-ninomiya theorem and fragile topology in two-dimensional systems with space-time inversion symmetry: Application to twisted bilayer graphene at magic angle. *Phys. Rev. X*, 9:021013, 2019.

[164] Zhida Song, Zhijun Wang, Wujun Shi, Gang Li, Chen Fang, and B. Andrei Bernevig. All Magic Angles in Twisted Bilayer Graphene are Topological. *Physical Review Letters*, 123(3):036401, 2019.

[165] Jianpeng Liu, Zhen Ma, Jinhua Gao, and Xi Dai. Quantum Valley Hall Effect, Orbital Magnetism, and Anomalous Hall Effect in Twisted Multilayer Graphene Systems. *Physical Review X*, 9(3):031021, 2019.

[166] Ya-Hui Zhang, Dan Mao, and T. Senthil. Twisted bilayer graphene aligned with hexagonal boron nitride: Anomalous Hall effect and a lattice model. *Physical Review Research*, 1(3):033126, 2019.

[167] Nick Bultinck, Shubhayu Chatterjee, and Michael P. Zaletel. Mechanism for Anomalous Hall Ferromagnetism in Twisted Bilayer Graphene. *Physical Review Letters*, 124(16):166601, 2020.

[168] Xiao-Ye Xu, Yong-Jian Han, Kai Sun, Jin-Shi Xu, Jian-Shun Tang, Chuan-Feng Li, and Guang-Can Guo. Quantum simulation of landau-zener model dynamics supporting the kibble-zurek mechanism. *Phys. Rev. Lett.*, 112:035701, 2014.

[169] Jin-Ming Cui, Yun-Feng Huang, Zhao Wang, Dong-Yang Cao, Jian Wang, Wei-Min Lv, Le Luo, Adolfo Del Campo, Yong-Jian Han, Chuan-Feng Li, and Guang-Can Guo.

Experimental trapped-ion quantum simulation of the kibble-zurek dynamics in momentum space. *Scientific reports*, 6:33381–33381, 2016.

[170] Ming Gong, Xueda Wen, Guozhu Sun, Dan-Wei Zhang, Dong Lan, Yu Zhou, Yunyi Fan, Yuhao Liu, Xinsheng Tan, Haifeng Yu, Yang Yu, Shi-Liang Zhu, Siyuan Han, and Peiheng Wu. Simulating the kibble-zurek mechanism of the ising model with a superconducting qubit system. *Scientific Reports*, 6(1):22667, 2016.

[171] Jingfu Zhang, Fernando M Cucchietti, Raymond Laflamme, and Dieter Suter. Defect production in non-equilibrium phase transitions: experimental investigation of the kibble–zurek mechanism in a two-qubit quantum simulator. *New Journal of Physics*, 19(4):043001, 2017.

[172] Yuki Bando, Yuki Susa, Hiroki Oshiyama, Naokazu Shibata, Masayuki Ohzeki, Fernando Javier Gómez-Ruiz, Daniel A. Lidar, Sei Suzuki, Adolfo del Campo, and Hidetoshi Nishimori. Probing the universality of topological defect formation in a quantum annealer: Kibble-zurek mechanism and beyond. *Phys. Rev. Research*, 2:033369, 2020.

[173] N. W. Ashcroft and N. D. Mermin. *Solid State Physics*. Holt-Saunders, 1976.

[174] P. W. Anderson. Absence of diffusion in certain random lattices. *Phys. Rev.*, 109:1492–1505, 1958.

[175] E. Abrahams, P. W. Anderson, D. C. Licciardello, and T. V. Ramakrishnan. Scaling theory of localization: Absence of quantum diffusion in two dimensions. *Phys. Rev. Lett.*, 42:673–676, 1979.

[176] P G Harper. Single band motion of conduction electrons in a uniform magnetic field. *Proceedings of the Physical Society. Section A*, 68(10):874–878, 1955.

[177] M. Ya. Azbel. Quantum particle in one-dimensional potentials with incommensurate periods. *Phys. Rev. Lett.*, 43:1954–1957, 1979.

[178] Serge Aubry and Gilles André. Analyticity breaking and anderson localization in incommensurate lattices. *Ann. Israel Phys. Soc*, 3(133):18, 1980.

[179] D J Thouless. A relation between the density of states and range of localization for one dimensional random systems. *Journal of Physics C: Solid State Physics*, 5(1):77–81, 1972.

[180] Y. Y. Atas, E. Bogomolny, O. Giraud, and G. Roux. Distribution of the ratio of consecutive level spacings in random matrix ensembles. *Phys. Rev. Lett.*, 110:084101, 2013.

[181] Marko Žnidarič, Antonello Scardicchio, and Vipin Kerala Varma. Diffusive and subdiffusive spin transport in the ergodic phase of a many-body localizable system. *Phys. Rev. Lett.*, 117:040601, 2016.

[182] V K Varma, A Lerose, F Pietracaprina, J Goold, and A Scardicchio. Energy diffusion in the ergodic phase of a many body localizable spin chain. *Journal of Statistical Mechanics: Theory and Experiment*, 2017(5):053101, 2017.

[183] M. Schulz, S. R. Taylor, C. A. Hooley, and A. Scardicchio. Energy transport in a disordered spin chain with broken u(1) symmetry: Diffusion, subdiffusion, and many-body localization. *Phys. Rev. B*, 98:180201, 2018.

[184] Felix Weiner, Ferdinand Evers, and Soumya Bera. Slow dynamics and strong finite-size effects in many-body localization with random and quasiperiodic potentials. *Phys. Rev. B*, 100:104204, 2019.

[185] J. J. Mendoza-Arenas, M. Žnidarič, V. K. Varma, J. Goold, S. R. Clark, and A. Scardicchio. Asymmetry in energy versus spin transport in certain interacting disordered systems. *Phys. Rev. B*, 99:094435, 2019.

[186] Vipin Kerala Varma, Clélia de Mulatier, and Marko Žnidarič. Fractality in nonequilibrium steady states of quasiperiodic systems. *Phys. Rev. E*, 96:032130, 2017.

[187] Archak Purkayastha, Sambuddha Sanyal, Abhishek Dhar, and Manas Kulkarni. Anomalous transport in the aubry-andré-harper model in isolated and open systems. *Phys. Rev. B*, 97:174206, 2018.

[188] Jagannath Sutradhar, Subroto Mukerjee, Rahul Pandit, and Sumilan Banerjee. Transport, multifractality, and the breakdown of single-parameter scaling at the localization transition in quasiperiodic systems. *Phys. Rev. B*, 99:224204, 2019.

[189] Marko Žnidarič and Marko Ljubotina. Interaction instability of localization in quasiperiodic systems. *Proceedings of the National Academy of Sciences*, 115(18):4595–4600, 2018.

[190] Yongchan Yoo, Junhyun Lee, and Brian Swingle. Nonequilibrium steady state phases of the interacting aubry-andré-harper model. *Phys. Rev. B*, 102:195142, 2020.

[191] Marko Žnidarič. Comment on "nonequilibrium steady state phases of the interacting aubry-andré-harper model". *Phys. Rev. B*, 103:237101, 2021.

[192] Yongchan Yoo, Junhyun Lee, and Brian Swingle. Reply to "comment on 'nonequilibrium steady state phases of the interacting aubry-andré-harper model' ". *Phys. Rev. B*, 103:237102, 2021.

[193] Artur M. Lacerda, John Goold, and Gabriel T. Landi. Dephasing enhanced transport in boundary-driven quasiperiodic chains. *Phys. Rev. B*, 104:174203, 2021.

[194] Scott R. Taylor and Antonello Scardicchio. Subdiffusion in a one-dimensional anderson insulator with random dephasing: Finite-size scaling, griffiths effects, and possible implications for many-body localization. *Phys. Rev. B*, 103:184202, 2021.

[195] Xhek Turkeshi, Damien Barbier, Leticia F. Cugliandolo, Marco Schirò, and Marco Tarzia. Destruction of Localization by Thermal Inclusions: Anomalous Transport and Griffiths Effects in the Anderson and André-Aubry-Harper Models. *SciPost Phys.*, 12:189, 2022.

[196] Seth Lloyd. Capacity of the noisy quantum channel. *Phys. Rev. A*, 55:1613–1622, 1997.

[197] Soumya Bera, Henning Schomerus, Fabian Heidrich-Meisner, and Jens H. Bardarson. Many-body localization characterized from a one-particle perspective. *Phys. Rev. Lett.*, 115:046603, 2015.

[198] Hassan Shapourian, Ken Shiozaki, and Shinsei Ryu. Partial time-reversal transformation and entanglement negativity in fermionic systems. *Phys. Rev. B*, 95:165101, 2017.

[199] Hassan Shapourian and Shinsei Ryu. Finite-temperature entanglement negativity of free fermions. *Journal of Statistical Mechanics: Theory and Experiment*, 2019(4):043106, apr 2019.

[200] Hassan Shapourian and Shinsei Ryu. Entanglement negativity of fermions: Monotonicity, separability criterion, and classification of few-mode states. *Phys. Rev. A*, 99:022310, 2019.

[201] Hassan Shapourian, Paola Ruggiero, Shinsei Ryu, and Pasquale Calabrese. Twisted and untwisted negativity spectrum of free fermions. *SciPost Phys.*, 7:37, 2019.

[202] Don Weingarten. Asymptotic behavior of group integrals in the limit of infinite rank. *Journal of Mathematical Physics*, 19(5):999–1001, 1978.

[203] Benoît Collins and Piotr Śniady. Integration with Respect to the Haar Measure on Unitary, Orthogonal and Symplectic Group. *Communications in Mathematical Physics*, 264(3):773–795, 2006.

[204] Tomaž Prosen. Third quantization: a general method to solve master equations for quadratic open fermi systems. *New Journal of Physics*, 10(4):043026, 2008.